Bellows   Tensile Specimen   Linear Variable Differential Transformer

Pekka Moilanen

Pneumatic servo-controlled material testing device capable of operating at high temperature water and irradiation conditions

Pneumatic servo-controlled material testing device capable of operating at high temperature water and irradiation conditions

Pekka Moilanen

VTT Industrial Systems

Abstract

Special requirements set for the constructional materials used in energy production have strongly influenced the challenges in the component design work. Many material parameters such as corrosion, fracture mechanics, fatigue and oxide films are needed as input data for such work. The generation of reliable data calls also for more sophisticated testing systems. The newly developed pneumatic loading technology (patented in Finland and international patents pending) provides important potential benefits and has already been successfully applied to testing many kinds of materials in different test environments. As the moving parts that penetrate the pressure boundary are not needed, the friction force at the sealing element location is avoided. Therefore the load control with pneumatic loading unit is more accurate than with the conventional servo-hydraulic devices. This enables testing of small size samples which is an advantage e.g. when testing irradiated materials or testing materials inside the reactor core of a nuclear power plant and especially in determining environmentally assisted crack growth rates of structural materials. Furthermore, the new design enables simultaneous testing of several samples, which helps produce more reliable statistical data in a more economical way.

This thesis summarizes my work done at the Technical Research Centre of Finland over the past 9 years to increase the knowledge of factors affecting material testing devices and material properties in gas and aqueous coolants at high temperatures. The developed pneumatic servo-controlled material testing device has been used to perform crack growth rate tests as a function of stress intensity factor K for AISI 316 stainless steel and Inconel 182 weld metal in Boiling Water Reactor (BWR) coolant by using small size (10x10x55 mm) three point bending specimens. The load and displacement were controlled during these tests by the pneumatic servo-controlled fracture measuring device (PSCFM device) and based on test results crack growth rates for Inconel weld metal and AISI 316 have been calculated. During the tests, accuracy with very slow

constant displacement rates of 1.2 10^{-5} mm/min and 1.2 10^{-6} mm/min and long term stability of the pneumatic material testing system under high temperature water environment, has been verified. Furthermore, the crack growth rate for Inconel 182 weld metal as a function of sulphate content (10, 20, 30 ppb) of BWR coolant has been determined. These results shows that the crack growth rate of Inconel 182 weld material is strongly affected by the sulphate content of BWR coolant. Furthermore, prototypes of pneumatically powered fatigue (PSCFAT-device), controlled distance electrode (PSCCDE-device) and tensile (PSCINCORE-device) devices have been designed and tested. The units, which were based on proven technology, operated well and gave reliable test results for the material design parameters. The PSCFAT device was tested at room temperature and the degree of specimen bending and general system performance were measured. A strain controlled axial fatigue test in a 12 MPa autoclave at 100°C was also performed. The test material was AISI 316 stainless steel and the specimen failed in its midsection due to fatigue after 15600 cycles. The preliminary tests with pneumatically powered controlled distance electrode arrangement equipment (PSCCDE) is presented. The equipment was tested in air at room temperature and in typical BWR environments. The test material was pure nickel and its oxide film properties were tested in BWR environment as a function of potential.

The design work for the pneumatic tensile testing device which is capable of working in a real reactor core is introduced. Prototype design, load calibrations, load frame for thin specimen tensile testing, and reactor installation with 30 m gas lines is presented. Furthermore, the PSCINCORE device was used to determine stress and strain curves for pure Cu specimen in the BR-2 reactor at Mol in Belgium. Reactor pool water temperature was 90 °C, neutron flux $\sim 0.3*10^{14}$ n cm^{-2}s^{-1}s (E>1 MeV) and damage rate $\sim 2*10^{-4}$ h^{-1}. The test type was constant displacement rate test with strain rate $\sim 10^{-7}$ 1/s.

Some of the results gained in this work are unique, whenever possible however, the test results have been verified by comparison to earlier results with alternative techniques. Invariably, the comparisons prove applicability of the pneumatically powered technology developed in this work.

Preface

Contents

List of abbreviations and used terminology

a	crack length
$A_0 = A/\cos\phi_0$	gliding area of the circular specimen
dA	crack area
a_{eff}	effective crack length
A_{eff}	bellows effective cross section
a_i	momentary crack length
a_I	activity factor
b	uncracked ligament of the specimen
B	thickness of the specimen
b_i	momentary ligament length
b_0	calculated ligament length
b and n	vectors
c_δ	axial spring rate for the bellows
da/dN	crack growth/cycle
E	Young's modulus
E_D	dielectric constant
E_{cor}	corrosion potential
E_{pas}	passivation potential
f_{ij}	dimensionless function of θ
F_L	load, measured by using load sensor
F_C	load calculated from inside pressure of the pneumatic loading unit
F_s	the load loss based on metal bellows own stiffness
g	Kirkwood correlation parameter
Gc	critical energy release rate
i_{crit}	critical current density
i_{pas}	passivation current density
I_n	integral constant which is dependent on n
J	J-integral
$J_{el(i)}$	elastic part of J
$J_{pl(i)}$	plastic part of J

k	material constant
K_1	stress intensity factor (mode I loading)
k_1 and k_2	proportionality constants
ΔK	(K_{max} - K_{min})
K_{eff}	effective stress intensity factor
l_0	original length of specimen
l	length after loading process of the specimen
M	Schmid factor
n	strain hardening exponent
n_W	number of corrugations
p	pressure
P_i	load (incremental)
p_I	partial pressure for gas
p_h	pressure loss
R	K_{min}/K_{max}
r	distance of the stress field from crack tip (polar co-ordinate)
r_y	size of the plastic field at front of crack
$1/r^{1/2}$	singularity of the crack tip
U	momentary voltage difference between the leads
U_0	initial voltage difference between the leads
u_y	distance behind the effective crack
w-a	unbreakable ligament of the specimen
y	distance of the potential drop leads from the crack plane
α	dimensionless constant
δ_b	required axial movement for the whole bellows [mm]
$\Delta_{i(pl)}$	distance for the plastic load line
ΔG°_{MeO}	free energy alteration for metal oxide, MeO

Δ	displacement
Π	potential energy of an elastic specimen body
χ	prior loading history
$\varepsilon_0 = \dfrac{\sigma_0}{E}$	initial strain
γ_i	factor (1 for SENB specimen)
η_i	factor (2 for SENB specimen)
λ	geometry correction factor
$\lambda_0, \phi_0 \, and \, x_0$	angles
θ and r	direction of the crack stress field
θ	angle between the crack tip and stress field
σ	damage stress
σ_{ij}	stress tensor
σ	stress component
σ_0	reference stress (typically yield stress),
$\tilde{\sigma}_{ij} \, ja \, \tilde{\varepsilon}_{ij}$	dimensionless functions from n and θ
τ_{R_0} , γ_R	resolved shear stress and strain
Ag/AgCl (0.01 M KCl)	reference electrode with a Ag/AgCl sensor
BWR	boiling water reactor
CCT panel	center cracked tension panel
CEI	contact electric impedance
CER	contact electric resistance
CDE	controlled-distance electrode arrangements
CT specimen	compact tension specimen
CTOD (δ)	crack tip opening displacement
$(da/dt)_{EAC}$ or $(da/dt)_{SCC}$,	stress corrosion propagation rate
DENT	double edge notched tension specimen
EAC	environmentally assisted cracking
FCC	face-centered cubic
IGSCC	intergranular stress corrosion cracking

K_{ISCC}	threshold stress intensity factor
LVDT	linear variable differential transformer
MT panel	middle tension panel
PD	potential drop
PID	proportional integrator and derivator adjuster
PWR	pressurised water reactor
SENB specimen	single edge notched bend specimen
SCC	stress corrosion cracking
TGSCC	transgranular stress corrosion cracking

Description of the thesis

The author of this thesis has been responsible for all the development work of the different versions of the pneumatic testing devices and measurements as well as data analysis. The references for the applications of the development work described in chapter 7 consist of the follow-up investigations and tests based on proven pneumatic technology. For the tests performed in reactor core the author has designed, constructed and assembled the pneumatic loading device. He has also been responsible for performing the measurements and preliminary post-test data analysis. The operation of the reactor including assembly of the device into the reactor and reactor tests was performed in co-operation with Mr. Patrice Jacquet at Reactor Experiments Department at Mol. The final data analysis for the publication was performed as a co-operation between Dr. Bachu Singh, Mr. Seppo Tähtinen and the author. Regarding the environmental assisted cracking (EAC) tests with fracture mechanical specimens under simulated BWR conditions Mr. Aki Toivonen has performed the crack growth rate data analysis.

With regard to the fatigue test device application the data analysis was performed in co-operation with Mr. Jussi Solin and Prof. Gary Marquis. For the application of the pneumatic testing device to oxide film measurements the data analysis was performed in co-operation with Dr. Timo Saario.

1. Introduction

Modern-day high technologies such as nuclear power plant and fusion reactor technologies have strongly affected the development and testing of construction materials. Instead of traditional material design parameters, such as yield and breaking strength designers have to know much more about specific characteristics of the construction materials. The field of materials and their properties is very wide including aspects such as environmentally assisted cracking (EAC), fatigue, corrosion and irradiation areas. In many cases, materials are used in different environments and, for example, corrosion factors can affect materials durability more than yield and breaking strength based calculations can take into account. Recycling and life cycle considerations also have a marked bearing on today's materials developing work.

In recent years the use of fracture mechanics based approach has become more popular in the research of environmentally assisted cracking (EAC). The main factors of interest are the susceptibility of the material to stress corrosion cracking (SCC) and stress corrosion propagation rate, $(da/dt)_{EAC}$ or $(da/dt)_{SCC}$, as a function of stress intensity factor K_I or J integral. Also, the threshold stress intensity factor for SCC, K_{IEAC} or K_{ISCC}, is of interest. Furthermore, the electric and electrochemical properties of the oxide films formed on construction material surfaces have a significant influence on the susceptibility of materials to general and localized corrosion such as EAC in high-temperature aqueous environments. According to the results on modeling high-temperature aqueous corrosion the properties of oxides are influenced by temperature, potential, electrolyte composition (presence of oxidising, reducing and/or complexing agents) and electrolyte flow rate.

Fatigue design of nuclear components and fusion components in international and national rules is based on local strain variations. The French and German standards are principally parallel to the ASME (American Society In Materials Engineers) code, that gives strain amplitude versus number of cycles graphs for different material classes. These design curves are based on fatigue test sets not covering all factors known to influence the fatigue life, but include a safety factor to cover these aspects and to increase the confidence level of design. One clear deficiency is that the design curves do not specifically address the effects of reactor coolant on fatigue crack initiation. Up to now relatively little test data

is available to assess this potential cause of failure. The limited experimental data indicates a detrimental effect which is dependent on both strain rate and dissolved oxygen content.

The materials employed in the structural components of a fission or fusion reactor, on the other hand, will be exposed simultaneously to external stresses and irradiation induced defect population produced continuously during irradiation. Under these conditions, both the magnitude and the spatial distribution of defect accumulation and hence the deformation behaviour may be substantially different from that in the case of post-irradiation experiments. This raises a serious question as to whether or not the results and the conclusions of the post-irradiation deformation experiments can be taken to represent the behaviour of materials used in the structural components of a nuclear or thermonuclear reactor.

As mentioned above engineering work is based on very strict requirements concerning material properties. It is common knowledge, however, that material durability and usability in modern design work insists knowledge of several design parameters from corrosion, fracture mechanics, oxide films and even from irradiation. To generate values for these kind of design parameters it is necessary to take into account also design work of the testing systems. Typically, durability calculations of the construction materials are based on parameters such as yield limit, breaking strength, strain, shear stress etc.

These parameters can give the basic information on durability of the materials but they can not take into account the special requirements of different environments, i.e. effects from temperature, water environment, corrosion, irradiation etc. EAC, environmentally assisted cracking, can be described as how construction materials can behave under specific working conditions, i.e. how stresses, strains, environmental effects, corrosion, oxide films on surface of materials, irradiation etc. can together affect the durability of the materials.

In this thesis, the basic parameters for EAC are described with help of the fracture mechanics, fatigue, high temperature water environment (BWR), oxide layer on surface of materials and irradiation effects. Furthermore, the development work for the pneumatic servo-controlled material testing system is

introduced. The development work and verification tests consist of the following main subjects:

- Design work for pneumatically powered pressure adjusting loop (PSC) capable of working at 20 MPa pressure level.
- Load calibrations of the pneumatic loading unit with the metal bellows.
- Design work for the pneumatic servo-controlled fracture resistance measuring device, PSCFM-device.
- Design work for the pneumatic servo-controlled distance electrode arrangement, PSCCDE-device.
- Design work for the pneumatic servo-controlled fatigue testing device, PSCFAT-device
- Design work for the pneumatic servo-controlled incore testing device, PSCINCORE device.
- Tests with the newly developed material testing devices in air, BWR environment and inside the reactor core of the test reactor.
- Typical test results and calculations for the material design parameters such as K, J da/dt etc. and comparison of the test results to literature.

2. Fracture mechanics

According to Anderson [1], fracture mechanics can be divided into many parts like linear-elastic and elastic plastic-fracture mechanics as shown in Figure 1. Actually these fields describes how structural materials behave under different levels of the applied load. In the linear-elastic case there is not or not a significant amount of plastic deformation in the structural material, whereas in the elastic-plastic case structural materials have to work under significant plasticity. [1]
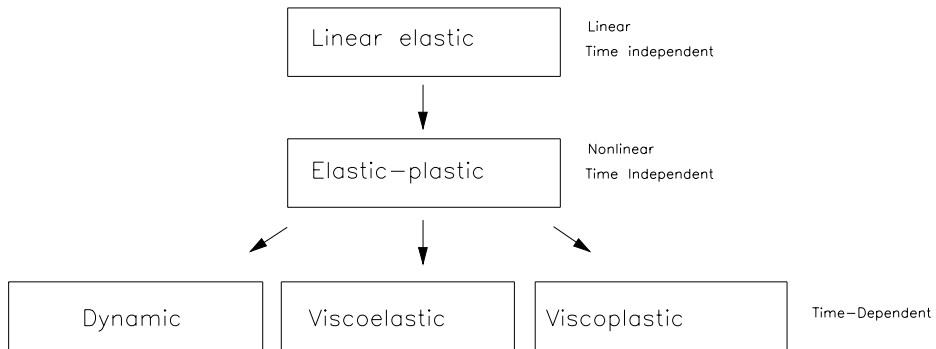
Figure 1. Simplified family tree of fracture mechanics. [1]

Fracture mechanics is based on two approaches i.e. the energy criterion and the stress intensity factor (K). In 1920, Griffith [2] showed that according to the First Law of Thermodynamics, when a system goes from non equilibrium to equilibrium, there will be a net decrease in energy [2]. In 1956 Irwin proposed an energy approach for fracture based on Griffith's earlier model [3]. According to Irwin, the energy release rate can be written as:

$$G = \frac{d\Pi}{dA}$$
(1)

where Π is the potential energy of an elastic specimen body and dA is the crack area. [3]

When material breaks, the material fracture toughness should be the same as the critical energy release rate G_c, i.e., $G = G_c$.

For the elliptical crack in an infinite plate the energy release rate can be written as:

$$G_c = \frac{\pi \sigma_f^2 a_c}{E} \qquad (2)$$

where a = half of the crack length, σ = damage stress and E = Young's modulus. It is essential to note that G_c changes at the crack tip as a singularity of $1/r^{1/2}$. Singularity has been described later in this chapter. [1,2,3,16]

2.1 Stresses and strains at crack tip

Westergaard [4], Irwin [5], Sneddon [6] and Williams [7] have made a number of investigations on crack tip stress fields. According to them, the stress fields of elastic cracked specimen (see Figure 2.) can be written as:

$$\sigma_{ij} = \left(\frac{k}{\sqrt{r}}\right) f_{ij}(0) + \sum_{m=0}^{\infty} A_m r^{\frac{m}{2}} g_{ij}^{(m)}(\theta) \qquad (3)$$

where σ_{ij} is stress tensor, θ and r are as defined in Figure 2 i.e. distance from crack tip, k is constant and f_{ij} is a dimensionless function of θ. The higher terms of formula (3) depend on the geometry of the specimen, but for every given configuration the first term is proportional to $1/\sqrt{r}$. When r → 0 the main term approaches infinity but other terms remain finite or approach zero. Thus $1/\sqrt{r}$ describes stress singularity at the crack tip, i.e., the stress is proportional to distance of $1/\sqrt{r}$ near the crack tip as shown in Figure 3. [4,5,6,7]

2.1.1 Crack tip stress intensity factor K and its singularity at crack tip

Stress intensity factor approach is based on the idea that the stress fields at crack tip can be distributed in a certain way that depends on the loading mode. Mode I loading tries to open crack tip, mode II is in plane shear loading and mode III is out-of-plane shear. Every loading mode generates stress singularity $1/(r)^{1/2}$ nearest to the crack tip but proportionality k and f_{ij} depend on loading mode.

Thus stress field at elastic material crack tip which is generated by using mode I loading can be written as:

$$\lim_{r \to 0} \sigma_{ij}^{I} = \frac{K_{I}}{\sqrt{2\pi r}} f_{ij}^{(I)}(\theta) \qquad (4)$$

where r is the distance of the stress field from crack tip (polar co ordinate), σ is stress component, θ is angle between crack tip and stress field (see Figure 2). [1, 16]
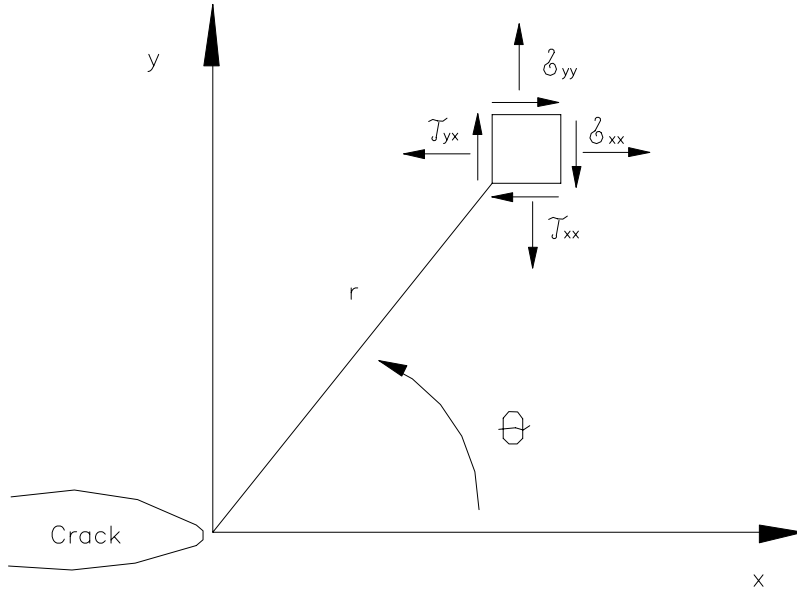
Figure 2. Stress fields at crack tip (in-plane) for on elastic material. [1, 16]

Stress fields (Figure 2) which are generated by using mode I loading can be described by the following formulas (5)–(7):

$$\sigma_{xx} = \frac{K_{1}}{\sqrt{2\pi r}} \cos\left(\frac{\theta}{2}\right)\left[1 - \sin\left(\frac{\theta}{2}\right) - \sin\left(\frac{3\theta}{2}\right)\right] \qquad (5)$$

$$\sigma_{yy} = \frac{K_{1}}{\sqrt{2\pi r}} \cos\left(\frac{\theta}{2}\right)\left[1 + \sin\left(\frac{\theta}{2}\right) - \sin\left(\frac{3\theta}{2}\right)\right] \qquad (6)$$

20

$$\tau_{xy} = \frac{K_1}{\sqrt{2\pi r}} \cos\left(\frac{\theta}{2}\right) \sin\left(\frac{\theta}{2}\right) \cos\left(\frac{3\theta}{2}\right) \tag{7}$$

$$\sigma_{zz} = 0 \,(plane\,stress)$$

$$\tau_{xz,yz} = 0$$

where σ and τ are stresses, r is the stress field distance from origin and θ is the angle for stress fields. Every stress field is proportional to constant K_1 and if this constant is known, all crack tip stress field distributions can be determined by using formulas 5,6 and 7. The idea is that local material damage can occur when a combination of stresses and strains reaches the critical value. This value is stress intensity factor K_{IC}, i.e., critical fracture toughness for elastic material. In the case of a large plate with crack located in the middle of the plate the fracture toughness can be written as:

$$K_I = \sigma\sqrt{\pi a} \tag{8}$$

where σ is stress and a is the crack length

When $K_I = K_{IC}$ material breaks. K is assumed not to be dependent on the size of the specimen. [1]

The relationship between K and G can be written as:

$$G = \frac{K_I^{\,2}}{E} \tag{9}$$

Note, that formula (9) is valid only for elastic materials. Schematic presentation of the crack tip singularity of an elastic material is shown in Figure 3.

According to Figure 3 there is a region very close to the crack tip in which the stress field can be described by using formula $K_I/\sqrt{2\pi r}$ (mode I loading and θ is zero). K based singularity does not exist anymore at a greater distance from the crack tip, as shown in Figure 3. [1, 16]
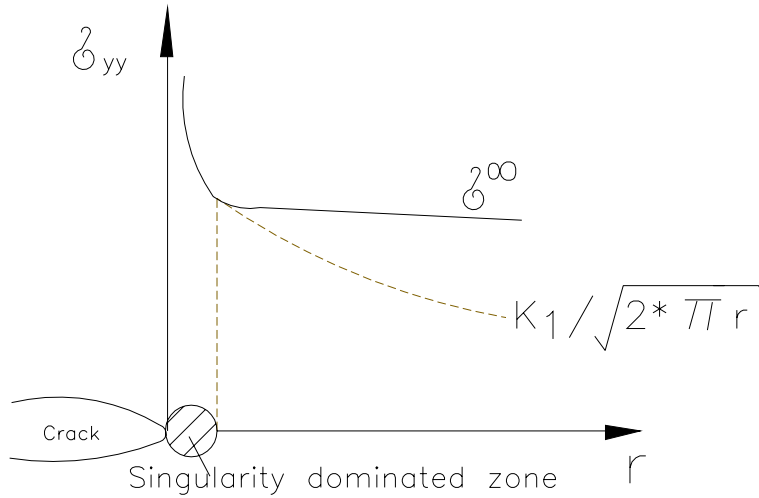
Figure 3. Crack tip singularity for elastic material. [1]

For example, if the cracked structure is subjected to a uniform remote tensile stress, σ_{yy} approaches a constant value σ_∞, as shown in Figure 3 [1].

2.1.2 Plasticity of the crack tip

In many cases structural materials are used in the plastic region, in which K is not described by the crack tip stress fields. When the amount of plasticity is very small K_{eff} can be described as shown in Figure 4; the small plasticity at crack tip can change the crack tip stress field. The idea is that material's elastic durability is decreased and singularity is increased as shown in Figure 4. Irwin [3] has performed a first order estimate for the size of the plastic zone:

$$r_y = \frac{1}{2\pi}\left(\frac{K_1^2}{\sigma_{ys}}\right) \qquad (10)$$

If we neglect strain hardening, the stress distribution for $r \ll r_y$ can be represented by a horizontal line at $\sigma_{yy} = \sigma_{ys}$, as Figure 4 illustrates; the stress singularity is truncated by yielding at the crack tip.
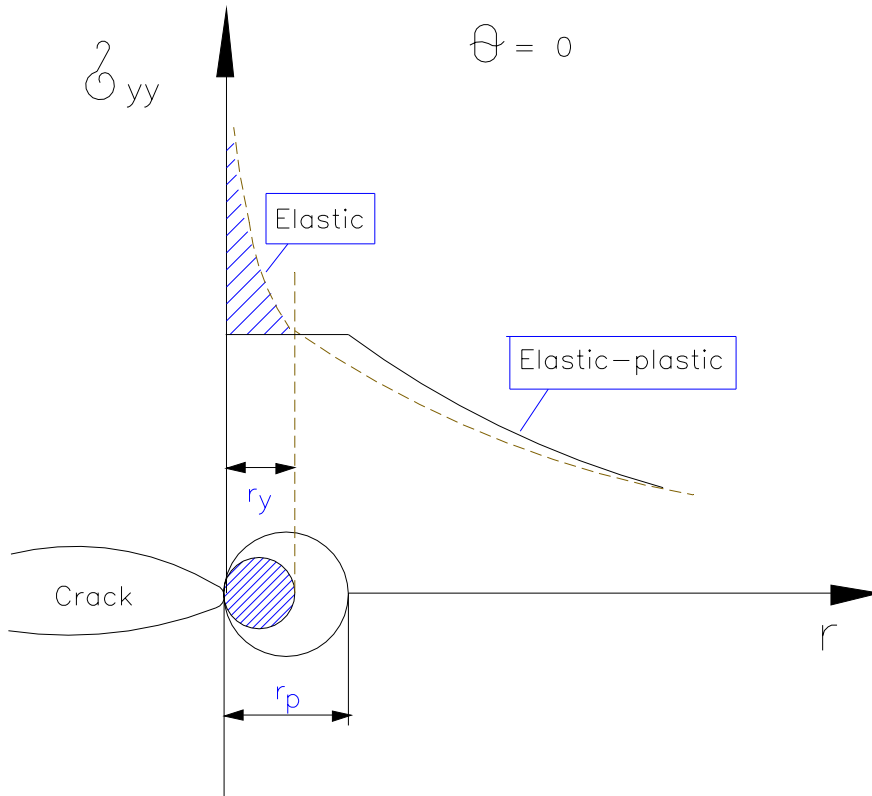
Figure 4. The first order and second order estimations for crack tips plastic zone. [3]

Material stress fields have to be distributed in a different way as shown in Figure 4 (hatched area). According to Figure 4, the elastic load carrying capacity is collapsed and because of that the size of the plastic zone is increased. According to Irwin, the second order estimate for crack tip plasticity can be written as:

$$r_p = \frac{1}{\pi} \left(\frac{K_1}{\sigma_{ys}} \right)^2 \qquad (11)$$

which is around two times the first order estimate r_y.

Accordingly the crack length in the case of a small amount of plasticity can be written as:

$$a_{eff} = a + r_y \qquad (12)$$

Furthermore, the stress intensity factor in the case of a small amount of plasticity can be written as:

$$K_{eff} = \lambda\left(a_{eff}\right)\sigma\sqrt{\pi a_{eff}} \qquad (13)$$

where λ is the geometrical correction factor. [3]

2.1.3 Specimen size versus constraint

As mentioned above, it has been proposed that at crack tip certain stress and strain conditions have to be established in elastic materials. Typically the stress and strain condition at crack tip is approached two dimensionally when one component of stress and strain is set at as zero. Let's assume a large plate without a crack which would be under two dimensional stress condition (plane stress state). In the case of a cracked specimen the area of the plane stress state can exist only a very long distance from the crack tip. Material near the crack tip is loaded to higher stress than the surrounding material. In Figure 5, a three dimensional stress field, i.e., plane strain state at the front of the crack tip is shown.

There is a large stress component which tries to contract the material in x and y directions near the crack tip as shown in Figure 5. This *constraint* is prevented by surrounding materials when a three dimensional stress condition (plane strain) near the crack tip can be achieved. Thus, when $r \leq B$ there is a plane strain inside the plane but at the surface of the plate the plane stress state exists because there is no stress that is normal for a free surface. Stress conditions depend on the ratio between the size of the plastic zone and the dimensions of the plate. If the plastic zone is small compared to the thickness of the plate, the plane strain condition should exist and if the plastic zone is of the same order of the thickness of the plate, the plane stress condition does exist. [1, 14]
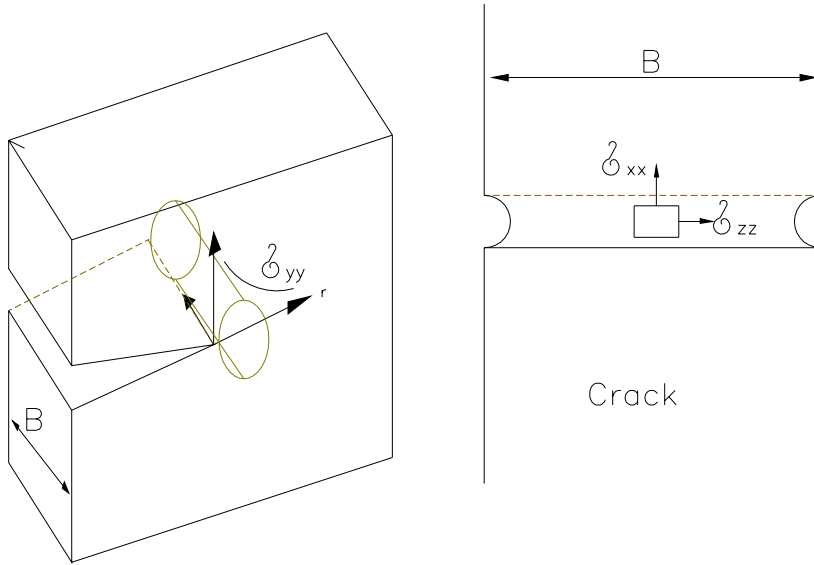
Figure 5. The stress field at crack tip. [1]

2.1.4 Specimen dimensions versus K-level

As described above, the plastic zone at the crack tip should be small in comparison to the thickness of the specimen. This can lead to a plane strain condition at the elastic plastic interface. When the plastic zone reaches a certain size in compared to the thickness of the specimen, the stress condition near the plastic surface is plane stress, but plane strain conditions can exist deep inside in plastic zone. The plane strain conditions can be relaxed when plastic deformation continues and this leads to a higher K value for the material. The size requirements have been set to guarantee that the plastic zone size is small enough so that plane strain conditions are maintained. According to ASTM 1152-87 [12] standard, the size requirements for the specimen can be written as:

$$a, B, (w-a) \geq 2,5 \left(\frac{K}{\sigma_{ys}} \right)^2 \qquad (14)$$

where a is the crack length, B is the thickness of the specimen and w-a is the unbreakable ligament of the specimen. [1, 12, 16]

2.2 Elastic plastic fracture mechanics

The rules for the linear-elastic fracture mechanics are valid as long as only a small amount of plastic deformation exists at the crack tip as described above. Elastic plastic fracture mechanics consists of investigations of plasticity of the crack tip that can be larger than in the case of the Linear Elastic Fracture Mechanics, (LEFM) . In the next chapters, two typical elastic plastic parameters, the Crack Tip Opening Displacement CTOD and the J-integral are presented. [1]

2.2.1 Crack Tip Opening Displacement (CTOD)

Wells [8] has performed many tests for different kind of materials and has noticed that many materials cannot carry out LEFM requirements. He noticed that when a sharp crack is growing it is blunts as shown in Figure 6. The rounding of the crack tip (blunting δ) is in proportion to the material toughness, i.e., CTOD = δ. A proposal based on this discovery has been made that crack blunting could be a fracture toughness parameter. Nowadays this parameter is the well known CTOD (Crack Tip Opening Displacement) parameter.
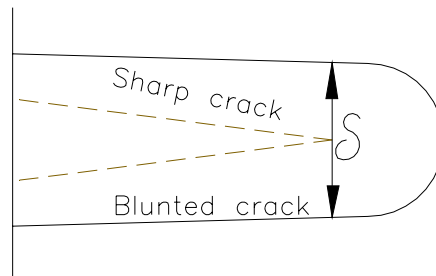
Figure 6. Crack tip blunting, CTOD fracture toughness .[8]

The relationship between Irwin's effective stress intensity factor K_{eff} and Well's CTOD is shown in Figure 7.
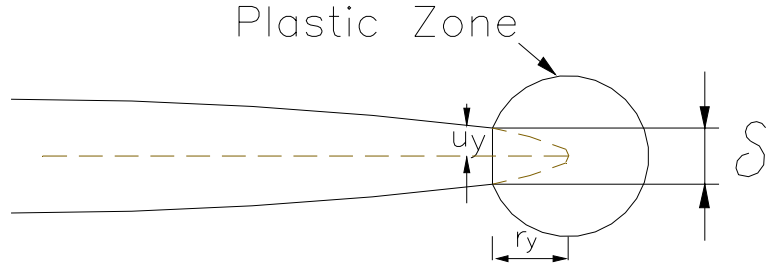
Figure 7. Plastic zone according to Irwin and CTOD parameters at crack tip.[1]

The distance u_y ($\delta=2u_y$) behind the effective crack can be written as;

$$u_y = \frac{\kappa+1}{2\mu} K_I \sqrt{\frac{r_y}{2\pi}} \tag{15}$$

According to Irwin, the correlation between plastic zone and crack length in plane stress condition can be written as:

$$r_y = \frac{1}{2\pi} \left(\frac{K_I}{\sigma_{ys}} \right)^2 \tag{16}$$

Combining (16) and (15) CTOD can be written as:

$$\delta = 2u_y = \frac{4}{\pi} \frac{K_I^2}{\sigma_{ys} E} \tag{17}$$

where, δ is CTOD and E is Young's modulus.

On the other hand, CTOD can be written according to energy release as follows:

$$\delta = \frac{4}{\pi} \frac{G}{\sigma_{ys}} \tag{18}$$

Thus, when the amount of plasticity is small, CTOD, G and K are related to each other.

There are also many other ways to derive formulas for CTOD such as the trip yield approach, etc.[1]

2.2.2 J-integral according to Rice

Rice [9] presented a path-independent contour integral for the analysis of cracks. He then showed that the value of this integral, which he called J, is equal to the energy release rate in a nonlinear elastic body that contains a crack [9]. According to Rice [9] J-integral for linear elastic materials is based on energy release rate according to the following formula;

$$J = \frac{d\Pi}{dA}$$ (19)

where Π is potential energy and dA is crack area. In the special case when material behaves according to linear elastic fracture mechanics there is a relationship between J and K_I which can be written as;

$$J = \frac{K_I^2}{E}$$ (20)

Note that this formula is valid only when loading mode I exists, i.e., loading tries to open the crack tip.

Furthermore, it is important to take into account that the energy release rate is determined as potential energy released from the structure when the crack grows in elastic material. In any case, a lot of strain energy, which is not accounted for in the case when crack grows or specimen is not loaded, is absorbed in elastic material. Thus, when the crack grows in elastic plastic material there is plastic imprint behind the crack. This means that the energy release rate is different compared to fully elastic case and J describes differences of energy rates which are absorbed inside the specimen. [9]

2.3 Stationary crack and stress singularities for different kind of materials

Hutchinson, [10] Rice and Rosengren [11] have independently showed that J can describe the features of the crack tip in non linear elastic materials. They have established a power law for plastic strain and stress. For example, in the case of elastic material this law for axial deformation can be written as;

$$\frac{\varepsilon}{\varepsilon_o} = \frac{\sigma}{\sigma_o} + \alpha \left(\frac{\sigma}{\sigma_0} \right)^n \qquad (21)$$

where σ_0 is a reference stress (typically yield stress), $\varepsilon_0 = \sigma_0/E$ and α are dimensionless constants and n is strain hardening exponent. This formula is also called as the Ramberg-Osgood formula and it is used to describe stress and strain in many cases (curve fitting).

Hutchinson [10], Rice and Rosengren [11] showed that in order to be a path independent case, stress and strain have to change according to $1/(r)^{1/2}$ singularity near the crack tip. The plastic zone elastic strain very close to the crack tip is small compared to the total strain. Thus stress and strain behavior is reduced to a simple power law. This situation leads to the following stress and strain variations in front of crack tip;

$$\sigma_{IJ} = k_1 \left(\frac{J}{r} \right)^{\frac{1}{n+1}} \qquad (22)$$

$$\varepsilon_{IJ} = k_2 \left(\frac{J}{r} \right)^{\frac{1}{n+1}} \qquad (23)$$

Where k_1 and k_2 are proportionality constants which are determined later for elastic materials. Formulas 22 and 23 can predict singularity $1/\sqrt{r}$ at crack tip as determined above. For active stress and strain distributions, boundary conditions can be written as;

$$\sigma_{IJ} = \sigma_0 \left(\frac{EJ}{\alpha \sigma_0^2 I_n r} \right)^{\frac{1}{n+1}} \tilde{\sigma}_{ij}(n,\theta) \tag{24}$$

$$\sigma_{IJ} = \frac{\alpha \sigma_0}{E} \left(\frac{EJ}{\alpha \sigma_0^2 I_n r} \right)^{\frac{1}{n+1}} \tilde{\varepsilon}_{ij}(n,\theta) \tag{25}$$

Where I_n is an integral constant that is dependent on n, $\tilde{\sigma}_{ij}$ ja $\tilde{\varepsilon}_{ij}$ are dimensionless functions of n and θ. These parameters depend on the state of stress condition i.e. plane strain or plane stress. Equations 24 and 25 are called the HRR singularity, named after Hutchinson [10], Rice and Rosengren. [11]

J-integral can be determined as the amplitude of HRR singularity in the same way as K can be determined in the case of elastic material as shown above. Thus J-integral completely describes the conditions within the plastic zone. Examples of crack tip singularities for different materials are shown in Fig. 8 (stationary cracks). In addition to singularities, there are also delineated areas in which different kinds of fracture mechanic parameters are valid. According to Figure 8a there is a large plastic region at close distance from the crack tip and in this area stress and strains cannot be described by using singularities (HRR or LEFM). In the case of small scale yielding, there is a J dominated region near the crack in which strain and stress can be followed by using $-1/(n+1)$ singularity. This J dominated region is surrounded by K dominated region in which stress and strain can be described by using singularity of $-1/\sqrt{r}$. In this case material behaves in a linear elastic way. [11]

The singularity field for an elastic plastic material is shown in Figure 8b. J dominated region with HRR singularity exists at the crack tip but LEFM singularity no longer exists because of the crack tip plasticity. In Figure 8c, the singularities for large scale yielding material are shown and in this case there is no way to describe crack tip condition by using K or J or singularities. [1]

a) Small scale yielding

b) Elastic–plastic conditions

c) Large scale yielding

Large strain region

J–dominated zone
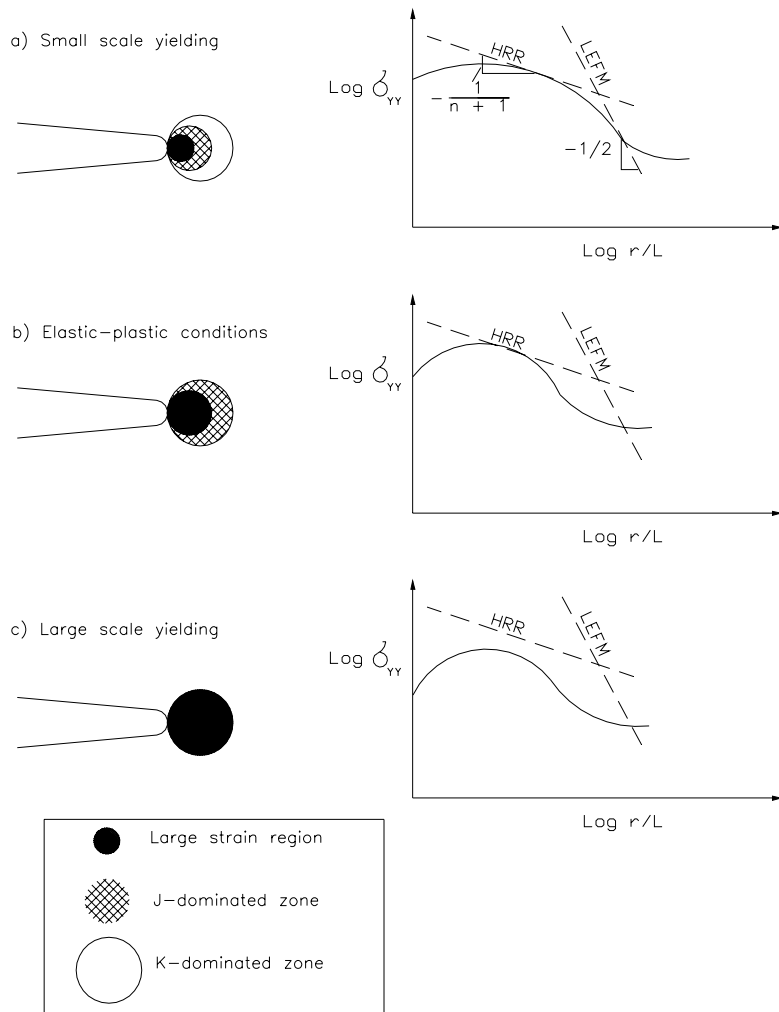
K–dominated zone

Figure 8. Effect of plasticity on the crack tip singularity fields for stationary crack. [1]

2.4   J-Integral for growing cracks

As described earlier, the specimen should have certain dimensions for J or K dominated zones to be generated in front of the crack tip. When crack growth rate is high compared to plane dimensions of the specimen, the single parameter assumptions are not valid. Prior crack growth does not affect purely elastic

31

materials because the local crack tip stress and strain fields depend only upon current conditions. But in the case of elastic plastic materials crack growth history can affect the stress and strain conditions at crack tip and therefore fails the assumption of a single parameter. Obviously there are two reasons for this breakdown of single parameter assumption namely elastic unloading and non-proportional stresses at the crack tip. Figure 9 illustrates crack growth in the elastic-plastic case. The elastic unloaded region behind the tip of the growing crack is obviously breaking the assumptions of deformation plasticity. Furthermore, the material directly in front of the crack tip is loaded with non proportional stresses, some stress components are increasing and some are even decreasing. When elastic unloading and non proportional plastic region are inside the J-dominated zone (in the case of small scale yielding) the single parameter assumptions are valid. When the crack is growing out of a J-dominated zone, single parameter assumption breaks down. [1]
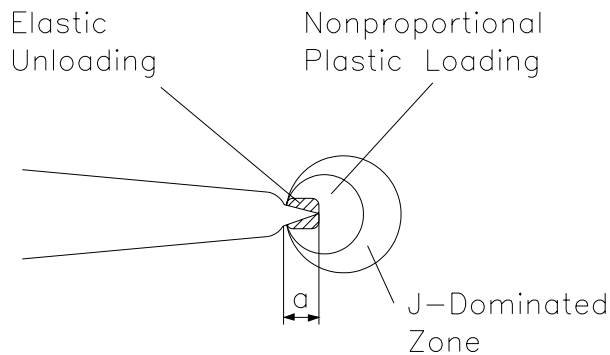
Figure 9. J-dominated growing crack.[1]

2.5 Specimen types for EAC testing

The selection of available SCC testing methods is very wide. The test methods range from qualitative tests, which are suitable for material screening, to quantitative tests, in which crack propagation rate is measured as a function of a loading parameter, e.g., stress intensity factor K_I. However, the distinction between the qualitative and quantitative methods is not very clear. Another way to classify the test methods is to divide them into smooth specimen testing and pre-cracked specimen testing.

2.5.1 Smooth specimen testing

SCC testing in smooth specimens includes both crack initiation and crack propagation. Crack initiation is a statistical process which may take a very long time. Tests can be accelerated using increased concentration of corrosive species, electrochemical stimulation or loading conditions more severe than what the material will experience in service conditions. Loading type can be divided into three categories: 1) constant strain, 2) constant load and 3) slow strain rate.

Typical constant strain (or -extension) test specimens are bent-beam, U-bend and C-ring specimens. The loading is a simple passive constant loading and can be provided by very simple fixtures, Figure 10a and 10b. In constant strain tests, the driving force for cracking decreases with increasing crack length. Constant load tests are usually performed on tensile type specimens, Figure 10 c. Similar specimens are used in slow strain rate tests. Active loading is provided by servo-hydraulic, pneumatic or stepper motor controlled loading machines. In both cases, the driving force for cracking increases with increasing crack length.

In addition to those presented here, several other specimen geometries are also used in SCC testing and also several other methods are used to provide the loading. A large number of both are presented as examples in references14 and 15.
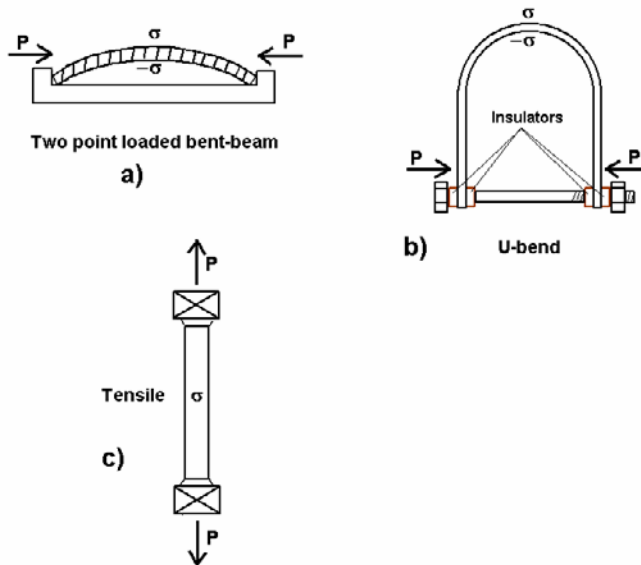
Figure 10. Typical smooth specimens used in SCC testing. [13, 14]

2.5.2   Pre-cracked specimen testing

Pre-cracking enables fracture mechanical stress analysis of the crack tip. Crack growth rate can be determined as a function of stress intensity factor K_I if the specimen fulfils the requirements of linear-elastic fracture mechanics, LEFM, as described above. Application of fracture mechanics enables prediction of the behavior of real components or structures. It is possible to predict when an existing crack reaches a critical size if the relation between the crack growth rate and K_I is known. LEFM applies if the size of the plastic zone is < 1/50 of specimen thickness or ligament length.

The tests are usually constant load tests (increasing K_I) or constant displacement tests (decreasing K_I). Because the linear-elastic fracture mechanics approach is usually applied in these tests, the specimens are quite large. Specimens are typically 25 mm (thickness) or larger CT-specimens (Compact Tension), Figure 11. Other geometries are also used, e.g., round CT, Double Cantilever Beam, Single Edge Notched Bend. Active load control is used in constant load tests, but passive loading can be used in constant displacement tests. Constant displacement can be achieved for example by using wedge loading. Wedge loading enables testing of several specimens at the same time quite easily. [13, 14]
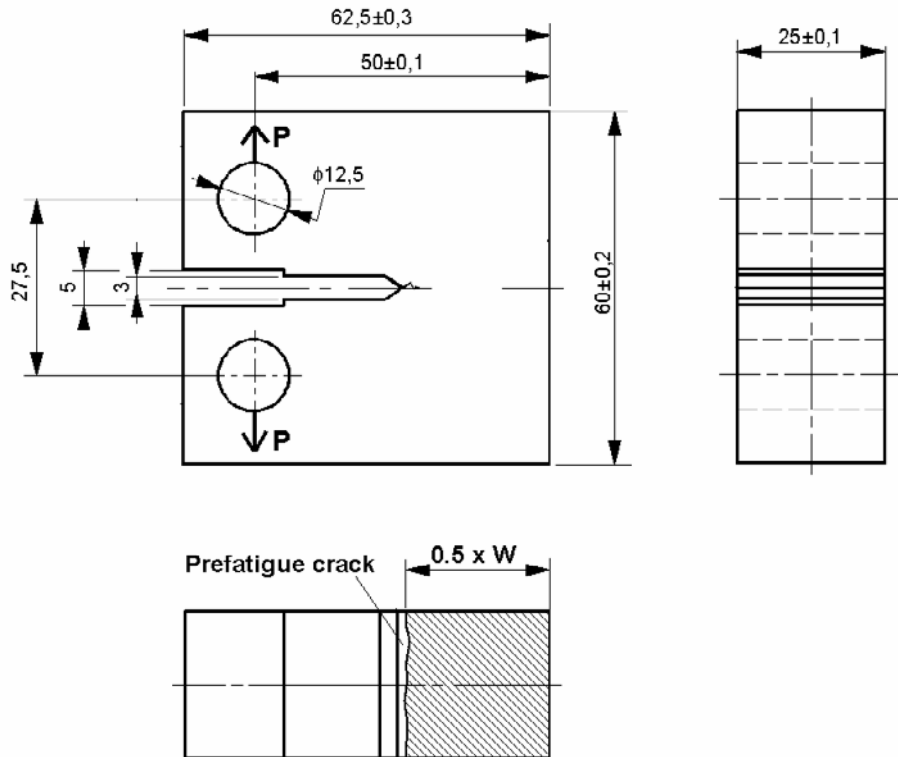
Figure 11. Typical dimensions (in millimeters) of a Compact Tension (CT) specimen used for quantitative stress corrosion crack growth rate measurements. [12, 13]

Crack growth rate vs. K_I is assumed to have three stages. At low K_I levels just above the threshold stress intensity factor, K_{ITH}, the crack growth rate is assumed to be strongly dependent on K_I. Above that, the crack growth rate is assumed to be relatively independent of K_I until the critical stress intensity factor, K_{IC}, is reached. At K_{IC}, the specimen fails mechanically. The crack growth rate vs. K_I behavior is presented schematically in Figure 12. It must be noted, however, that the behavior of different alloys in different environments varies. It also is not quite clear whether there really is a material-environment specific threshold stress intensity factor or not. [13, 14]
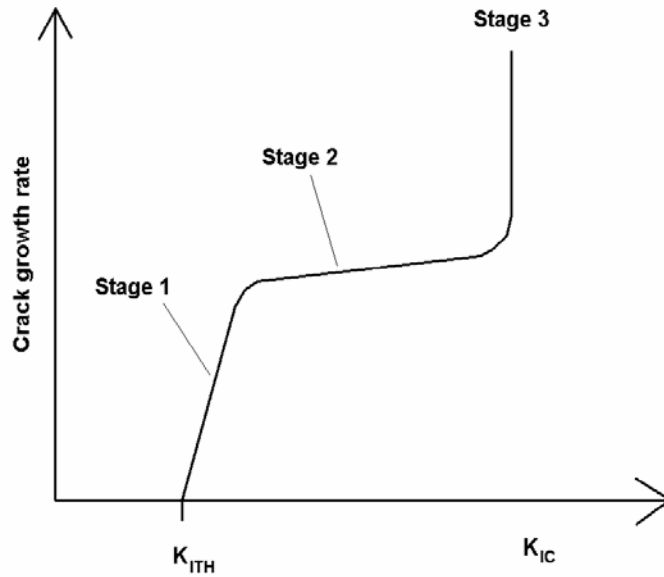
Figure 12. Schematic dependency between crack growth rate and stress intensity factor K_I. [13, 14]

If significant plasticity (plastic zone size is significantly proportional to the thickness or ligament length), the loading condition can be described using elastic-plastic loading parameters, e.g. J-integral. Tests are usually slow rising displacement tests on CT or single notched bend, SEN(B), specimens. To be able to present the loading level in K_I-units, J-integral can be converted to K scale using relation:

$$K_J = \sqrt{[J*E/(1-v^2)]} \qquad\qquad (26)$$

In equation 26, E is elastic modulus and v is Poisson's ratio. The subscript in K_J indicates that the K value has been determined from J-integral. Equation 26 applies because crack tip opening displacement, CTOD, is a function of K_I and J in linear-elastic loading conditions and the relation continues well into the elastic-plastic condition between CTOD and J. This approach is still in its development stage. [14, 15]

2.6 Specimen type effects for plasticity at crack tip

McClintock [15] has performed investigations for plane strain conditions at crack tip as a function of different kind of specimen configurations. Figure 13 summarizes some of these results. According to slip plane analysis, DENT specimen seems to have high three dimensional stress state on crack tip even in fully plastic conditions. An edge cracked plate in bending (Figure 13 c) exhibits slightly less stress elevation, with the maximum principal stress approximately 2.5 σ_0. A center cracked panel in pure tension cannot carry out significant amount of triaxiality under fully plastic condition. The results in Figure 13 indicate that, for nonhardening material under fully yielded conditions, stresses near the crack tip are not unique, but depend on geometry. Most laboratory measurements of fracture toughness are performed with bend type specimens, because these specimens present the fewest experimental difficulties [15].
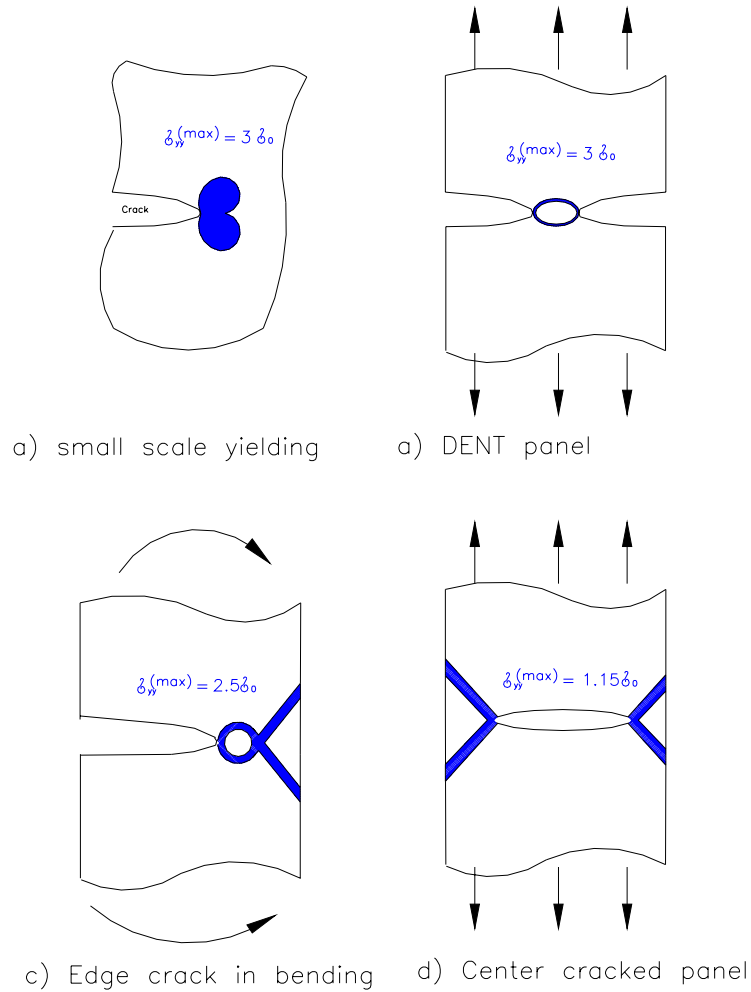
Figure 13. Comparison of the plastic deformation pattern in small scale yielding (a) with slip patterns under fully plastic conditions in three configurations [15].

2.7 Calculations for K and J according to ASTM 1152-87 standard

There is a number of different kind of tests to determine values for calculations of K, CTOD and J levels. Roughly, the test types can be divided up to two categories, single and multi specimen tests. In multi specimen tests, fracture mechanic parameters can be determined by using many specimens either

simultaneously or separately. The idea of this kind of test is to use one specimen to determine one specific K or J level with crack length therefore many specimens are needed to determine materials fracture resistance curve (K or J as a function of crack length). [12]

The type of test mostly used at VTT is a rising load test. The rising load test is a single specimen test, i.e., fracture resistance curve for material can be determined by using only one specimen. Either displacement or strain is controlled during the test and increased step by step linearly. Typically, K and J calculations from measurement data can be determined by using incremental methods i.e. temporary load, displacement and crack length points are used to determine fracture resistance curve. According to ASTM 1152-87 standard K and J levels can be determined by using the following formula:

$$K_{(i)} = \left[\frac{P_i S}{(BB_n)^{1/2} W^{3/2}}\right] f\left(\frac{a_i}{W}\right) \tag{27}$$

where W is specimen width, P is load, B is specimen thickness, B_n is the net thickness and S is span.

Function $f(a_i/W)$ in eq. (27) is a dimensionless function of momentary crack length a_i and specimen width W:

$$f\left(\frac{a_i}{W}\right) = \frac{3\left(\frac{a_i}{W}\right)^{1/2}\left[1.99 - \left(\frac{a_i}{W}\right)\left(1 - \left(\frac{a_i}{W}\right)\right)\left(2.15 - 3.93\left(\frac{a_i}{W}\right) + 2.7\left(\frac{a_i}{W}\right)^2\right)\right]}{2\left(1 + 2\left(\frac{a_i}{W}\right)\right)\left(1 - \left(\frac{a_i}{W}\right)\right)^{3/2}} \tag{28}$$

$$J_{el(i)} = \frac{K_i^2\left(1 - v^2\right)}{E} \tag{29}$$

$$J_{pl(i)} = \left[J_{pl(i-1)} + \left(\frac{\eta_{i-1}}{B_N b_{i-1}} \right) \frac{(P_i + P_{i-1})(\Delta_{i(pl)} - \Delta_{i-1(pl)})}{2} \right] \left[1 - \gamma_{i-1} \frac{a_i - a_{i-1}}{b_{i-1}} \right]$$

(30)

where P_i is load, a_i momentary crack length, $\Delta_{i(pl)}$ is distance for plastic load line, $\gamma_i = 1$ for SENB specimen and $\eta_i = 2$ for SENB specimen, b_i = momentary ligament length, b_0 is calculated ligament length. [12]

3. Fatigue damage of materials

3.1 Resolved stress and strain for single crystal

The basic parameters for the fatigue process of materials are described by using a ductile single crystal tensile specimen as shown in Figure 14. Figure 14 shows that the loaded specimen is subject to a directed main force P which generates vectors n and b acting on a slip plane (A) inside of the specimen. [16,17]
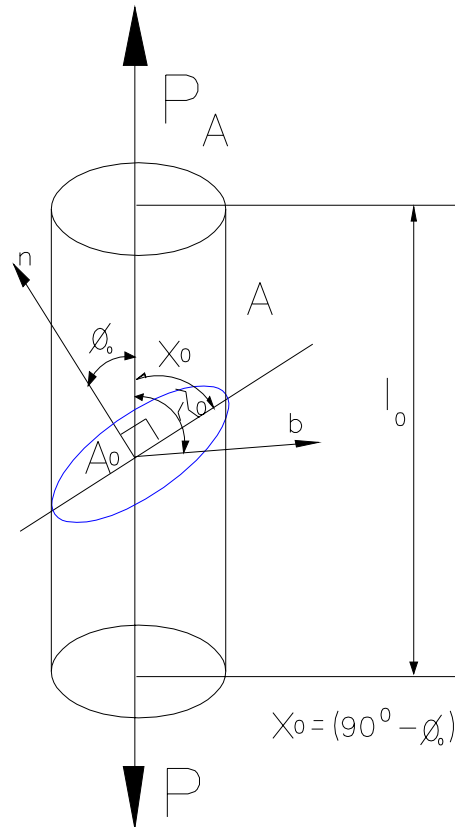
Figure 14. The parameters describing a crystallographic slip plane in a single crystal tensile specimen.[17]

According to Figure 14, the so called resolved shear stress and strain can be calculated with help of vectors b, n and angles $\lambda_0, \phi_0 \ and \ x_0$. Shear stress on the slip plane of the specimen can be written as (31):

$$\tau_{R_0} = \frac{P}{A}\cos\phi_0 \cos\lambda_0 = \sigma\cos\phi_0 \cos\lambda_0 \tag{31}$$

where slip area is $A_0 = A/\cos\phi_0$, where A is the initial specimen cross section area.

According to Schmid law the, plasticity of the specimen takes place when shear stress (τ_{R_0}) reaches the critical value (τ_c), which can then be written as:

$$\sigma\cos\phi_0 \cos\lambda_0 = \sigma\sin x_0 \cos\lambda_0 = M\sigma = \tau_c \tag{32}$$

where M is the Schmid factor, which is a maximum of 0.5 when $\phi_0, \lambda_0 = 45^o$.

During plastic loading of the specimen parameters $l_0, x_0 \, and \, \lambda_0$ are changed and resolved shear strain (γ_R) can be solved from the following formula:

$$\gamma_R = \frac{1}{\cos\phi_0}\left\{\left(\sqrt{\frac{l}{l_0}}\right)^2 - \sin^2\lambda_0 - \cos\lambda_0\right\} \tag{33}$$

where l_0 is the original specimen length and l is the length after the loading process.

Because of plastic deformation, $x_0 \, and \, \lambda_0$ are changed as follows:

$$\frac{d\gamma}{d\varepsilon} = \frac{\sigma}{\tau_R} = \frac{1}{M} = \frac{1}{\cos\phi\cos\lambda} \tag{34}$$

when $\phi = \lambda = 45^\circ, M = 0.5 \, and \, \tau_R = 0.5\sigma$

For resolved shear stress and strain can be written also as:

$$\tau_R = \frac{P}{A}\cos\phi_0 \sqrt{1 - (l_0 \sin\lambda_0 / l)^2} \tag{35}$$

$$\gamma_R = \frac{1}{\cos\phi_0} \left\{ \left(\sqrt{\frac{l}{l_0}} \right)^2 - \sin^2\lambda_0 - \cos\lambda_0 \right\} \quad (36)$$

Figure 15 shows resolved shear stress as a function of resolved shear strain for a FCC single crystal.
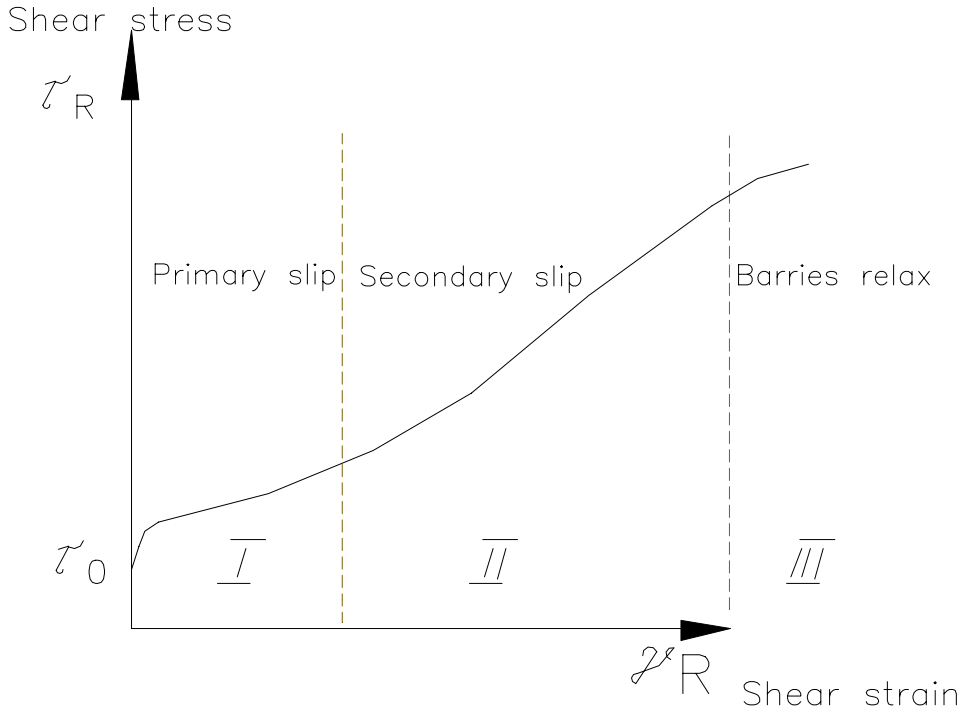
Figure 15. Resolved shear stress and strain curve for FCC single crystal.[17]

As described in Figure 15, resolved shear stress (τ_R) increases with strain of the specimen. It is important to notice that in the fully elastic case (beginning of the stage I) there is small geometrical change in the specimen. When the slip plane is turned at the end of the stage (I), secondary slip is activating and stage (II) in the stress strain curve in Figure 15 is starting. During stages (I) and (II), plastic deformation of the specimen can occur. Furthermore, during secondary slip the density of dislocations is increasing and at the beginning of the stage (III) dislocations can move inside the crystal by the cross sliding process. Therefore when deformation of the crystal is increasing dislocation barriers can be generated inside the crystal and thus resolved shear stress increases. At the

beginning of stage (III) in Figure 15, strain hardening rate of the single crystal decreases because of disengagement of dislocations from the barriers. [17]

3.2 Cyclic strain hardening and saturation of single crystal

When a single crystal specimen is loaded by using a fully reversed loading with constant amplitude, Figure 16 shows the resolved stress strain curve as a function of loading cycles. Resolved stress and strain curve consists of fast strain hardening area in the beginning of the test (during a few cycles). After certain number of the cycles (N_S) the stress strain curve has reached the quasi-steady stage, i.e., the stress strain loop (τ_S as a function of γ_{TS}) has a stabile configuration. [17]
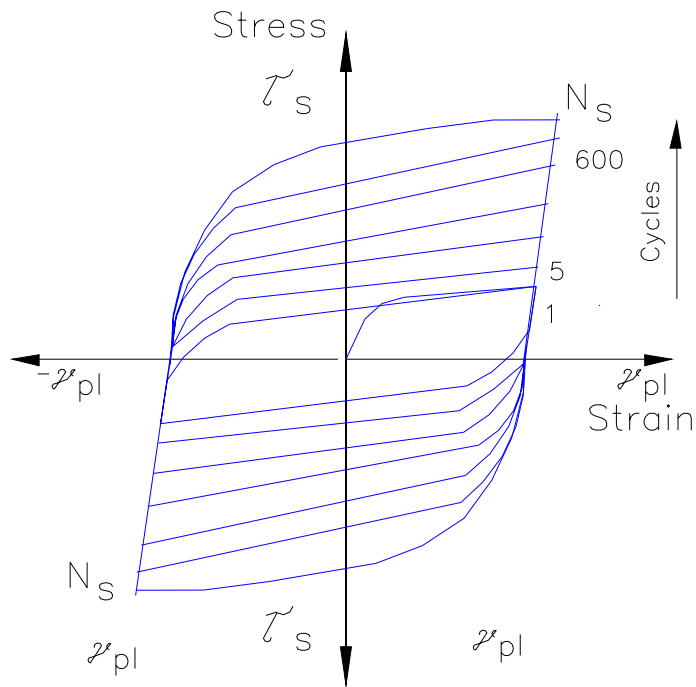
Figure 16. Resolved stress strain curve for single crystal specimen as a function of loading cycles. [17]

3.3 Fatigue with help of K and J

Paris et al. [18,19] (1960) have made a lot of investigations into fatigue. According to them, the fatigue process of materials can often be described by using fracture mechanics parameters such as K and J. The crack growth rate is a function of ΔK and R in linear elastic material and it can be written as:

$$\frac{da}{dN} = f_1(\Delta K, R))$$ (37)

Where $\Delta K = (K_{max} - K_{min})$, $R = K_{min}/K_{max}$, da/dN is crack growth/cycle. Many empirical formulas have been presented for the function $f_1(\Delta K, R)$.

The number of cycles depends on initial crack length a_0 and final crack length a_f, as shown in the next formula:

$$N = \int_{a_0}^{a_f} \frac{da}{f_1(\Delta K, R)}$$ (38)

Furthermore, if K_{max} and K_{min} are changed during the cyclic loading process, prior loading history can affect for number of cycles as follows:

$$\frac{da}{dN} = f_2(\Delta K, R, \chi))$$ (39)

where, χ is prior loading history, i.e., amount of the plasticity in the specimen. [18,19]

4. Environmental factors affecting crack growth rate

Environmentally assisted cracking (EAC) can be understood as a localised deformation process accelerated by local corrosion in addition to mechanical stresses or strains. The cracking of structural materials in nuclear power plants may proceed along grain boundaries, i.e. intergranularly (IGSCC), underlining the role of dissolution, or through the grains, i.e. transgranularly (TGSCC), underlining the role of mechanical loading. Generally, the two most studied occurrences of cracking have been that of sensitized stainless steel in BWRs and that of nickel-based alloys (especially Inconel alloy 600) in pressurized water reactors (PWR).

Linear elastic and elastic plastic fracture mechanics parameters such as K, J and CTOD can be used as described the stress and strain components at crack tip and thus give important information on specific material properties to designers. In many cases materials have to work in different environments such as high temperature water, under irradiation and in these cases EAC can be related to the failure mechanisms of materials in many ways as described later. In addition to basic parameters such as yield strength and fracture mechanics parameters such as K and J, designers should take into account many other things like the effect of potential level, oxide film properties, impurities of water and corrosion mechanisms.

Brossia and Kelly [20] have reported that alloying material can affect the structure of passive films on material surfaces; even crack tip chemistry and kinetics of electrochemistry can be consequence to EAC. Page *et al*. [21] have, on the other hand, reported that increasing dynamic strain at the crack tip can affect for the pH value of the electrolyte and thus changes chemical reaction kinetics. Furthermore, dynamic strain at crack tip can also break the oxide film and thus causes dissolution reactions at the crack tip. Plastic stresses have also been reported to affect faults density of the material. [20, 21]

Concerning the transport properties of the films on the crack wall surfaces within a crack, both electronic and ionic conductivity are of interest, because both anodic and cathodic reactions take place within the crack. The electronic

properties of the films within a crack are likely to be associated with the cathodic partial reaction that is most likely a reduction of a species in the solution. On the other hand, the protectiveness of the film (i.e. ionic transport properties of the film) is likely to be associated with the anodic oxide growth, because the growth requires transport of species through the oxide film. This is in contrast to the oxide films exposed to the bulk coolant, on which most probably cathodic reduction reactions of a species in the solution dominate. Therefore, the electronic transport properties of the films on the free surfaces are likely to play an important role. In addition, anodic reactions such as the transpassive dissolution of Cr as chromate may proceed at this external surface.

Special crack tip chemistry conditions are established, when trace amounts of anions are present in the BWR coolant and become enriched within a crack, as described in detail later. Possible routes for the influence of enriched anions in cracking are illustrated in Figure 17. Anions may influence both the conductivity and the pH of the coolant within the crack. In addition, they may influence the composition, structure and properties of the oxide films formed on crack walls either directly via adsorption or incorporation or indirectly via the effect of changes in pH. Certainly other routes may exist as well, such as possible changes in the composition and properties of the material in the crack tip region.
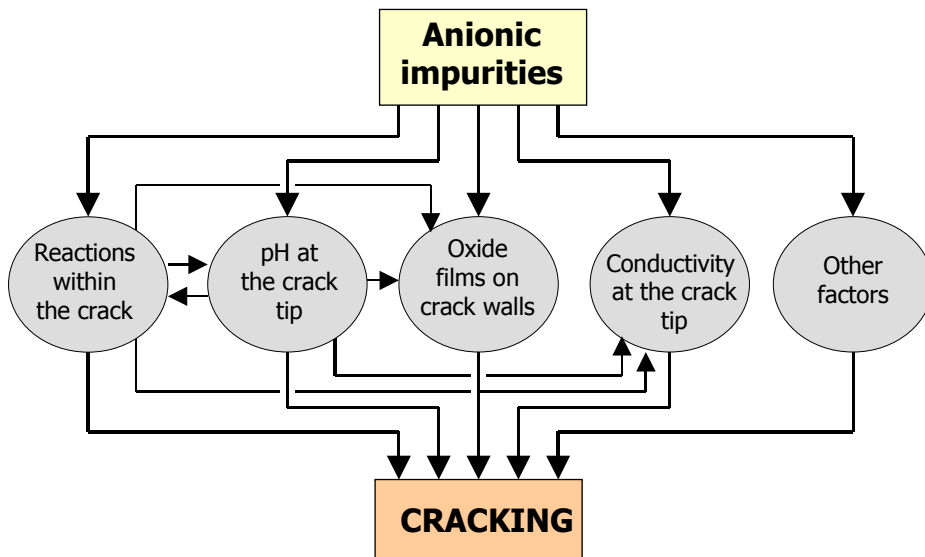
Figure 17. A sketch illustrating possible routes via which anions enriched inside a crack may influence cracking susceptibility of structural materials. [22]

4.1 Bulk environment in case of EAC

According to the results on modelling high-temperature aqueous corrosion, the properties of oxides are influenced by temperature, potential, electrolyte composition (presence of oxidising, reducing and/or complexing agents) and solution flow rate. To understand and to model the mechanisms of phenomena taking place on oxide surfaces and within oxide films, more experimental information is needed.

In the next chapter the basic issues which can affect the EAC such as properties of bulk water, ion mobility, temperature, flow rate, corrosion potential and impurities, have been introduced.

4.1.1 Viscosity of water and ion mobility

Water viscosity can have an affect on the diffusion coefficient and ion mobility in the coolant. The measurements for this parameter are difficult to perform at high temperature. Empirically produced data for water viscosity as a function of temperature is presented in Figure 18. Water density can vary as a function of temperature from steam to the normal density of 1 g/cm^3. It is obvious that at a density lies than 0.8 g/cm^3 and at temperatures higher than 400 ^{O}C, water viscosity as a function of temperature is only slightly positive and the isothermal curve can deviate a slightly from the linear curve. At a temperature of 500 ^{O}C and 3 kbar pressure, the water viscosity is only 10 % of water at room temperature. The diffusion factor and ion mobility are then around ten time higher than at room temperature. These factors can strongly affect the growth rate and the break down processes of the oxide layer. [23]
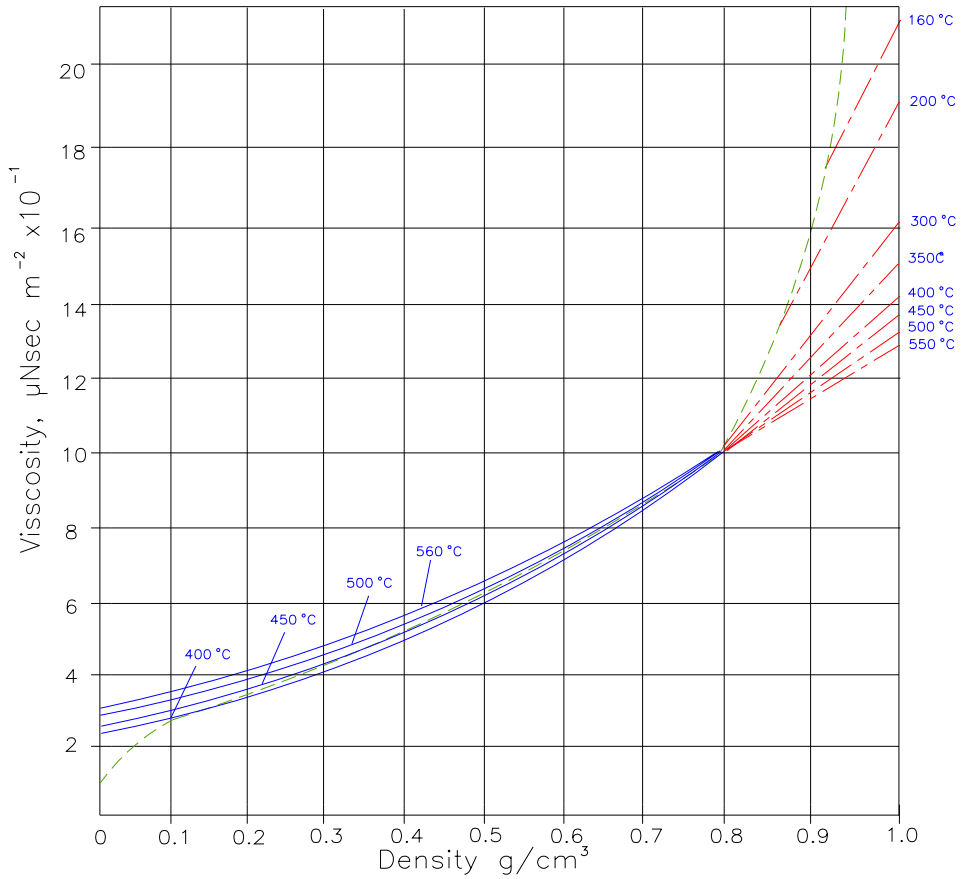
Figure 18. Water viscosity as a function of density at high temperature. [23]

4.1.2   Dielectric constant of water

Statistical dielectric constant describes electrolysis properties of high temperature water.

According to R. Gilmont et al., dielectric constant as a function of temperature can be written as (see Figure 19) [24]:

$$E=0.0007*t*10^7-10*t+87.861 \qquad (40)$$

where t is temperature (°C). [11]
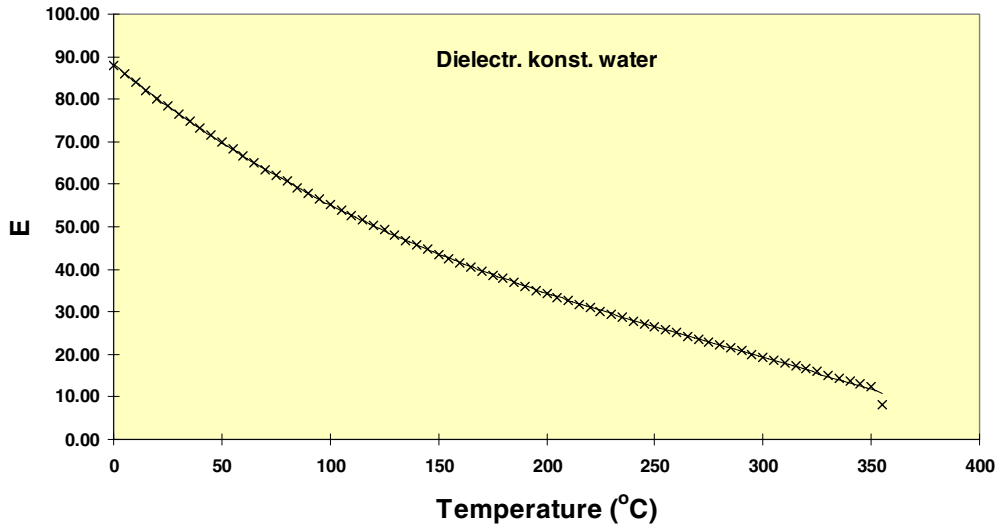
Figure 19. Dielectric constant as a function of temperature. [24]

Dielectric constant is a helpful tool to investigate the structure of the liquid. Furthermore, dielectric constant can also be used to derive Kirkwood correlation parameter (g) which describes unification of non coincidental water dipoles. This value is around 2.9 for liquid water at 0 °C and 1.0 for randomness distribution. The Kirkwood parameter as a function of water density is shown in Figure 20. [23]
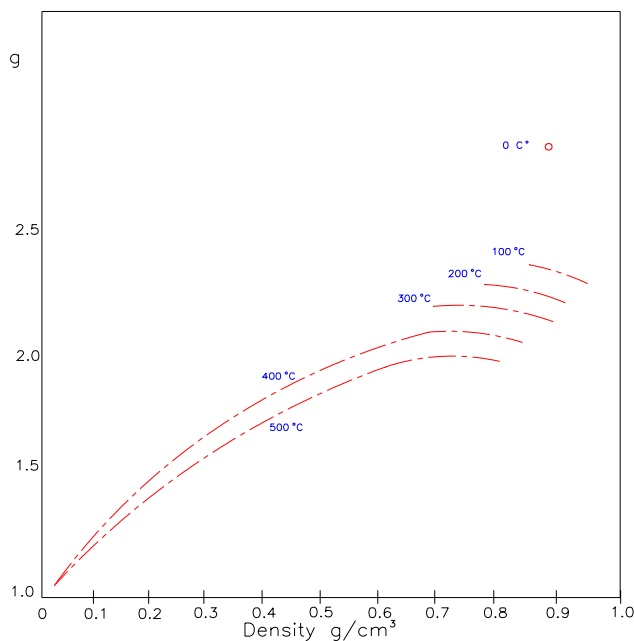
Figure 20. Kirkwood correlation parameter as a function of water density. [23]

Kirkwood correlation parameter can be used, for example, to investigate formation of the double layer (Helmholz) on the surface of the electrode. Figure 21 shows the double layer generation on the electrode surface in the case of negative and positive electrode potentials.

When the electrode potential is negative compared to the neutral charge potential its surface charge is also negative and thus cations and water dipoles are attracted to the surface of the electrode as shown in Figure 21. In the case of positively charged surface of the electrode (positive potential compared to the neutral charge potential) the orientation of the water dipoles changes as shown in Figure 21. Furthermore, hydrated anions will be attracted to the surface instead of cations. With Kirkwood correlation parameter the number of attracted water dipoles, i.e., thickness of the double layer at different temperatures can be estimated. [25]
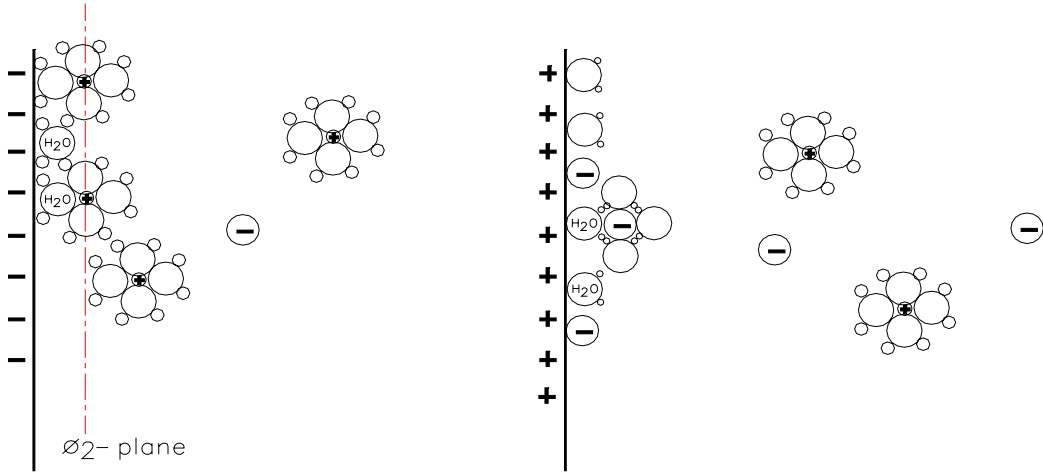
Figure 21. The generation of double layer on electrode surface .[25]

4.1.3 Water density, ionic dissociation Kw and pH change as a function of temperature

The concentration product between hydrogen and hydroxyl ions at room temperature water is 10^{-14} (mol/l)^2. When temperature and pressure increases the generation of ions also increases. Ionic dissociation, Kw, and water density as a function of temperature is shown in Figure 22. These parameters have been calculated by using the following formulas [24]:

$$Kw = -4.098 + (-\frac{3245.2}{(T+273.15)} + \left(\frac{(2.2363*10^5)}{(T+273.15)}\right)^2 + \left(\frac{(-3.8884*10^7)}{(T+273.15)}\right)^3 + \left(13.957 + \frac{(1262.3)}{T+273.15}\right) +$$

$$+\left(\frac{8.5641*10^5}{(T+273.15)}\right)^2 * Log(\delta) \qquad (41)$$

where T is temperature (K) and ρ the density of water.

Density can be calculated from the following formula:

52

$$\rho = 0.99781 + 0.002011 * T - 0.00019322 * T^2 + 6.7397 * 10^{-6} * T^3 - 1.22861 * 10^{-7} T^4 + \\ + 1.29322 * 10^{-9} * T^5 - -8.30187 * 10^{-12} * T^6 + 3.2997 * 10^{-14} * T^7 - 7.92295 * 10^{-17} * \\ * T^8 + 1.05247 * 10^{-18} T^9 - 5.93642 * 10^{-23} * T^{10}$$

$$(42)$$

where T is temperature (K).
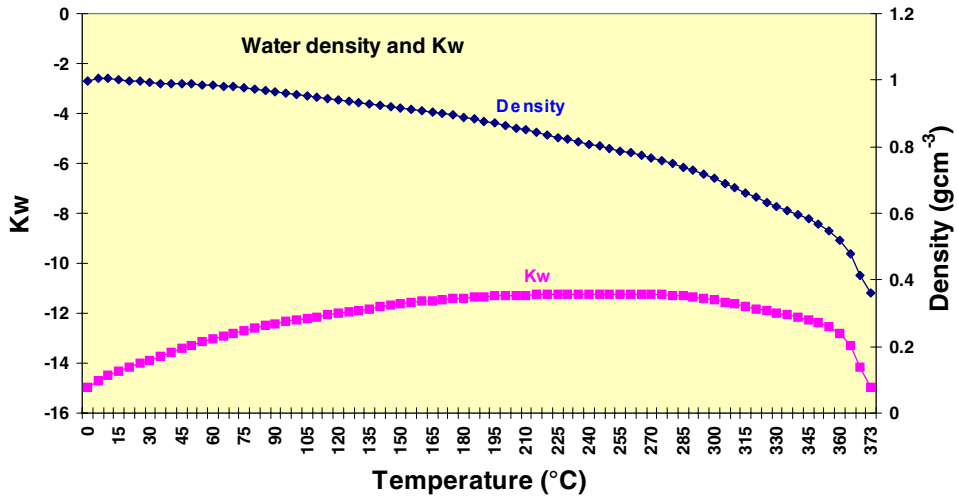
Figure 22. Kw and water density as a function of temperature. [24]

Furthermore, the relation between pH and Kw is shown in Figure 23. This curve has been calculated by using the following formula (42) [24] and Kw from equation (41):

$$pH = \frac{kW}{-2}$$

$$(43)$$
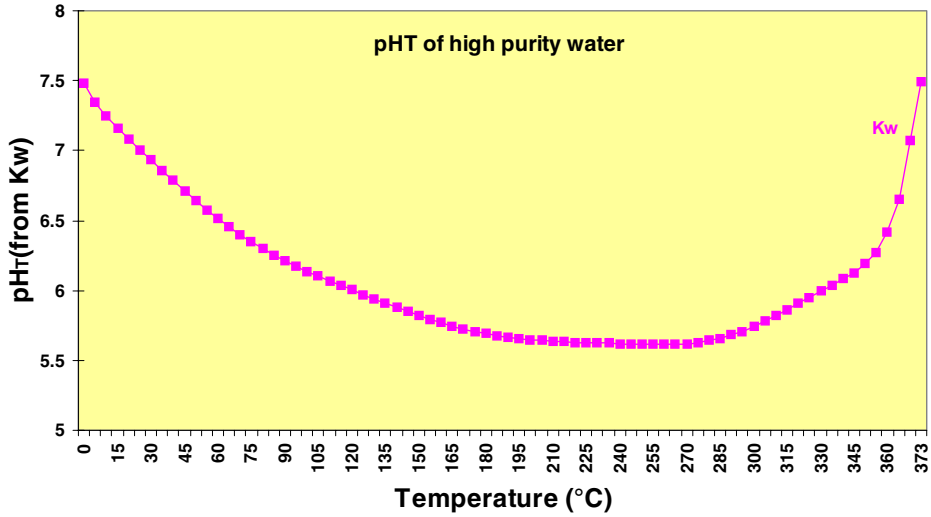
Figure 23. pH as a function of temperature according to Kw value. [24]

As described above, high temperature water properties can affect the EAC process in many ways. Generally, according to Figures 21–25 it can be said that:

1. pH = -log(H$^+$) so zero level for hydrogen electrode is changed as a function of temperature as described in Figure 23.
2. Standard potentials for different water solutions are not comparable without extra empirical correlation.
3. Water dissolution, ion mobility and water density can affect the structure of oxide films in a high temperature water as described later.

4.1.4 Flow rate effects of the coolant

Many opposite opinions on the effect of coolant flow rate on EAC can be found in literature (see also formation of crevice chemistry, presented in chapter 4). Typically, coolant flow rate effects should affect the corrosion potential and thus the fracture process of materials. According to Chai et. al. [26], crack growth rate is increased as a function of flow rate when the flow rate is < 5 cm/s and the oxygen level is around 100 ppb. This can effect the corrosion potential because the amount of the oxidizing species increases with increasing flow rate of the coolant. When the oxygen level of the coolant is more than 1000 ppb the flow rate does not seem to have any affect. In this case, when the oxygen level is high

enough, the corrosion potential can increase as a function of oxygen level without changes in the flowing rate. When the flow rate increases the mass transport from the crack should also increase and therefore have an effect on crack growth rate. [22]

According toTurnbull [27], a suitable flow rate of coolant forming in the same orientation as the crack can flush the crack and thus prevent the forming of the corrosion cell in the crack.

Clear evidences has been found that nucleation of IGSCC in water decreases as a function of increased flowing rate. This may occur when oxygen comes from the crack to other areas near the crack and repassivation processes can occur at free surfaces. [22]

4.1.5   Corrosion potential

Protection of stainless steel is based on the Cr content of the oxide layer formed on the material surface. There are couple of basic rules for passivation of stainless steel: 1) corrosion potential and 2) corrosion current density should be between certain limits. Passivation of stainless steel can happen when the redox potential (approximated potential of solution) is higher than E_{pas} (potential of the specimen) and the cathodic current density should is higher than i_{crit}, as shown in Figure 24.
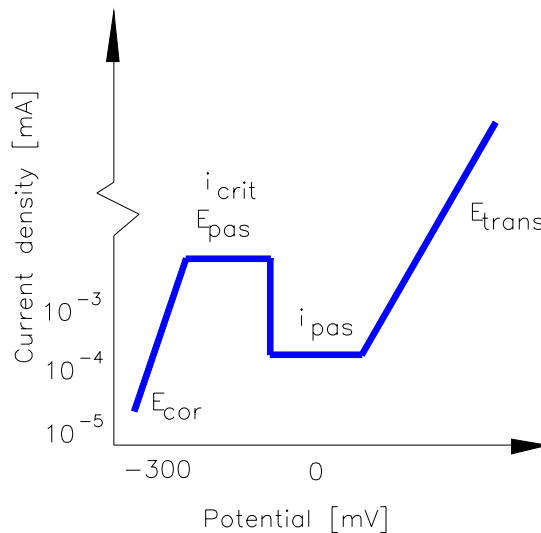
Figure 24. Corrosion current density as a function of potential. [28]

55

There are many investigations which have shown that an increased corrosion potential at 300 °C in water environment can strongly affect the crack growth rate in the case of sensitized AISI 304 stainless steel (see Figure 25). The corrosion potential depends on the level of oxygen and other oxidants in the coolant.
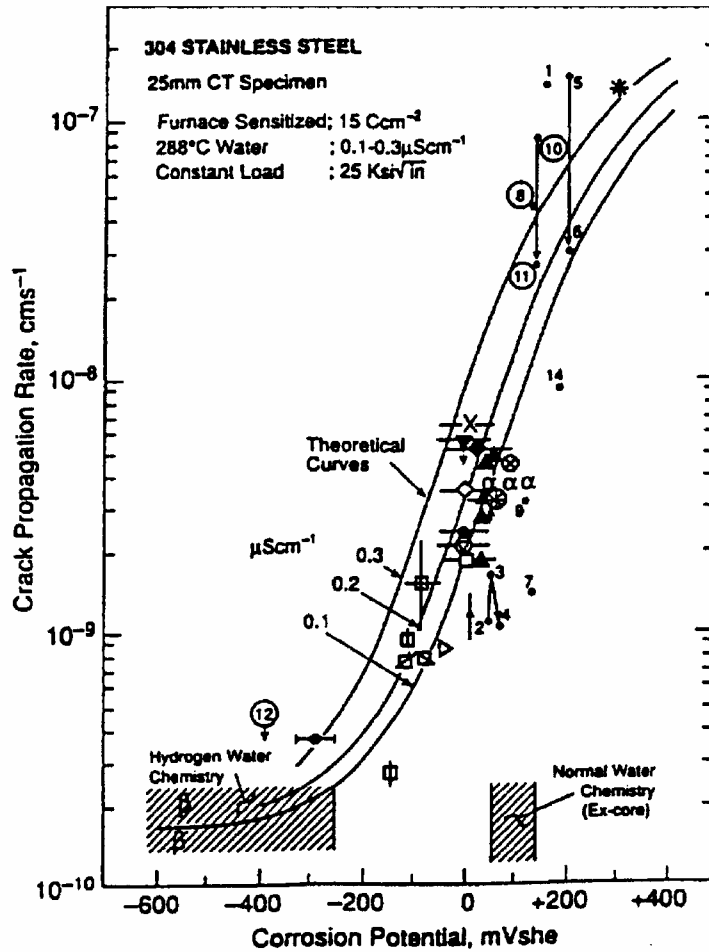
Figure 25. The influence of corrosion potential on the crack growth rate of sensitised stainless steel of type 304 [29].

As indicated in Figure 25, cracking of sensitised stainless steels in a BWR environment has been found to occur mainly above a threshold potential of around –0.23 V vs. SHE at 288 °C. This threshold potential value has been suggested to depend on temperature, loading rates, surface condition, solution

pH etc. Furthermore, according to Figure 25, even at high potentials such as -50 mV vs SHE, the crack growth rate of AISI 304 stainless steel is rather low when coolant purity is high [30].

4.1.6 Anionic impurities

Anionic impurities such as chloride, sulfate, carbonate, fluoride, chromate, nitrate and phosphate have in many cases been reported to increase the crack initiation and crack growth rate for stainless steel in water. These impurities can directly affect the conductivity of the coolant and increase further the crack growth rate for AISI 304 stainless steel as shown in Figure 26. [31, 32]
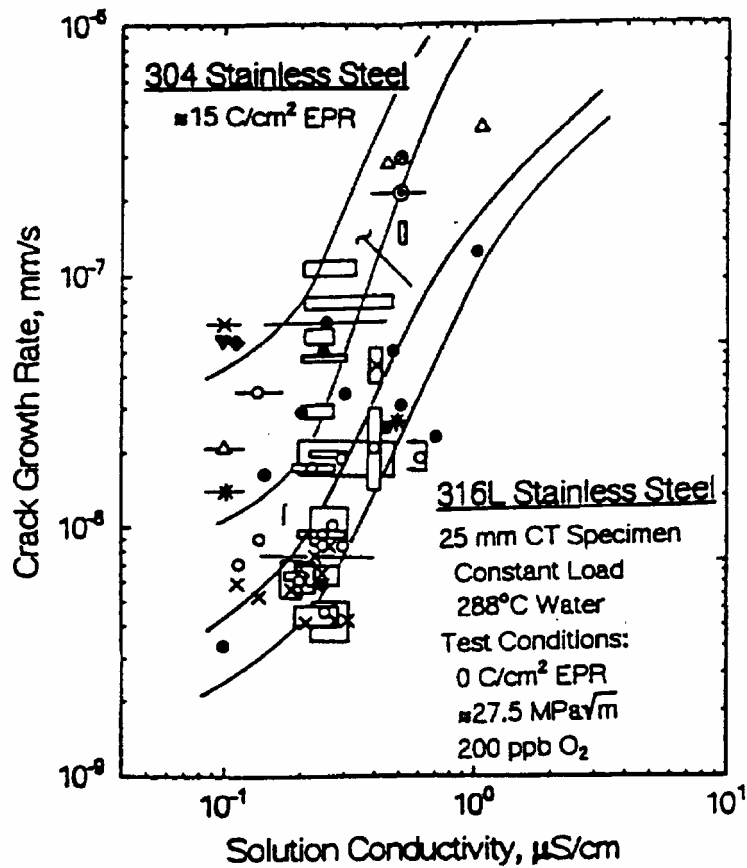
Figure 26. Correlation between the conductivity of the coolant and the crack growth rate of austenitic stainless steel of type AISI 304 and 316L [30].

A typical amount of anionic impurities in BWR coolant is around one to few ppb [17]. Andersson [27] has shown that the conductivity levels of BWR water has decreased from 0.2…1.0 µScm^{-1} to 0.12 µScm^{-1} during the 1970s and 1980s because of the development of coolant purification medhods. Specific impurities are likely to have different effects on the EAC susceptibility independent of their influence on conductivity and it is therefore important to know which ions are present in the water [30]. Clarifications and rules of thumb on the effect of different impurities can be looked for by comparing various experimental observations.

Ruther et al. [33] studied and ranked sodium salts and various acids at constant anion concentrations of 100 ppb in the following order with respect to their decreasing effect on the crack growth rate in stainless steels:

$Na_2S > Na_2SO_3 > Na_2SO_4 > Na_2S_2O_3 > NaOH > Na_2SiO_3 > Na_2HPO_4 > Na_3PO_4 > NaCl > Na_2CO_3 > Na_2B_4O_7 > NaNO_3 > H_2SO_3 > H_2SO_4 > HCl > H_2CO_3 > H_3PO_4 > HNO_3 > H_3BO_3 > H_2SiO_3$

This order is in fair agreement with the results of, for instance, Davis and Indig and Ljungberg et al. [34, 35, 36] and also partly with those of Sambongi et al. [37]. Ljunberg et al. have found that for sensitised AISI 304 stainless steel, sulphate is the most detrimental of the impurities considered. According to Ljungberg et al. [34, 35, 36], 100 ppb sulphate noticeably enhances IGSCC in NWC with 200 ppb oxygen, and at 1 ppm oxygen the effect is severe. In HWC (Hydrogen Water Chemistry) with 5 or 15 ppb oxygen, some IGSCC occurs at 25 ppb sulphate, and at 100 ppb sulphate cracking is nearly as severe as in pure NWC (Normal Water Chemistry). Chloride also severely enhances IGSCC. However, Ljungberg et al. have reported that to achieve similar effects as with sulphate in EAC tests using the constant elongation rate tensile (CERT) technique, 4 to 10 times as much chloride is needed. Ljungberg et al. have not found nitrate (200 ppb), carbon dioxide (1…10 ppm) or sodium carbonate (1 to 24 ppm) to have an increasing effect on crack growth rates, though the results of other experiments have indicated that nitrate and carbonate ions may enhance crack initiation. Also fluoride ions (F$^-$), SiO_2 and thiosulphate ions ($S_2O_3^{2-}$) have been found to be harmful.

Inconel alloys 600 and 182 seem to be affected by sulphate and chloride ions in the same way as sensitised AISI 304 stainless steel, but to a smaller degree. Also the results of Toivonen *et al.* [38] indicate that the addition of sulphate ions has a more profound effect on the crack growth of Inconel alloy 182 than on that of sensitised AISI 304.

4.1.7 Irradiation and material damages

Many types of high energy radiates are generated inside a reactor of the nuclear power plant:

- fast neutrons,
- electrons,
- alpha particles
- protons and
- x-ray etc.

This kind of high energy radiation can generate high energy particles (up to 2 MeV) which sweeps through the material and therefore affect material properties at the atomic scale. The speed of so called fast neutrons can be over $2x10^7$ m/s and they can hit atoms of the material and force them out of lattice structure. In an example for pure Cu, where an area 4 barn (1 barn = 10^{-28} m^2) is under irradiation for one day (10^5 s), the neutron flux is 10^{17} m^{-2}s^{-1} so the number of neutrons which are going trough the material is around 10^{22}nm^{-2}. In this case one Cu atom from 250 000 can get hit by a fast neutron. In many materials the knock out process is fully elastic and thus reserved energy, which is related to atomic mass, can vary between 0...E$_{max}$. Collision between a fast neutron and an atom can generate an energy density of 200000 eV. This energy can produce more knock out for atoms i.e. secondary and tertiary knock outs and thus more local damages to the material. In the case of Cu, a knock out atom moves through the material lattice until its energy decreases to 25 eV. [39]

Material damage which is caused by knock out process typically consists of interstitial atoms and vacancies in the lattice. The area of the damage can be around 60 000 atoms and its structure consists of vacancies (in the middle of the lattice) and interstitial (at the edge zone of the lattice) as shown in Figure 27.
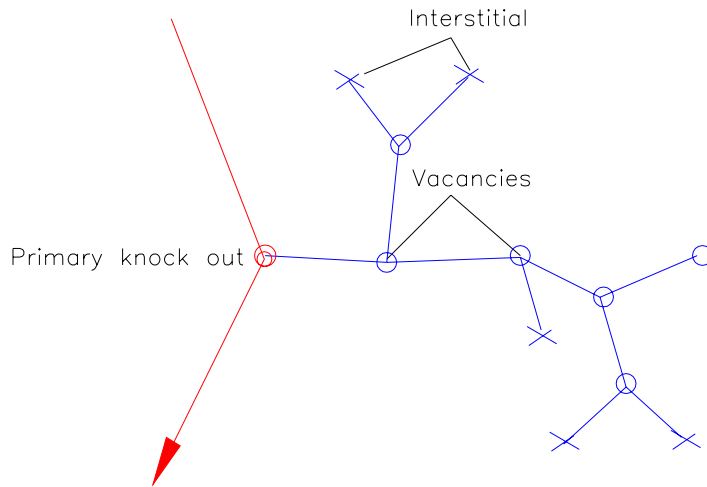
Figure 27. Knock out process for generating vacancies and interstitial at lattice of atom. [39]

One knock out can generate around 1000 pairs of vacancies and interstitial atoms. Part of the generated damage can be repaired by annealing processes with thermal movement of atoms. At low temperature most of the vacancies and interstitials are annihilated again for a new combination of structure as shown in Figure 27.

There is also another way to generate material damages under irradiation. Energy dissolution which comes from the oscillation movement of atoms can move the atom position in the lattice and thus increase its temperature. Thermal spike can locally increase the temperature over 1000 °C at lattice and thus affect the annealing process between vacancies and interstitial. Furthermore, this high local temperature can affect the phase structure of the material, i.e., the microstructure of the material can change due to the martensite reaction.

Transmutation products such as krypton and neon can be generated with the help of slow neutrons. Together with these inert gases vacancies can produce voids and cracks in the material. On the other hand, these inert gases consist of very high energy particles, e.g. alpha particles, which can be the energy source for the knock out phenomenon. For example, heavy ions are energy sources of up to several keV, which can affect the material properties and durability. [39]

Irradiation assisted stress corrosion cracking has been reported to occur as intergranular cracking in austenitic stainless steels in BWR environments at neutron fluences above 5×10^{20} n/cm^2 (E > 1 MeV), corresponding to about 0.7 dpa (displacements per atom). The threshold fluence for increased risk of intergranular irradiation assisted cracking in PWR environment is suspected to be clearly higher, 3 dpa or more. In oxidising BWR environment, the role of corrosion in IASCC is evidently important, but in hydrogen containing PWR environment corrosion should not be as decisive. Possible additional factors promoting intergranular cracking are radiation-induced hardening, radiation-induced creep and grain boundary segregation together with hydrogen embrittlement. Swelling, formation of helium bubbles and radiation-induced precipitation may also become an issue, especially at higher irradiation temperatures or at higher neutron fluences. [88]

4.2 The crack tip chemistry

The chemical conditions within a stress corrosion crack may differ markedly from those in the bulk coolant, and this most probably plays an important role in regard to crack propagation. Several authors have described the physical and chemical phenomena taking place within a crack during crack growth [31, 40, 41, 42, 43, 44, 45, etc.]. These phenomena lead to the establishment of special water chemistry conditions that are often identified as occluded water chemistry. Increased crack growth rates have been ascribed primarily to the occluded chemistry conditions and not to the presence of high amounts of oxygen or high corrosion potential within a crack [34].

Two main processes in the establishment of special crack tip conditions are the formation of oxygen-free regions and the oxidation of the metal at the crack tip. The former is due to consumption of oxygen in cathodic reactions and the mass transfer limitations preventing additional oxygen from entering the crack. The latter is a result of exposure of bare metal surface or of non-protective oxide film to the coolant within the crack. These main processes leading to special conditions are closely similar to those discussed when modelling crevice corrosion.

Obtaining information of conditions within the crack is both highly important and very difficult. Turnbull [45] has commented that the major factor hindering progress in the modelling and validation of the developed models for cracking is the difficulty in quantifying the local environment and the kinetics of reaction processes at the crack tip. It has been attempted to assess the chemical conditions within a stress corrosion crack through measurements of solution chemistry in real cracks based on micro sampling techniques [46, 47, 48], measurements of solution chemistry, pH and/or potential in artificial or simulated cracks or crevices [49, 50, 51, 52, 53, 54, 55, 56, 57] and mathematical modelling of the reactions and transport phenomena within cracks or crevices [57, 58, 59, 60, 61]. Recent attempts to study the influence of potential within the crack have been based on micro-polarisation of the crack tip and micro-reference electrodes.

As illustrated in Figure 17, the influence of anions can take place via the solution or by affecting on the composition and properties of the oxide films on crack walls. The influence of crack tip conditions can thus be discussed from different viewpoints:

- Enrichment of anions leads to changes in the conductivity of the coolant within the crack, which in turn may affect the magnitude of the IR drop in the solution within the crack.
- Changes in the chemical environment and pH lead to changes in the reaction and dissolution equilibria and reaction kinetics within the crack.
- The enrichment of oxidising anionic impurities such as $SO_4{}^{2-}$, $NO_3{}^-$ and $CrO_4{}^-$ may lead to increased oxidation of the material within the crack.
- The changes in the environment and possible adsorption or incorporation of impurities may have a strong influence on the protective properties of the oxide films on the crack walls [46]–[61].

4.3 Fe-Cr-Ni-alloys at high temperature water

Austenitic type stainless steel is most typically used in a high temperature water environment. The basic alloys for this kind of austenitic stainless steel is 18-8 Cr-Ni (AISI 304 category). The oxide layer which is formed on the surface of

austenitic stainless steel in a high temperature water environment can be multi layers of Fe_3O_4, Cr_3O_4 in vacuum (no oxygen) or Ni_3O_4 and Cr_2O_3 or Fe_2O_3 in a gas environment with oxygen. The effect of Cr content in iron alloys on the structure of the oxide film is shown in Figure 28. The oxide layer consists of spinel structure and solid solutions. To generate these products diffusion between Cr oxide and cation holes should take place. $FeCr_2O_4$ can, depending on the Cr content, form in the FeO layer decreasing the mobility of Fe^{2+} and causing the Fe_3O_4 layer to increase due to the reduction of the FeO layer. [62]
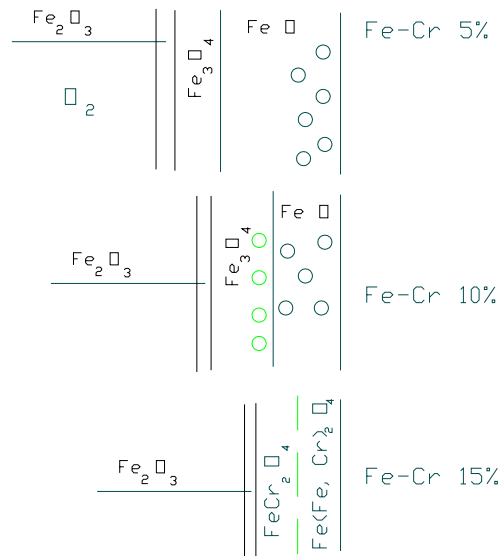
Figure 28. Oxide layers structure as a function of Cr content. [62, 63]

4.3.1 Damage mechanics for passive layer

Factors which can contribute to break-down of the oxide layer on the metal surface are: environment, structure of passive layer, existence of aggressive ions, structure of the base metal etc. In some cases only one factor can dominate but the damage process usually consists of several mechanisms working simultaneously. For example in SCC (stress corrosion cracking), stress together with the environment can lead to the damage of the passive film. Three different damage mechanisms (penetration, breaking and adsorption) leading to the destruction of the oxide film are introduced in the next three chapters. [64, 65, 66]

4.3.2 Penetration mechanism

According to Oudar et. al. [65], anions can penetrate through the oxide layer and react at the metal surface as shown in Figure 29. Furthermore, anion movement can be explained by the high fault density of an oxide layer and the electric field ($E_{1,2}$ $E_{3,4}$) which is generated through the layer as shown in Figure 29. Macdonald et. al. [67] and Kinnunen et.al. [68] have presented models for the formation and damage of the passive layer on the metal surface. This model is based on vacancies and their movement through the layer. The idea for this model is that cation vacancies can move from the oxide-electrolyte interface to the metal-oxide interface by migration and at the same time same an equal amount of cations can move in the opposite direction to the metal-oxide interface. If vacancies can penetrate inside the metal slower than through the oxide layer at the metal-oxide interface this leads to the generation of local concentrations on the metal surface. These local concentrations of vacancies can generate local stress fields inside the oxide layer and therefore cause break down. [67, 68]
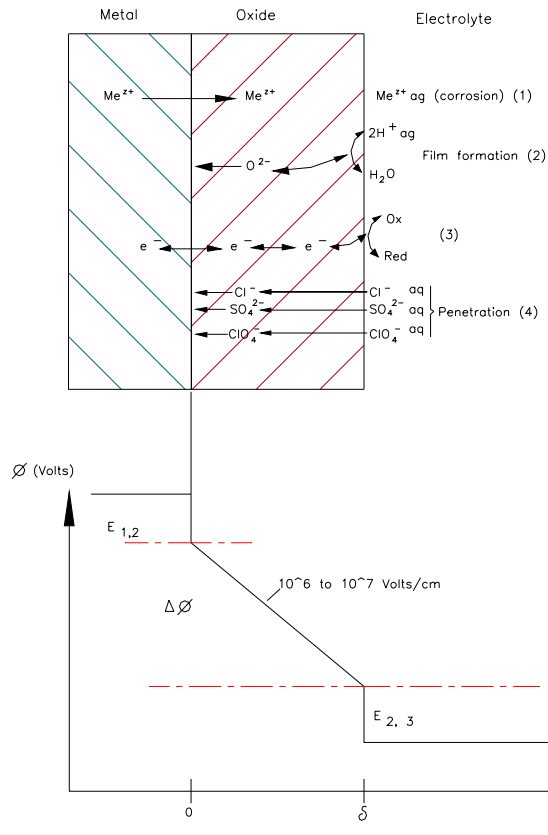
Figure 29. The penetration mechanism for oxide film damage process. [65]

4.3.3 Breaking mechanism

The oxide layer can break down when the electric field in the layer changes suddenly, generating stress fields inside the oxide layer. Also chemical reactions in the oxide layer or current peaks can damage it. For example, investigations with rotating ring electrode have shown that fast potential drop from 1.3 V to 0.7 V leads to a dissolution of Fe^{2+} ions in the electrolyte during a few milliseconds and thus causes a current peak on the electrode. This current peak has been explained to be the reason for the oxide layer damage process and can also affect strongly the self reparation process of the oxide layer. A small crack in the oxide layer can lead to direct contact between metal and electrolyte and for example in

the case of Fe may dissolve Fe^{2+} ions. The self reparation process of the oxide layer is the reason for temporal formation of Fe^{2+} ions during a few milliseconds.

These potential changes can generate a lot of small faults (nanometer size) when temporally released Fe^{2+} ions from the metal surface can occur and thus the re-passivation process on the metal surface can take place through the self repair process of the oxide layer. Aggressive ions can prevent the self reparation process as shown in Figure 30 causing pitting corrosion. [64, 65, 66]
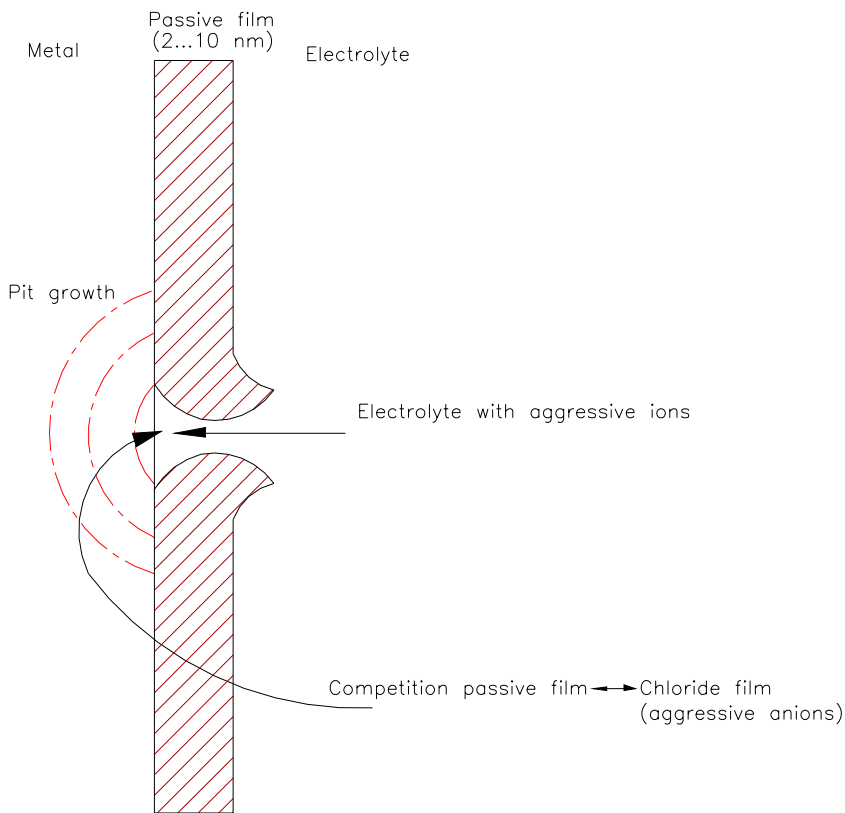
Figure 30. The oxide layer breaking mechanisms with aggressive ions. [65]

It is well known that the presence of Cl^- ions increases the pitting corrosion rate on metals. It is not completely clear what the damage mechanism is in the presence of aggressive ions. For example, the presence of Cl^- ions can break the passive layer and prevent re-passivation layer on the metal surface but the mechanism for this kind of process is unknown.

Heusler and Fisher [39] have investigated the role of Cl⁻ ions in pitting corrosion. They used a ring electrode for iron and iron alloy (Fe-6%Cr) in buffer solution. First they generated Fe^{2+} and Fe^{3+} ions and then added Cl⁻ ions to the solution. According to their tests Cl⁻ ions caused dissolution of the oxide film without corrosion current generation, i.e., Cl⁻ ions can absorb on the surface of the oxide layer and thus prevent the re oxidation process on the metal surface. Furthermore, they noticed that Cl⁻ ions can affect the thickness of the oxide layer.

4.3.4 Adsorption mechanism

According to Kolotyrkin and Hoar [65], adsorption mechanism consists of two main stages. In the first stage, aggressive ions can adsorb on the surface of the oxide layer and cations can move from the oxide to the electrolyte easier with help of aggressive ions. The basic principle of the adsorption mechanism for the annihilation of an oxide layer is shown in Figure 31.

$$\frac{d\delta}{dt} = \frac{Vm}{zF}(i_i - i_c)$$
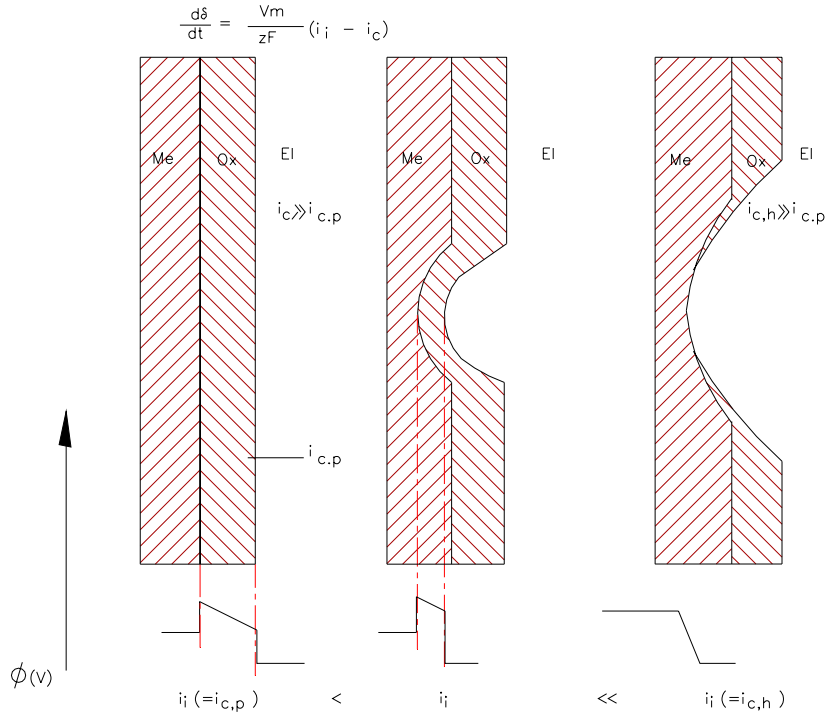
Figure 31. Adsorption mechanism for oxide damaging process.[65]

As shown in Figure 31, the adsorption mechanism consists of the movement of aggressive ions and their combination with anions at the surface of the oxide layer. This combination increases corrosion current density (i_c) with an increasing electric field (Φ) in the oxide layer and the thickness of oxide layer decreases. In the non destructed form the oxide film can sustain a high electric field (see figure 31 a). When the destruction of the oxide films begins the movement of the current carriers through the oxide film increases and the corrosion current, in the pit i_i, increases. Finally, the whole oxide layer vanishes and the electric field through the oxide film collapses (see Figure 31c). Correspondingly, the corrosion current, i_i, increases further.

Picker et. al. have given the following explanation for the damage of the oxide layer. The local damage of the oxide layer can be caused by the surface roughness of the oxide layer. This is because the electric field is not distributed evenly through out the oxide layer, i.e., it can be higher for convex areas and

thus higher electrostatic pressure can affect the oxide layer. The oxide layer damage process starts when the electrostatic pressure is higher than the bearing strength of the oxide layer. Furthermore, with an increasing electric field the mobility of vacancies can increase through the convex area. [64, 65]

4.4 Research needs in the EAC

In order to verify materials properties needed in structural analysis as well as in development of material damage models new in situ tools are necessary. In the following a set of applications are described, based on the new pneumatic servo-controlled material testing arrangement, which allow in situ monitoring of the properties of passive films forming on structural materials, monitoring of crack growth rate as a function of hydrodynamic and water chemistry variables as well as irradiation and measurement of the effect of environmental variables on fatigue life of structural materials.

5. Development of a pneumatic servo-controlled material testing system

As described above, design parameters in material selection include many important factors. The field of materials and their properties is very wide, and aspects such as environmentally assisted cracking EAC, fatigue, corrosion and irradiation areas need to be considered. It is important to consider the requirements for these specific when material testing systems are being developed. The basic requirements for systems developed in this thesis can be listed as follows:

- *Environment*; capable of working in PWR and BWR coolants (temperature up to 350 °C and pressure of 16 MPa) and inside reactor core.
- *Load and displacement accuracy*; capable to perform accurate stress and strain singularities for crack tip of specimens
- *Pneumatic loading unit* i.e. gas pressurized metal bellows for the test load.
- *Pressure adjusting loop with electronic control system*; capable of working with feed back control under high pressure and temperature levels.
- *Two way load*; capable to generate cyclic loading of the specimens (fatigue)
- *Electric isolation*; needed for electrochemical measurements and for crack growth rate measurements i.e. for DCPD (Direct Current Potential Drop system).
- *Accurate a*l*ignment of the specimen*; for the specimen fixing system
- *Moveable testing system*; capable of working in the autoclave and in the reactor core environments with long gas lines.
- *Calibration system for load calculations,* by using metal bellows inside pressure with effective cross section.
- *Load frames,* for different applications i.e. fracture mechanics, fatigue, electrochemical measurements and incore tests.
- *Small size, for* minimum thermal expansion for the load frame.

In conventional materials testing systems the load on the specimen is produced by using a pull rod. This pull rod penetrates the pressure boundary through a sealing element, which causes a additional friction force. It was decided, that the

operation principle of the material testing system should be pneumatic instead of hydraulic so the load control would be more accurate than with conventional servo-hydraulic devices. Such a system enables testing of small size samples, which is a significant advantage when testing e.g. irradiated materials. Furthermore, the new design enables simultaneous testing of several samples, which helps produce statistically more reliable data and more economically way. The pneumatic servo-controlled pressure adjusting loop was designed keeping mind the requirements presented above. The aim was to develop a high pressure adjusting system capable of working at a 10–20 MPa pressure range. The pressure controlling system was designed by using servo valve and feedback signal technology.

As described above, strain and stress conditions at the crack tip can strongly affect the level of fracture mechanics parameters such as K, CTOD and J. Material testing systems typically consist of a loading system, a high pressure water circulation system, autoclave (pressure vessel), sensors and data collection system as shown in Figure 32. The water chemistry of the testing system is controlled, i.e., pH, conductivity and oxygen level can be controlled and measured during the test. Test load is typically generated by using hydraulic, pneumatic or electric step motor systems which are capable of working under a feed back control and with PID values as described in the next chapter.

A typically used test environment at VTT is a simulated BWR environment: temperature 273°C and outlet oxygen content 300 ppb. The outlet flow is purified with ion exchangers before re-circulating the water. The re-circulation flow volume through the autoclave is typically 0.3 l/min, which means that the autoclave water is refreshed every 20 min. The water chemistry parameters for the outlet water and inlet water (pH, conductivity and dissolved oxygen content) are continuously measured at ambient temperature. [69]
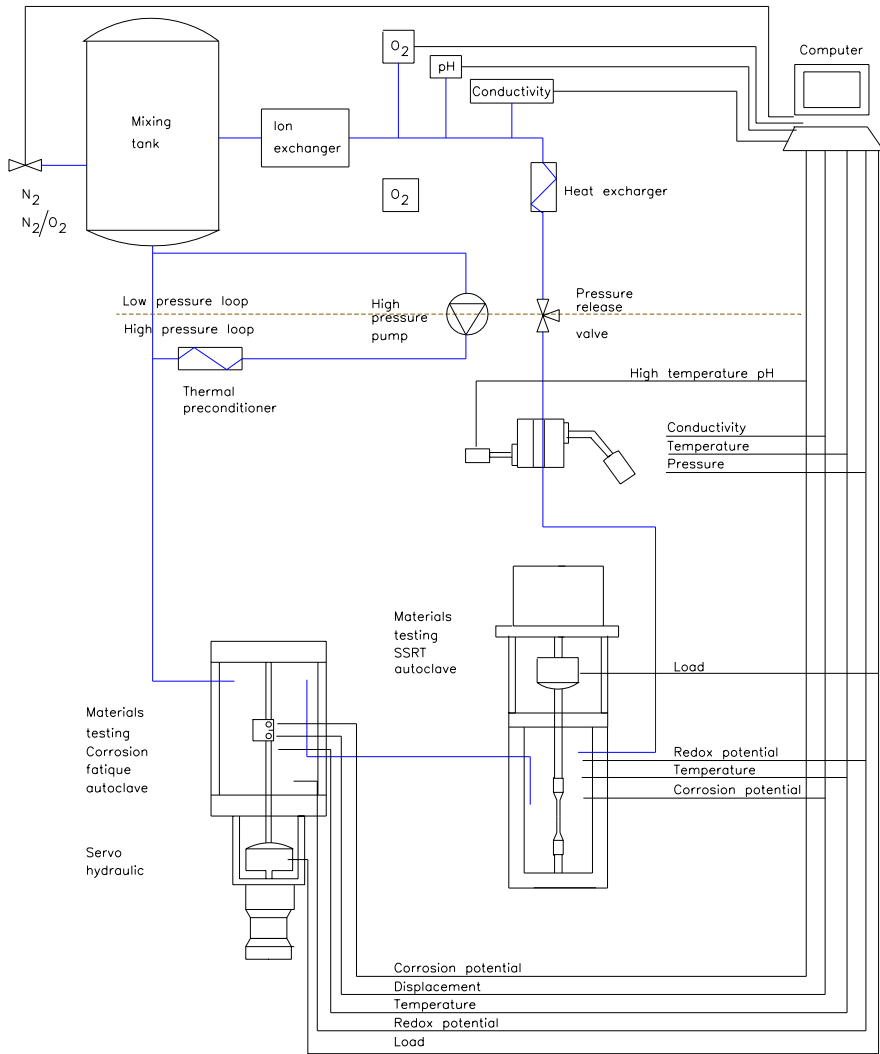
Figure 32. Main components of EAC material testing system. [69]

The automatic controlling and adjusting loop based on feed back control (according to standard SFS 2289) is presented in Figure 33. The system consists of circulation loops (A) and (B). (B) is a controlled system and (A) is a controlling system. Furthermore the controlling system (A) usually consist of a reference element c, a feed forward device FF, a direct adjustable system D, an indirect adjustable system ED, a transducer T and a filter S. The controlled

system (A) includes devices which are controlled during the adjusting operation. [70]

Figure 33. The controlled system with feed-back signal. [70, 72]

The controlling parameters used in the feed-back loop presented above are described by letters w, e, m, y, f and v. The reference variable w and the feed-back signal f are connected through the comparing element c. According to the reference variable w and the and feed-back signals, the reference element can produce an error signal e that is usually connected to the feed forward device (FF).
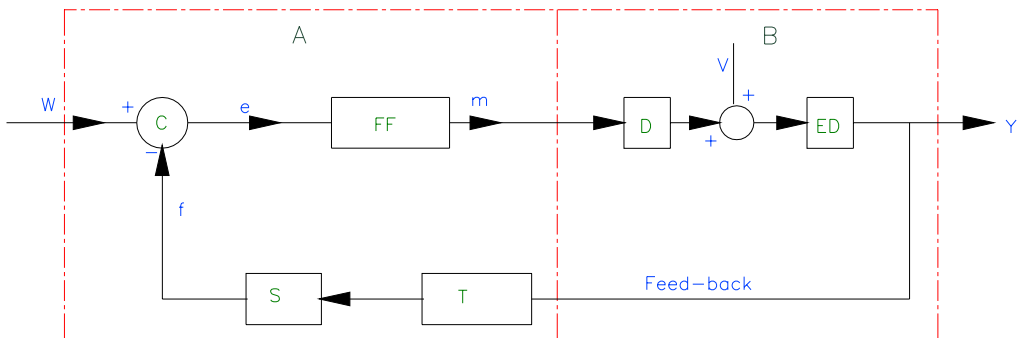
The feed forward device consists of an amplifier and an adjuster, which are in series. From the feed forward device (FF) the manipulated variable is connected through the controlled system (A) and on to the direct (D) and indirect controlled (ED) systems. From the indirect controlled system (ED) the signal is led to the feed-back and indirect controlled variable (y). Usually, positive feed-back circulation loop consists of a transducer and a filter system before the comparing element c. Furthermore, there can also be interference v inside the controlling loop (A). [70, 72]

Typically, the automatic controlling and adjusting loop is equipped with a PID adjuster. The basic PID adjuster collects information from the comparing element (set point - measured point) including present, past and future information. The term (I) is the integrator which is used to collect the past information from comparing element. The amplifier term (P) is used to estimate information from comparing element in present time. The derivation term (D)

can not exactly forecast the information from future but it follows the course of the diversion. [70]

5.1 The operation principles of the pneumatic pressure adjusting loop (PSC)

The main parts of the pneumatically powered adjusting loop are described in Figure 34. The pressure adjusting loop consists of four pressure boundaries (A), (B),(C) and (D) as shown in Figure 34. At pressure boundary (A), the gas flow needed for the servo valve (6) is provided by the high pressure compressor (1). An operational pressure level (20 MPa) of the gas is achieved with the fully automatic compressor. The pressure variation at the pressure boundary (A) during the test is 17.5 to 20 MPa.

From the pressure accumulator (2) the gas is led to the pressure reducer (3) and further through the manual flow valve (4) using 6 mm diameter pipes. The boundary pressure (B) depends on the test environment and specimen size. For example, if the specimen size is 10x10x55 mm^3 and the test environment pressure is 8 MPa (pressure vessel, boundary (D), then the pressure at the boundary (B) could be 15 MPa. This pressure can be adjusted by the pressure reducer (3). In such a case, the maximum pressure difference which can directed to the bellows is approximately 5,5 MPa. So, the real working pressure of the bellows during the test can vary from 8 to 13,5 MPa. According to the servo manufacturer, the maximum pressure for the servo valves is 20 MPa. [71]

From the flow valve (4) the gas is directed to the bellows (5) and to the servo valve (6) (pressure boundary (C)) by 3,0 mm diameter pipes. The gas flow from the servo valve is let out from the pressure boundary (C). The suitable initial pressure level required for different tests can be provided (pressure boundary (C)) with the pressure regulator (3) and the flow valve (4). In the case of specimen size 10x10x55 mm^3 and test environment pressure 8 MPa, the initial pressure at boundary (C) could be adjusted to 0.7 MPa before start of the test. The initial gas flow through the servo valve is then about 6–8 l/min. [71]

The adjustment of the bellows pressure (5) (and the pressure at boundary C) is based on a continuous gas flow through the flowing valve (4) and the servo

valve (6). Only one servo valve (6) or electrically controlled closing valve and one mechanical flowing valve (4) are needed to provide the adjustable pressure for the pressure boundary C. With this kind of pressure boundary loop, a two-way pressure adjusting system can be created. The servo valve (6) can be opened or throttled for adjustment of gas flow until the desired pressure level of the bellows (5) is achieved. Throttling will increase and opening will decrease the bellows pressure. The load directed to the specimen is directly proportional to the bellows (5) pressure (pressure boundary (C)). The displacement of the bellows is controlled by an LVDT-sensor (7) which gives a feedback signal to the servo controller. The servo controller compares the feedback signal of the LVDT-sensor to a pre-set base signal. If there is a difference between the two signals, the servo valve can throttle or open for adjustment of gas flow until the feedback and the preset base signals become equal as has been described above.[71]

The pressure accuracy and stability of pneumatic servo-controlled pressure adjusting loop was checked with demonstration test. During this test the servo-controlled pressure adjusting loop is worked under pressure feedback control. The test result is shown in Figure 35. The deviation of the pressure was ± 0.02 MPa under 9.8 MPa pressure. Furthermore, the pneumatic servo-controlled pressure adjusting loop is tested by using different high pressure levels as shown in Figure 36. According to Figure 36, the maximum pressure level which can be created with pneumatic servo-controlled pressure loop was around 20 MPa. Commercial pneumatic servo valves are designed for pressure level of 1 MPa usually. [71]
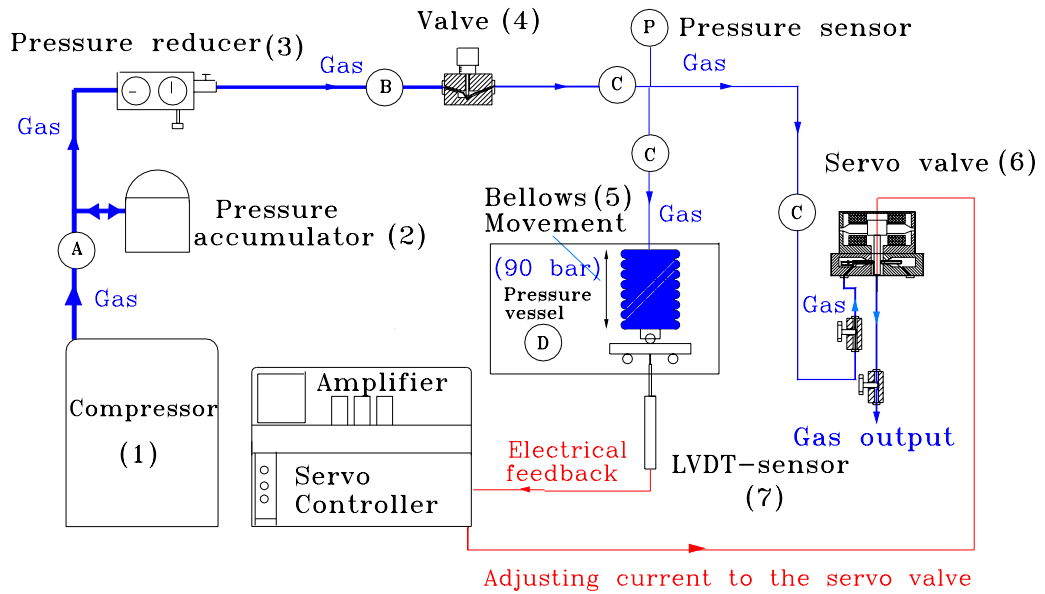
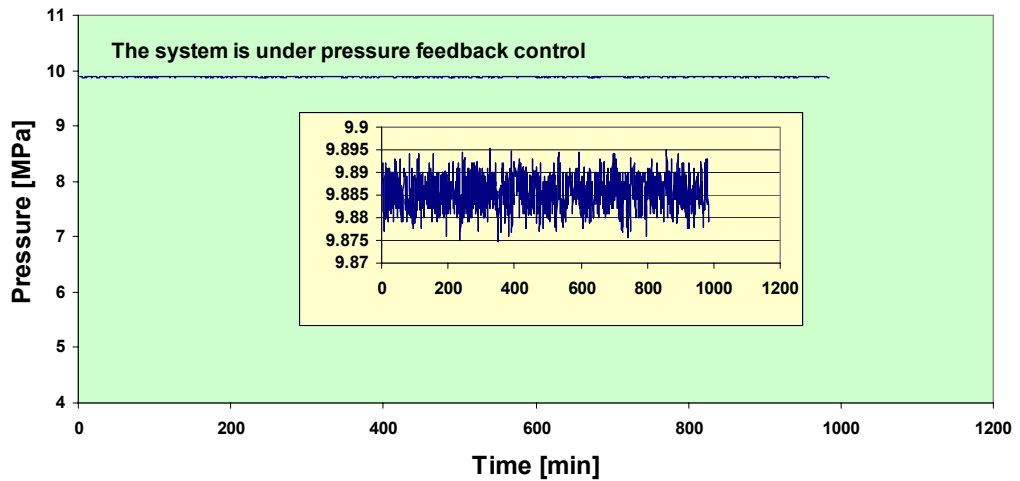*Figure 34. Operating principle of the pressure adjusting loop.[71]*

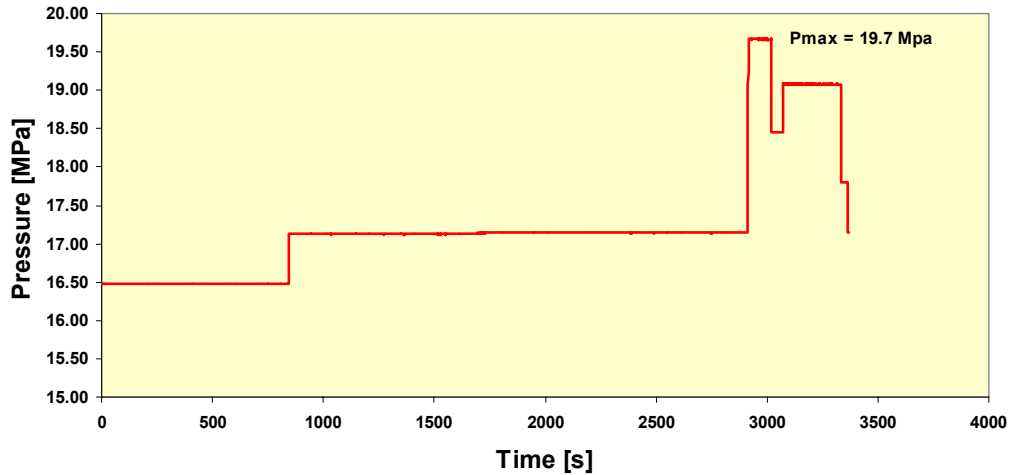*Figure 35. The accuracy of pressure under pressure feedback control.*

Figure 36. The high pressure level test for the PSC loop.

5.2 Pneumatic loading unit with metal bellows

The same pneumatic servo-controlled pressure adjusting system described above can be connected to every application of the pneumatic material testing systems, i.e., for pneumatically powered PSCFM-, PSCCDE-, PSCFAT- and PSCINCORE devices.

The main principle of the pneumatically powered loading unit is to provide the needed test load by using gas pressurized metal bellows. The gas is led inside the bellows from the servo-controlled pressure adjusting loop, and together with inside pressure and the effective cross section of the bellows the load can be calculated. The design and structure of the pneumatic loading unit is based on the bellows main dimensions as shown in Table 1. The main parts of the pneumatic loading unit are shown in Figure 37. The pneumatic loading unit consists of a corrugated bellows, upper and lower pistons, gas inlet tube, sleeve and zirconium oxide roll. The upper and lower pistons are moved over the sleeve when the pneumatic loading unit is pressurized. The three main diameters of the pneumatic loading unit are the outer diameter d_u, inner diameter d_i, and the effective diameter d_e. The load is calculated using the effective diameter d_e.

77

Table 1. Main dimension specification of the three different bellows units in use at VTT. [73]

Bellows specification	10x10x55 mm^3 3PB specimen testing	3x4x27 mm^3 three point bending (3PB) speci-men testing and CER testing system and tensile testing system	fatigue specimen testing
Internal diameter	23.5 mm	12.5 mm	29.0 mm
External diameter	36.5 mm	19.0 mm	44.0 mm
Elastic deformation per corrugation (axial)	+/- 0.3 mm/corr	+/- 0.15 mm/corr	+/- 0.3 mm/corr
Spring rate per corrugation	850 N/mm/corr	813 N/mm/corr	3030 N/mm/corr
Effective bellows cross section	690 mm^2	189 mm^2	990 mm^2
Number of corrugations	9	7	4
Axial movement for whole bellows	+/- 2.7 mm	+/- 1.05 mm	+/- 1.20 mm
Maximum pressure	14 MPa	15 MPa	27 MPa
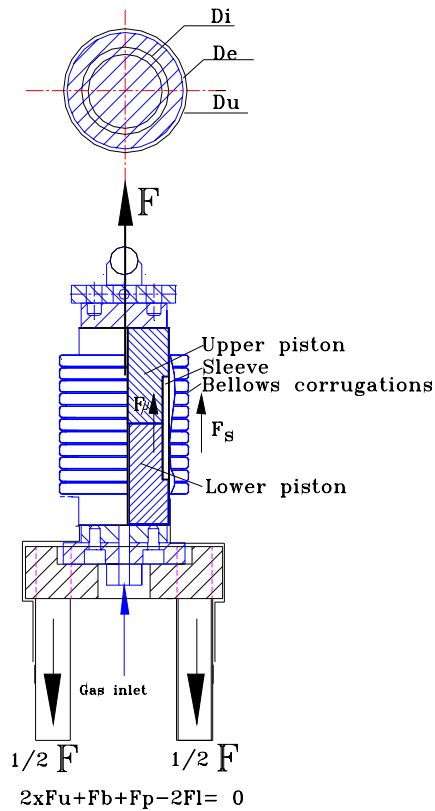
Figure 37. The pneumatic loading unit with the internal parts and the metal bellows.

5.3 Calibration of the pneumatic loading unit used in fracture mechanics, fatigue, and CDE measurements

Commercial load sensors are typically designed for low temperature gas environments and they cannot be installed for the high temperature water environments. The load determination of the pneumatic loading unit is based on special developed calibration methods where the metal bellows' own stiffness and effective cross section are determined for the true load calculations. High temperature calibration of the pneumatic loading unit was performed in a gas environment in the furnace shown in Figure 38.

The calibrations of the pneumatic loading unit have to be performed at real test temperatures. The LVDT-, pressure and load sensors used in the calibration furnace of the pneumatic loading unit have been calibrated according to VTT calibration certificates before the furnace calibration tests. The same moving parts of the load frame including pneumatic loading unit are needed in the calibration furnace as well as in a real test. The bellows, Figure 38 (a), was first equipped with additional posts, Figure 38 (b), and then installed in the calibration furnace, Figure 38 (c). The calibration furnace consists of the main frame, heating elements, an LVDT-sensor and a load sensor. A typical set of raw data from a load-pressure calibration run is shown in Figure 39. An accurate calibration based on this result can be achieved between the gas pressure and the load directed to the specimen by the bellows loading unit. The calibration procedure consists of two different tests. In the first calibration test, the pressure loss arising from the metal bellows own stiffness and internal parts, the friction fall of the pneumatic loading unit can be determined over the working range (see Figure 39.). In the second calibration test, the interaction of pressure and load was determined by performing constant displacement rate tests with demonstration specimens (see Figure 38, Figure 41). Selection of the demonstration specimen depends on the working range of the real test specimens to be used.
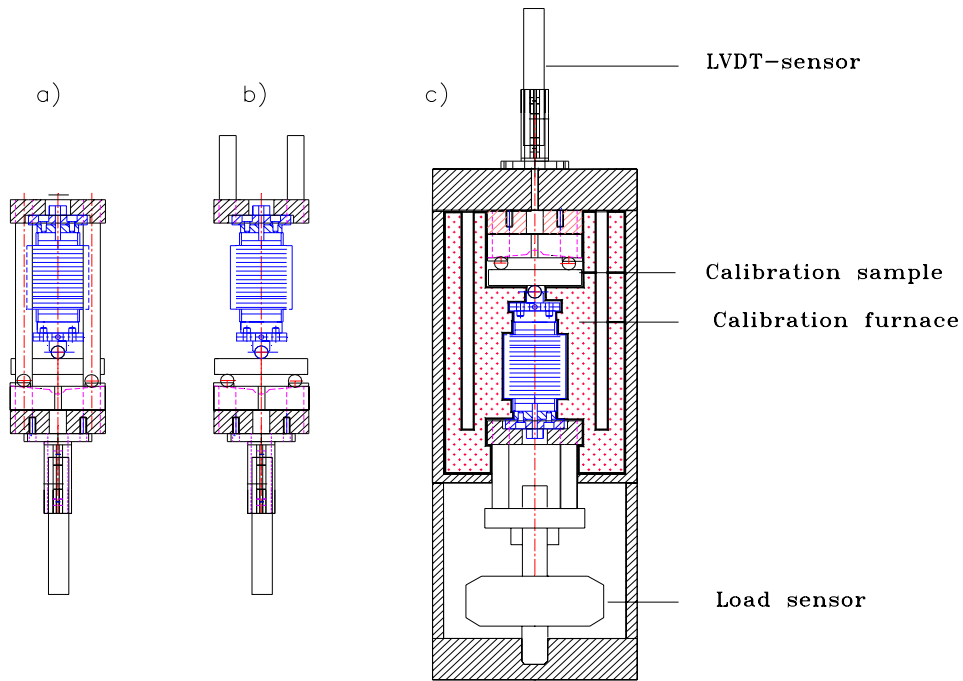
Figure 38. High temperature calibration system of the pneumatic loading unit.

The test result from the first calibration test during two different calibrations is shown in Figure 40. The pressure loss curve for of the pneumatic loading unit is shown as a function of displacement at 200 °C. This data is needed for real load calculations presented later. According to Figure 40, the pressure loss due to the metal bellows own stiffness and internal parts friction fall of the pneumatic loading unit can be determined by using the following formula:

$$p_h = 0{,}3299 * \Delta + 0{,}0211 \tag{44}$$

where, p_h = pressure loss arising from the metal bellows own stiffness and internal parts friction fall of the pneumatic loading unit (see Figure 37) [bar]/mm, Δ = displacement [mm]. The value for the constant (0,3299) comes from the pressure sensor at the start of the test (initial gas flow through the servo valve) and the value for second constant (0,0211) comes from the trend line curve for pressure as a function of displacement as shown in Figure 40. The pressure loss, p_h can be determined for the total working range of the pneumatic loading unit according to formula (44).
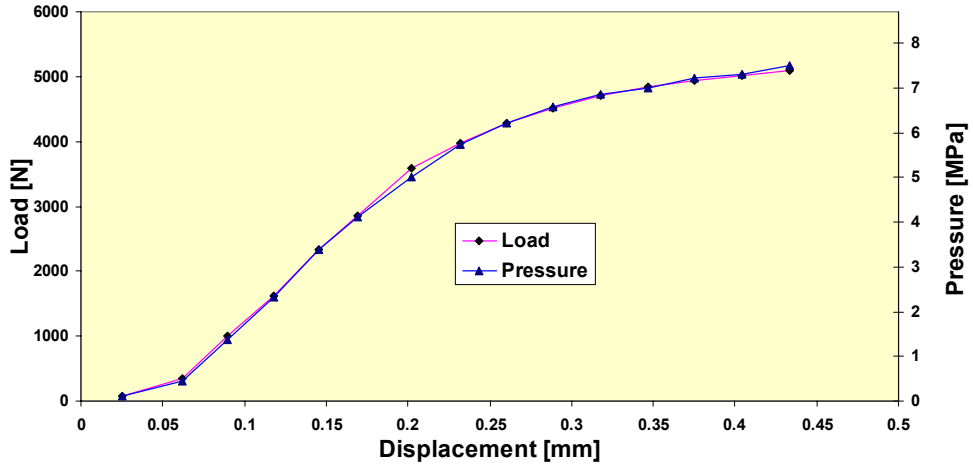
Figure 39. The load and the pressure of the pneumatic loading unit as a function of displacement.

The results of the second calibration test are shown in Figure 39. The load is measured by the load sensor, see Figure 38, and the inside pressure of the pneumatic loading unit is measured by pressure sensors. The basic shape of these curves is similar as a function of displacement, and by using these curves and the pressure loss curve (Figure 40), the effective cross section for metal bellows can be calculated.

Figure 40. The bellows stiffness together with friction fall of the pneumatic loading unit calibrations at temperature of 200 °C.

Determination of the effective cross section for the metal bellows is based on information from the data shown Figure 39 and in Figure 40, and can be calculated as,

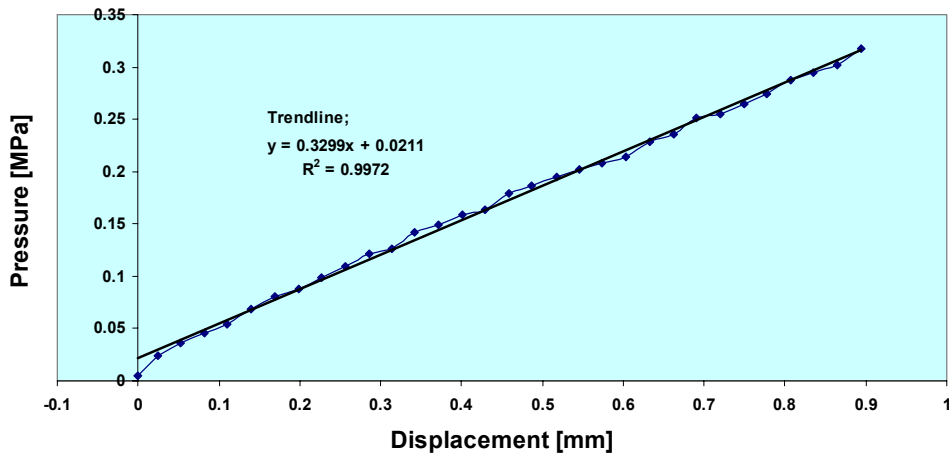$$(p - p_h)A_{eff} \, F_L \Rightarrow A_{eff} = \frac{F_L}{(p - p_h)} \qquad (45)$$

where, F_L = load [N], measured by using load sensor as a function of displacement.

p = pressure [MPa], measured by using pressure sensor as a function of displacement.

p_h = pressure loss [MPa] according to Figure 40.

The determined effective cross section at each measuring point can therefore be calculated from the calibration curves and it should be constant over the working range of the metal bellows. After determination of the effective cross section, all needed parameters are available and the generated test load can be calculated from bellows inside pressure as,

$$F_c = (p - p_h)A_{eff} \qquad (46)$$

where F_C = load [N] calculated from inside pressure of the pneumatic loading unit
        p = pressure [MPa] inside pressure of the pneumatic loading unit
        p_h = pressure loss according to Figure 40 result [MPa]
        A_{eff} = bellows effective cross section [m^2]

In Figure 41, the correlation between calculated pressure based load and the true load measured by using the load cell are shown. The calculated load was extracted from each measured calibration point using formulas 44 and 46. For example the pneumatic loading unit introduced force is calculated from pressure as follows;

$F_c = (6.202 - 0.083 * 10 * 10^5) \, \text{N/m}^2 * 696 * 10^{-6} \, \text{m}^2 = 4258.7 \, \text{N}.$

where p = 6.202 MPa (from pressure sensor at point 0.26 mm of displacement)

p_h = 0.083 MPa (according to Figure 40 i.e. 0.26 mm*0.32 MPa/mm)

A_{eff} = 696 mm^2 (according to formula (45))

Furthermore, the load loss due to the metal bellows own stiffness can according to the metal bellows manufacturer (spring constant) be presented by equation (47) [68];

$$F_s = \frac{c_\delta \, \delta_b}{n_w} \qquad (47)$$

F_s = the load loss according to metal bellows own stiffness

c_δ = axial spring rate for the bellows [N/mm]

δ_b = required axial movement for the whole bellows [mm]

n_w = number of corrugations

This formula (47) is not needed for the load calculations when the pressure loss of the pneumatic loading unit is determined experimentally as described above.

The real load measured by the load sensor as described above was 4267 N and the calculated load was 4259 N. The deviation of the calculated load compared to the load indicated by the load cell was 0.35 % at displacement point 0.26 mm for the pneumatic loading unit.
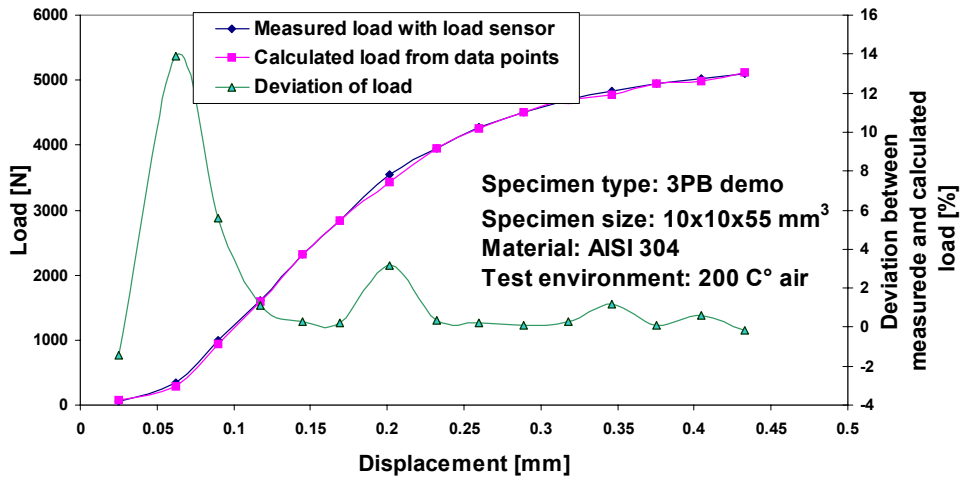
Figure 41. The load and pressure of the pneumatic loading unit as a function of displacement.

The accuracy of the load and pressure calibration over the tested range (0.1 to 0.45 mm of displacement) was approximately ±1 %. According to this data, the biggest deviation of the calculated load was at the beginning of the calibration curve. The main reason for this deviation is mostly mathematical but also caused by compliance in the beginning of the calibration. The compliance of the calibration furnace and free clearance of the rolls slightly affects the calibration results. In any case, the calibration accuracy is dominated by the accuracy of the pneumatic sensor, which in this case is ±0.2 % from 20 MPa.

5.4 Summary and discussion of the developed calibration methods

The main parts of calibration procedure are as described in the following:

The effective cross section of the bellows must be checked and verified at each calibration point with help of the measured pressure and the true load measured with a load cell. The effective cross section of the bellows must be constant at each point over the whole working range. The bellows' stiffness and friction loss

must be subtracted from the measured pressure at each calibration point as shown in the example above.

According to bellows' the manufacturer the effective cross section of the bellows is 690 mm^2, as shown in Table 1. The cross section evaluated by calibration is 696 mm^2. These values are very similar.

The measured bellows stiffness is 224 N/mm. According to the bellows' manufacturer, the bellows stiffness should have been 95 N/mm. Measured values were rechecked for the bellows stiffness by using a hydraulic testing system. This measurement gave a stiffness of 165 N/mm without pneumatic loading unit internal parts, and 219 N/mm including pneumatic loading unit internal parts, therfore validating the first measurement (224 N/mm). The difference between measured and given stiffness of the bellows was sizeable. One reason for the difference might lie in the bellows welding procedure. The inside friction fall contribution in the pneumatic loading unit is estimated to be the difference between the measurements with and without internal parts, i.e. 54 N/mm.

6. Applications of the pneumatic material testing system

6.1 The servo-controlled fracture resistance measuring device, PSCFM-device

In recent years, fracture mechanical testing has increasingly been used for research of environmentally assisted cracking, EAC. The PSCFM-device is designed for testing sub size three point bending specimens under different high temperatures and pressures. Specimen type have selected using requirements for constraint as shown in chapters 2.1.3 and 2.6.

The PSCFM device consists of a pressure adjusting loop (which is introduced above in chapter 5.1) a load frame with pneumatic loading unit. The specimen sizes used are 10x10x55 and 3x4x27 mm^3. A load frame with a moveable specimen carrier, see Figure 42, was designed especially to enable multi-specimen testing and to achieve a minimum compliance of the load frame. This specimen carrier is easy to handle and it facilitates the positioning of the specimens and attaching the PD leads at the beginning of the test. The PD system is used for monitoring the crack growth rate of the bending specimen during the test. The load frame consists of the following parts: moveable cassette system, aluminium oxide rolls, pneumatic bellows, carrier for the LVDT sensor, top and bottom parts of the load frame and four posts. The bottom part of the load frame can move along the four posts so that the system can be adjusted for different size three point bending specimens.
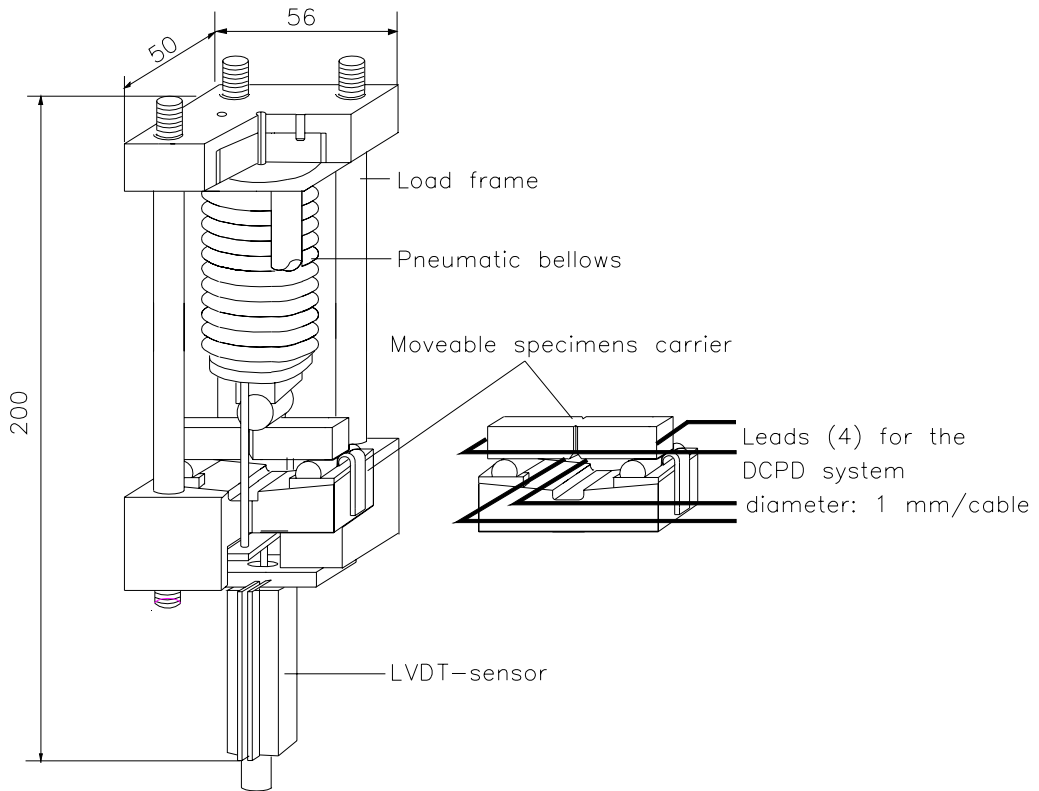
Figure 42. The load frame with the cassette system and the pneumatic loading unit.

Constant load constant displacement and constant displacement rate (rising load) tests can be performed with the PSCFM device at high temperature air and water environments by using small size three point bending specimens. Because of small size of the load frame it is possible to equip the autoclave with several test devices at the same time.

6.2 The pneumatically powered controlled distance electrode arrangements, PSCCDE device

The principle of the thin layer electrode arrangement, developed to perform electrochemical measurements in low-conductivity media, is shown in Figure 43.

In this arrangement, the working electrode and the inert counter electrode (usually made of Iridium) formed as two parallel surfaces (tips of small diameter rods). The distance between the electrodes can be adjusted up to about 100 µm with an accuracy of 10^{-6} mm by means of a step motor and spring system developed originally for CER measurements [74]. It is possible to replace the step motor with a servo-pneumatically driven bellows system in which no moving parts penetrate through the pressure boundary. The reference electrode is situated at the side of the working electrode. When the working electrode is polarized, the current flows between the working and counter electrodes across the µm-range gap, while the potential is measured from the side of the specimen thus greatly suppressing the effect of the ohmic drop in the electrolyte. [74]
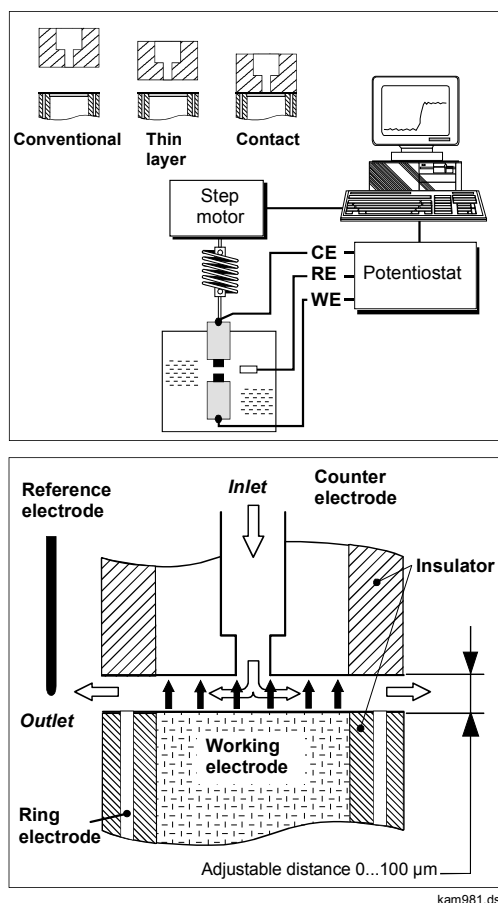

Figure 43. A scheme of the experimental set-up for the thin-layer electrochemical measurements.[74]

The bulk solution can be pumped through the counter electrode ensuring that representative solution chemistry prevails between the electrodes during the measurements. Therefore, this test arrangement can also be conveniently used to study the effects of solution flow rate and novel water chemistries on the electrochemical properties of oxide films. A detector electrode, analogous to the ring electrode in a conventional rotating ring-disk electrode set-up, can also be included in the arrangement to identify soluble species released during corrosion. [74]

The arrangement shown in Figure 43 can be employed to obtain electronic and electrochemical information of the oxide films on the studied construction materials by using the following techniques:

Thin layer electrochemical measurements

* Thin Layer Electrochemical Impedance (TLEI) measurements to characterize the oxidation and reduction kinetics and mechanisms of metals as well as properties of metal oxide films even in low conductivity aqueous environments.

* Thin Layer Walljet (TLW) measurements to detect soluble products released from the working electrode.

* Other controlled potential and controlled current measurements

Solid contact measurements

* Contact Electric Resistance (CER) technique to investigate and/or to monitor the electronic properties of surface films

* Contact Electric Impedance (CEI) measurements to measure the solid contact impedance spectra of oxide films.

The main parts of the pneumatically powered CDE measuring device are presented in Figure 44. The pneumatic CDE system consists of pneumatically powered bellows, springs, moving tips, pressure pipe and the servo-controlled pressure adjusting loop. The servo-controlled pressure adjusting loop is the same

as in the pneumatic servo-controlled pressure adjusting loop presented in Figure 34. The pneumatic CDE-device was designed to work under pressure feedback control rather than displacement feedback control.
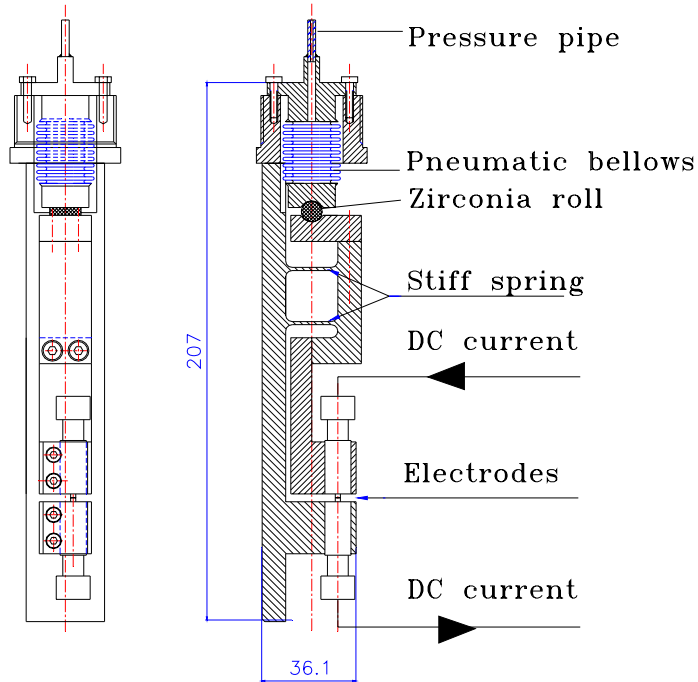

Figure 44. The pneumatically powered PSCCDE-device.

6.3 The servo controlled fatigue-device, PSCFAT-device

The primary goal of this test unit was to design and test pneumatically powered fatigue-device in BWR and PWR environments. A key requirement of the design was that it would allow four fatigue-devices to be simultaneously used in an autoclave loop or at the plant. Furthermore, an important requirement was to check how precisely the device would operate and how precisely alignment class of specimen would be under strain feedback control. The schematic picture of the load frame for fatigue test is shown in Figure 45. The fatigue load frame consist of pneumatic loading unit, bottom and top caps, metal slide alignment system for specimen and strain measuring posts for LVDT-sensor. The body of the fatigue unit is essentially a thick walled tube providing good symmetric

stiffness and thus helping to maintain alignment. The upper end of the specimen is threaded into the pneumatic loading unit and provides tensile load when the bellows pressure is less than the environment pressure. Compressive loading is the result of bellows pressure exceeding the environment pressure. [75]
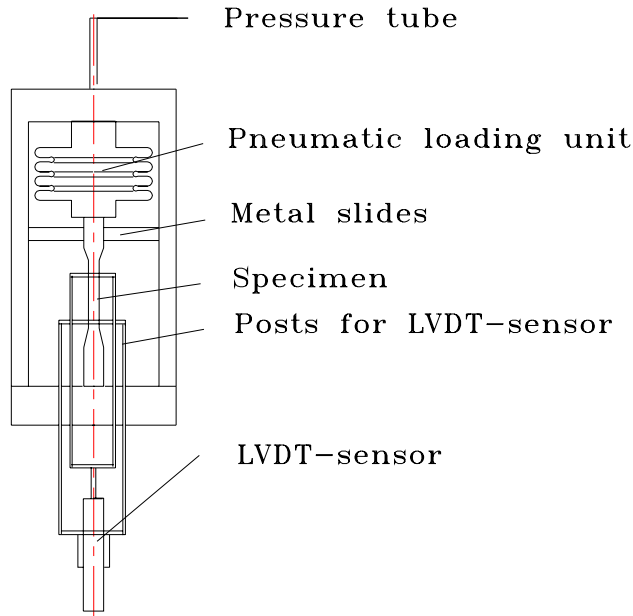

Figure 45. PSCFAT-device with main parts.[75]

6.4 The incore tensile testing device, PSCINCORE

The primary goal of this work was to develop and test a prototype for a tensile testing system which is capable of performing a tensile test for small size copper and copper alloy specimens inside the actual reactor core. The key factors and requirements for the tensile testing system were the size of the load frame with the pneumatic loading unit (metal bellows) and its pipe length (should be at least 25 m pipeline), the accuracy of the displacement (strain rate) and the accuracy of the load. [76]

The reliability of unit operation and test results was to be verified. The pneumatic servo-controlled material testing system which used for CER, fracture and other types of testing in LWR autoclaves was given priority over other

loading means. The pneumatic servo-controlled pressure controlling loop was based on a patented flowing valve system with Moog digital servo technology.

Load train rigidity and concentricity should provide specimen alignment equal to that provided by conventional materials testing load frames. The thickness of the tensile specimen is only 0.3 mm so a special fixing system is needed to guard against bending of the specimen during fixing process. The strain measurement and control of the tensile specimen during the test is performed using LVDT sensor. Specimen cross section and material strength determine the required load capacity. A load range of 100 N…200 N producing a stress range of 110…250 MPa for a 0.3 mm thickness specimen should be sufficient for most tests with copper and its alloys. The system should worked under strain or displacement control. The strain rate should be between $1.7*10^{-4}…10^{-7}$ 1/s. The dimensions of the pneumatic loading unit, pipelines and the load frame should be small enough to perform tests inside the reactor. The shape, size and operating principle of the load frame is designed according to requirements set by the reactor environment. The pneumatic loading unit with servo-controlled pressure adjusting loop should be able to work with a 30 m pipeline.

It was decided that a simple prototype tensile unit would be designed and manufactured from easily machined martensite stainless steel. Figure 46 provides a sketch of the prototype tensile unit design and lists the important elements. The maximum diameter of the prototype was 38 mm. A final design suitable for use in the reactor core is functionally identical to the prototype unit but it would be constructed for smaller dimensions with a maximum diameter of 25 mm.
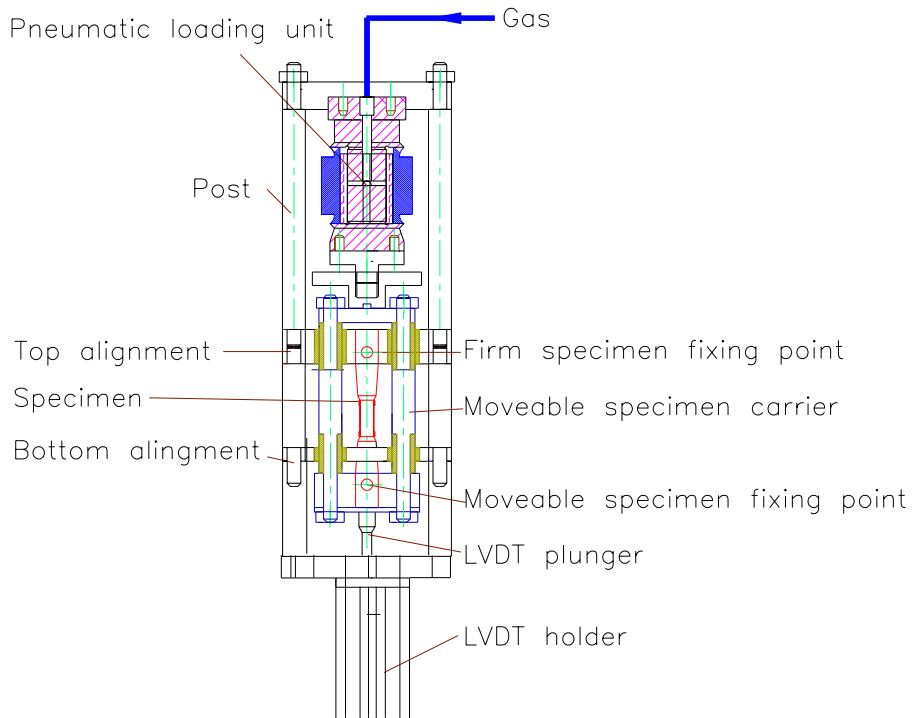
Figure 46. Schematic of the prototype axial tensile testing unit. [76]

7. Evaluation of testing units

The experimental procedure consists of four types of test, electrochemical tests with PSCCDE device, fracture mechanical tests with PSCFM device, corrosion fatigue tests with PSCFAT device and tensile tests with PSCINCORE device. The pneumatic servo-controlled pressure adjusting loop with metal bellows is connected for each applications of the material testing system.

7.1 Preliminary test results by using PSCFM-device at gaseous environment

The PSCFM device was used to determine the fracture resistance curve of sensitised AISI 304 stainless steel. The tests were performed in air at room temperature and at 288 $^{\circ}$C. The momentary crack growth during the tests was measured with the PD (Potential drop) technique (ASTM E 647 1993). The test lay-out is shown in Figure 47.
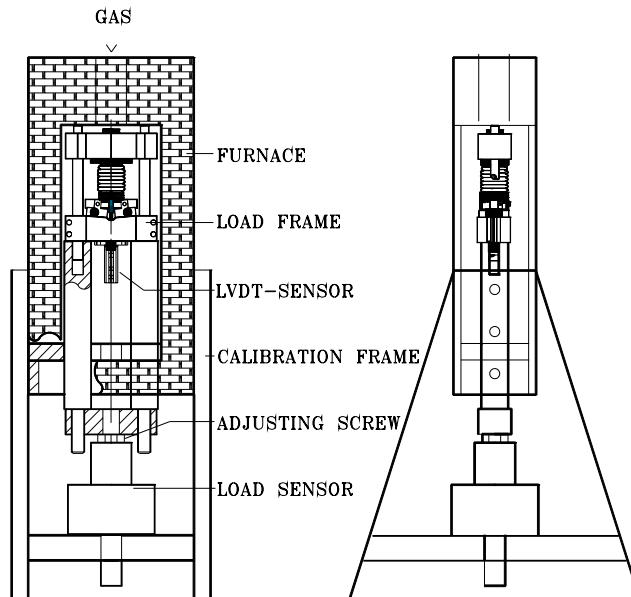

Figure 47. The test lay-out for testing in a gas environment.

95

The servo valve needs a pressure level of 0.05...0.2 MPa (initial gas flow through the servo valve) when the test is started (the pressure of the environment is normal atmospheric pressure). The pressure level at the beginning of the test depends on the size of the test specimen. Typically the pre-load is 50...300 N. In Figure 48 typical load-time and displacement-time curves are presented for AISI 304 stainless steel in air at 288 °C.

The displacement shows linear behaviour except at the beginning of the loading (time < 500 min). This non-linearity is caused by the compression of the gas in the bellows and the compliance of the load frame. The compliance of the load frame was measured with a separate calibration sample. According to the data shown in Figure 49, the non-linearity at the beginning of the test was accounted for in the final analyses.

The target displacement rate produced with the help of the function generator was $1.8*10^{-4}$ mm/min. According to the measured data (Figure 48), the actual displacement rate was $1.74*10^{-4}$ mm/min during the test. The difference between the target and actual displacement rate is caused mainly by the inaccuracy of the setting of the function generator. The difference between the measured and target displacement rates, i.e. 3.3 %, can be considered acceptable for all practical purposes. The specimen pre-load before pressurizing the bellows was about 500 N. Pre-load is generated using a manual adjusting screw (Figure 47). The pre-load is not needed when testing in a BWR-environment because of the high pressure of environment; The load can affect the specimen only when the bellows inside pressure increases to a higher level than the pressure of the autoclave (autoclave pressure is typically 8.5 MPa so initial pressure level of 0.05...0.2 MPa cannot generate load for the specimen).
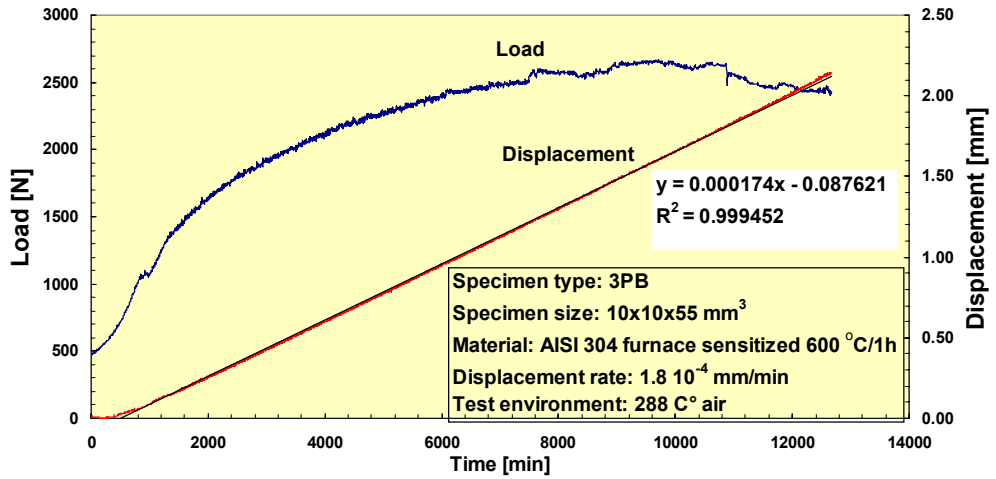
Figure 48. Test results for a single AISI 304 specimen tested in air at 288 ^{o}C.
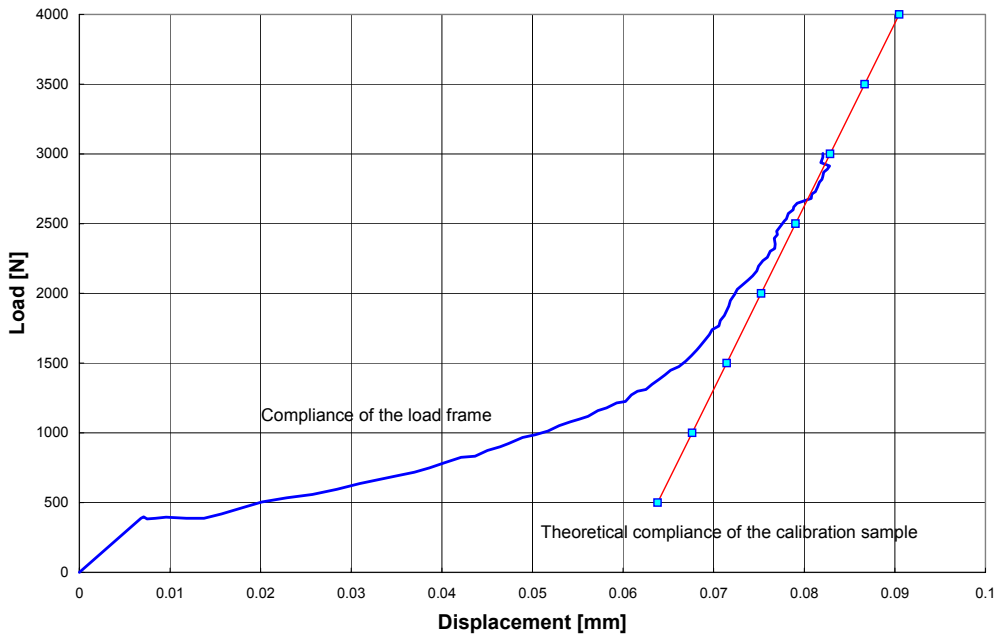

Figure 49. The compliance of the load frame with a calibration sample compared with the theoretical compliance of the calibration sample alone.

97

The developed servo-controlled fracture resistance measuring device is suitable for performing constant load and displacement rate tests for small three point bend specimens in gaseous test environments. The pre-set displacement rate was achieved accurately in the tests and it was constant during the test even with slow (0.2 10^{-5} mm/min) displacement rates. The PSCFM measuring device was used to determine the fracture resistance curve of sensitized AISI 304 stainless steel. The tests were performed in the air at room temperature and at 288 $^{\circ}$C. Typical test results are shown in Figure 50. The momentary crack growth during the tests was measured with the DCPD (Potential drop) technique (ASTM E 647 1993). Further investigations for PSCFM device are based on the possibility to perform simultaneous multi- specimen testing at the same time in a high temperature water environment.

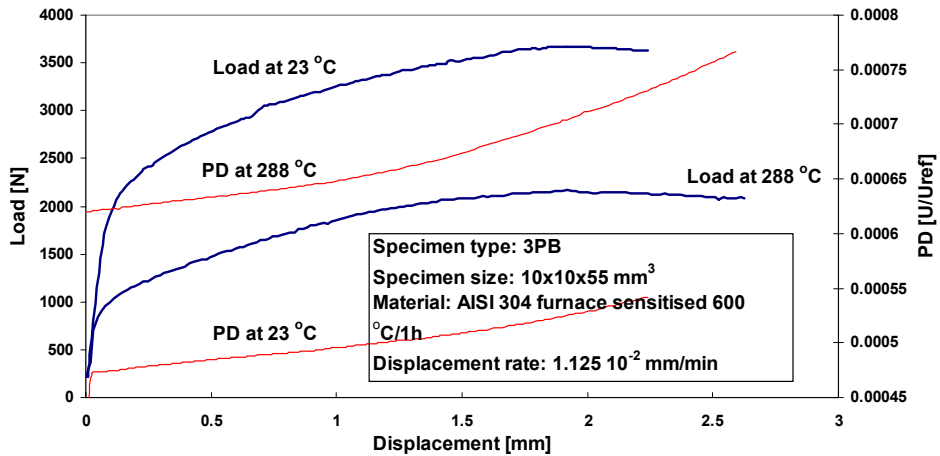*Figure 50. The test results for AISI 304 stainless steel at 23 and 288 ℃.*

7.2 Multi-specimen testing with PSCFM-device in high temperature aqueous solutions

As an example of a test set-up for multi-specimen tests, the test lay-out for simultaneous testing of six specimens in a BWR environment is presented in Figure 51.
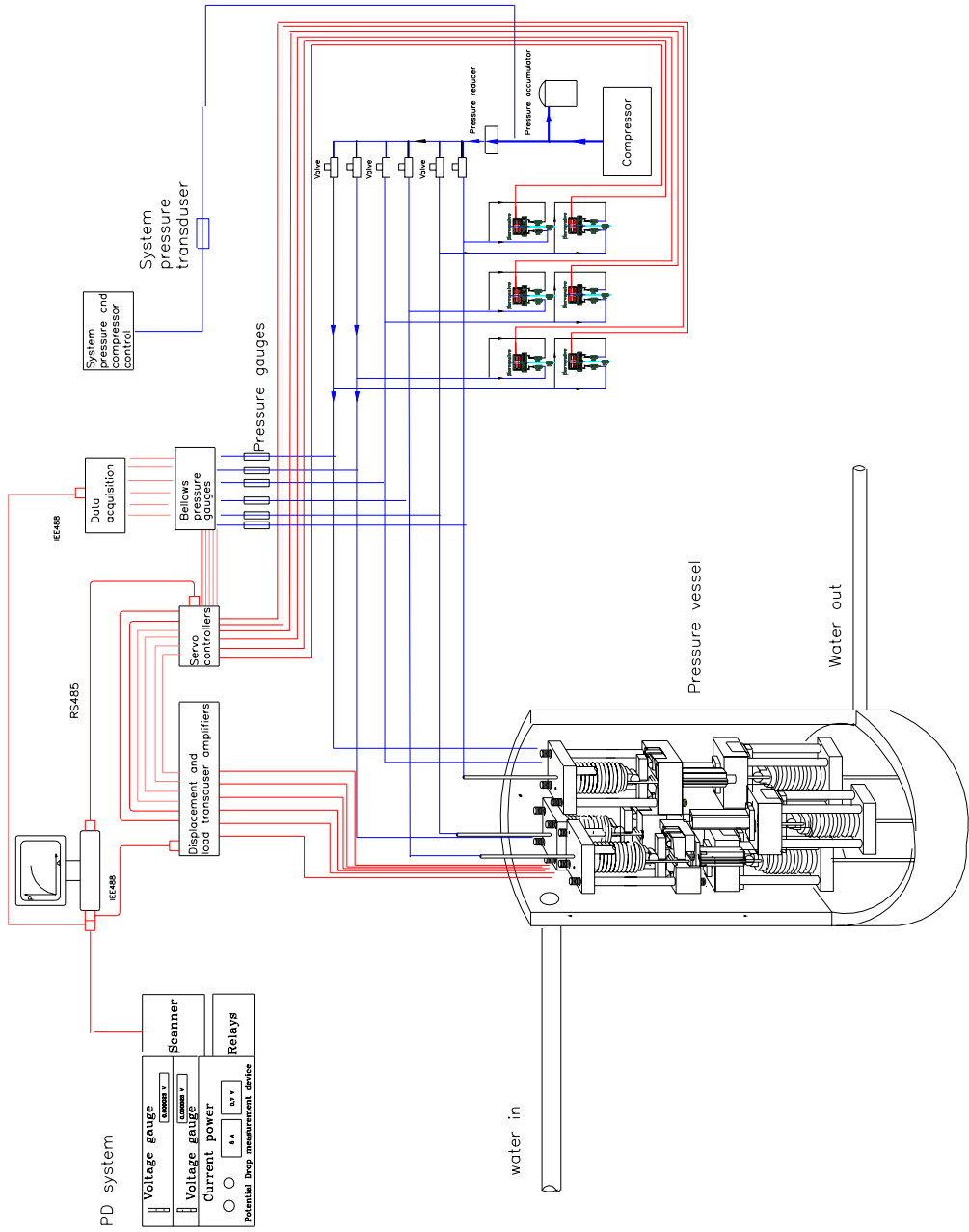
Figure 51. Test lay-out for simultaneous testing of six specimens at the same time.

99

7.2.1 Load and displacement accuracy for multi-specimen testing in a typical BWR environment

The pressure of the autoclave and bellows, displacement of the bellows and PD signal were measured during the multi-specimen testing. The pH, conductivity and dissolved oxygen content of the water were controlled using a re-circulation loop.

The measured accuracy of the LVDT sensor with the amplifier without loading devices at room temperature was around $\pm$ 0.02 μm and under high temperature water around $\pm$ 0.5 μm. The displacement rate in the first multi-specimen test was $1.2*10^{-5}$ mm/min for each specimen. In the second test series the displacement rates for five specimens were $1.2 \ 10^{-6}$ and $3*10^{-6}$ mm/min for one specimen. Figure 53 shows the displacement of each of the bellows as a function of time. The maximum fluctuation in the displacement was $< \pm 2$ μm. According to the ASTM-1152-87 standard the increase in the displacement has to be linear during a constant displacement rate (rising load) test and the fluctuation in the displacement can at maximum be ± 3 μm to 0.3 mm of displacement and after that $\pm$ 1 % of the total displacement (see Figure 54). Thus, these requirements were achieved in performed tests.

The unavoidable pressure variation of the autoclave re-circulation loop (environment pressure) can be accounted for using the LVDT sensor. The servo-controlled bellows pressure adjusting loop with sensitive bellows is able to react very fast to this kind of short period pressure changes. The maximum allowed pressure variation of the autoclave re-circulation loop is 0.5 MPa. The pressure changes of the re-circulation loop during the multi-specimen test were within $\pm$ 0.15 MPa. This pressure variation of the re-circulation loop did not affect the pressure difference (the bellows pressure minus the autoclave pressure) as shown in Figure 52. A short interruption in distribution of electricity occurred during the test, resulting in a sudden loss of pressure of the bellows. The autoclave pressure reacted much slower to the transient than the bellows pressure. In such a case the pressure difference decreases, which means that the load directed to the specimen also decreases, protecting the specimen from overload.
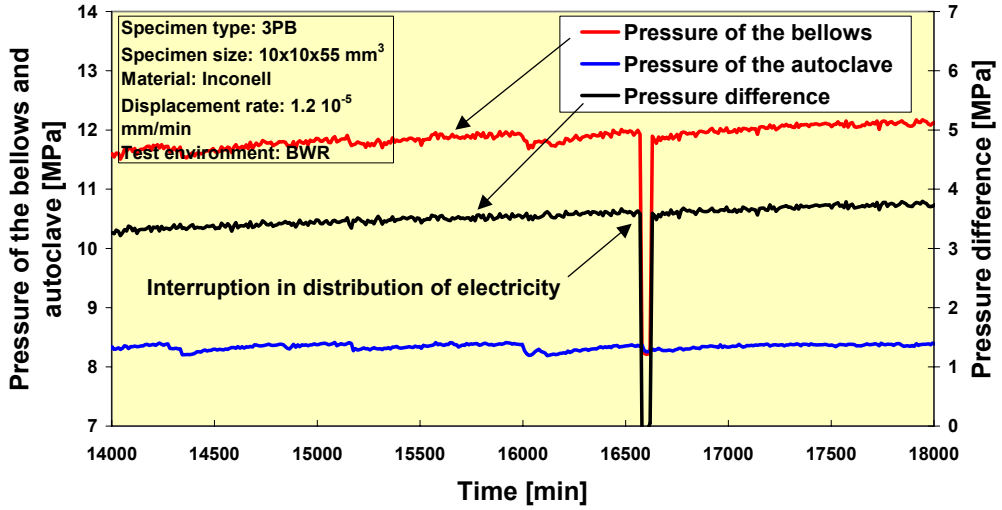
Figure 52. The bellows and environment pressure and pressure difference as a function of time.
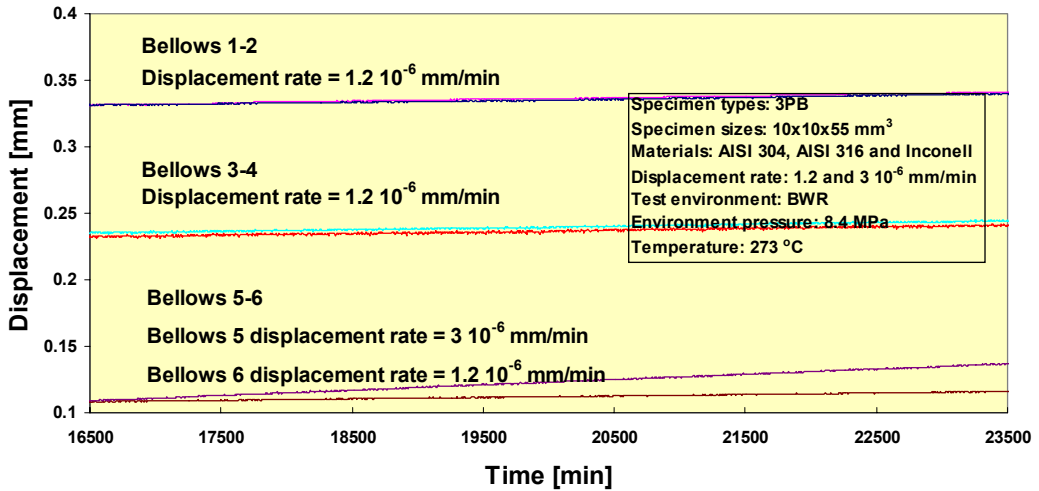
Figure 53. The displacements of the bellows during multi-specimen testing.

Specimen type: 3PB
Specimen size: 10x10x55 mm3
Material: Inconell
Displacement rate: 1.2 10^{-5} mm/min
Test environment: BWR
Environment pressure: 8.4 MPa
Temperature: 273 ^{o}C

Raw data from LVDT

ASTM standard limits for displacement

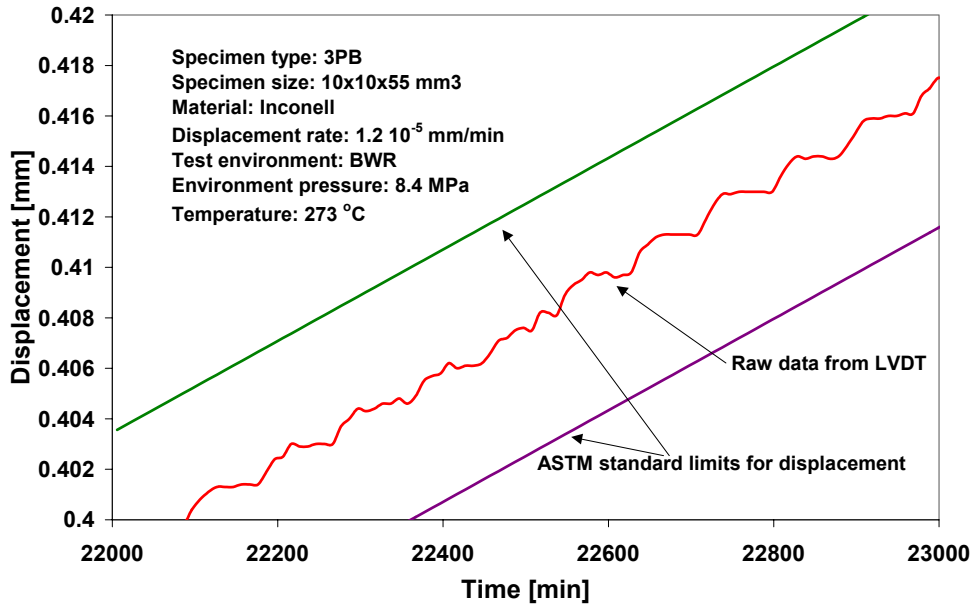*Figure 54. The displacement accuracy for one loading unit.*

The load curve with ESIS P2P deviation (± 1% from measured value) limits as a function of displacement during BWR environment testing in pressure vessel specimen testing are shown in Figure 55. The load and displacement accuracy during the rising load tests was good and satisfies ASTM and ESIS conditions. [12, 77]
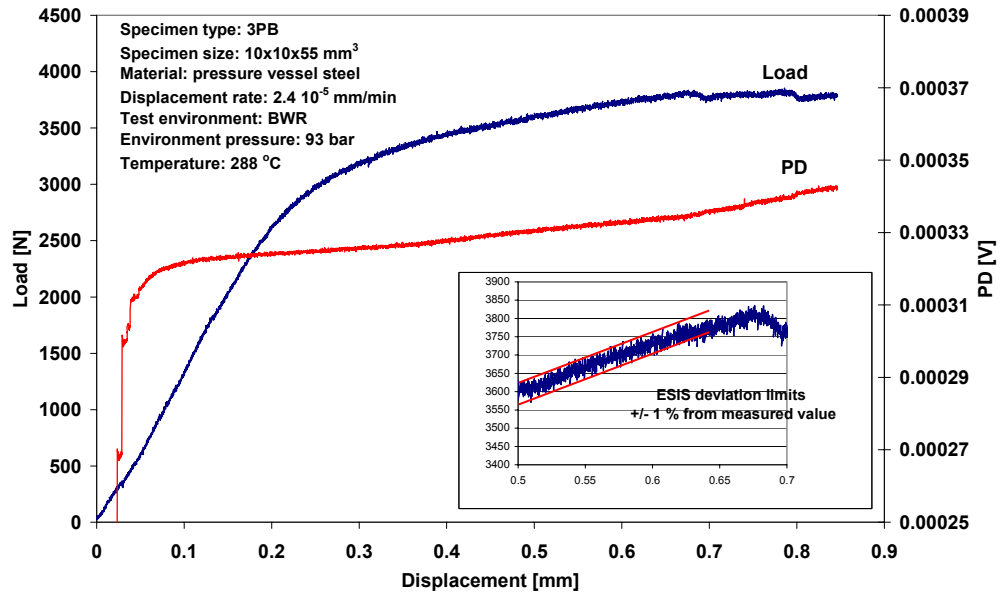
Figure 55. The test load and PD-signal as a function of displacement.

7.2.2 Impact of the load and displacement accuracy on the fracture type of SCC

As shown in theoretical parts of this thesis, the accuracy of the load and the displacement (or strain) can have an affect on many material parameters (see chapters 2 and 3). The investigations on load and displacement accuracy effects were performed with four independent long time test series using PSCFM device with six specimens. The test environment was BWR, specimen type was a three point bend specimen and constant displacement rate was $2,5*10^{-8}$ mm/s. There is evidence that load and displacement accuracy can affect the fracture type of IG or TG. One of the six pneumatic loading units had more inaccuracy compared to the other five and the same behavior was repeated in other test series. The reason for this inaccuracy with one pneumatic loading unit was probably due the inaccuracy of the LVDT sensor and the pneumatic pressure adjusting loop with amplifiers. The displacements and pressures as a function of time for one test with AISI 316 stainless steel specimens are shown in Figure 56. The displacement accuracy was about ±1 μm for specimen number 3 (and for four other specimens) and ±2 μm for specimen number 4 as shown in Figure 56. The

load accuracy calculated from pressure presented in Figure 56 was quite small: specimen number 4 load accuracy was around 5 % smaller than load for specimen 3.

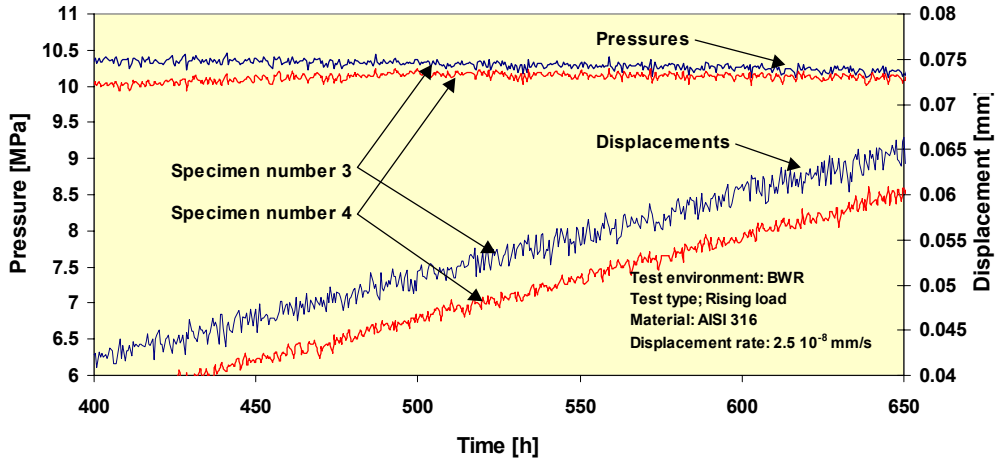*Figure 56. The pressure and displacement accuracy during rising load test.*

The DCPD (Potential Drop) curves for both specimens are shown in Figure 57. According to these curves specimen number 3 crack growth rate seems to accelerate as a function of time. One reason for this acceleration process could be load and displacement accuracy as shown above.
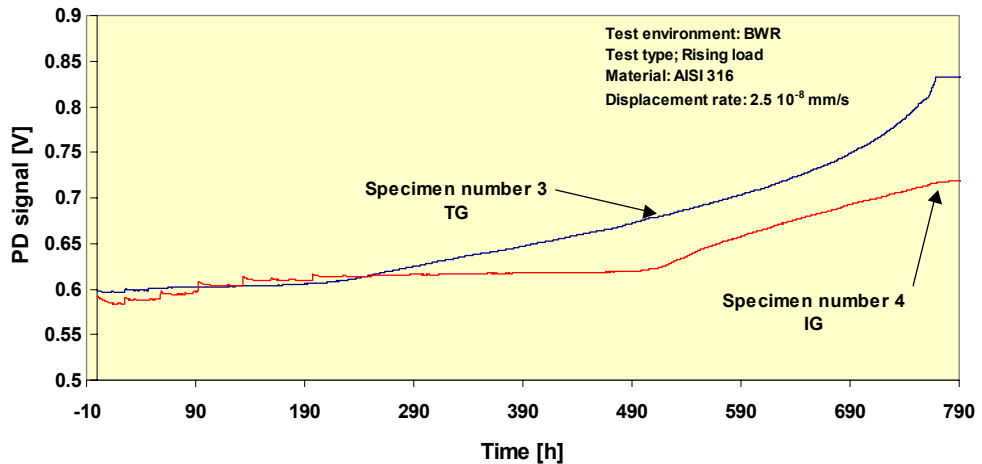
Figure 57. PD signals as a function of time.

There is clear evidence in the microstructure pictures of the changes in fracture type between TG and IG. Figure 58 illustrates the microstructure of the specimen number 3. The crack has grown mainly as a TG fracture type. IG type fracture mechanism dominated in number 4 specimen as shown in Figure 59.

Figure 58. Displacement rate = 2.5×10^{-8} mm/s. Mainly TG crack growth and crack growth rate increased during the test (see Figure 56, specimen 3).
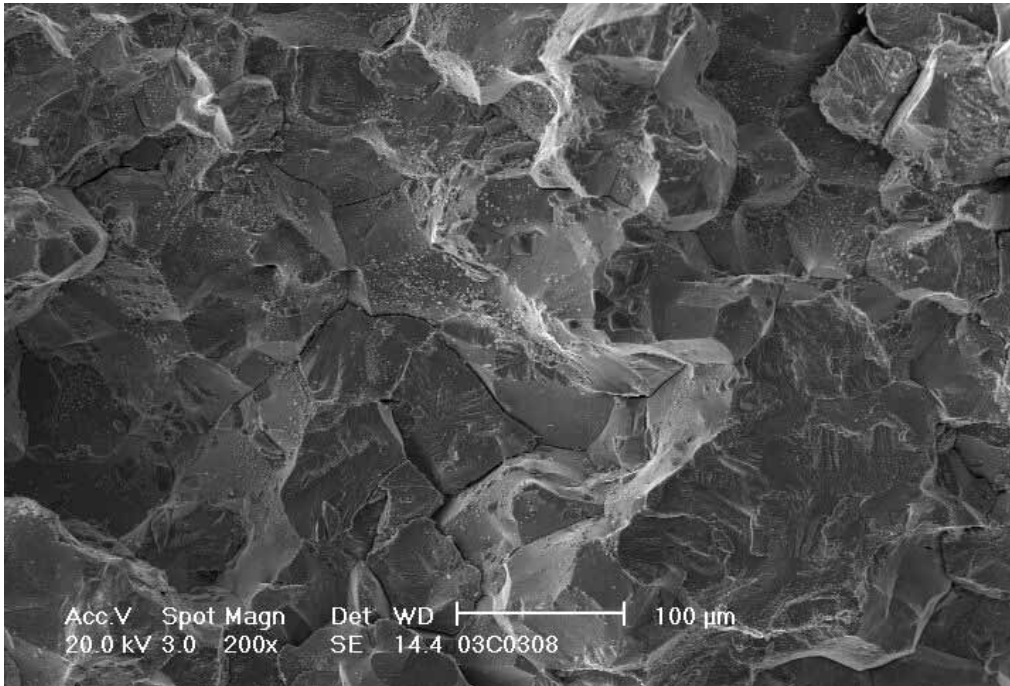
Figure 59. Displacement rate = 2.5x10^{-8} mm/s. Mainly IG fracture mechanics and crack growth rate was constant during the test.

This change in fracture mechanism can be affected by the accuracy of the test load and displacement and naturally by the material properties themselves. In any case, the microstructure was similar for all six specimens (two of them are shown in Fi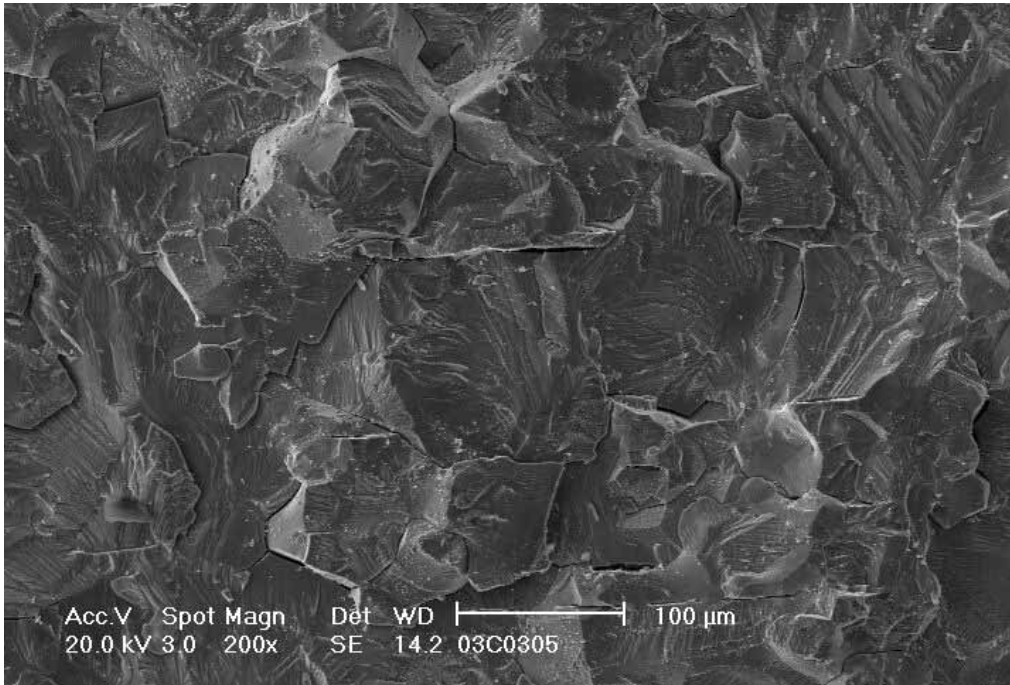gures 58 and 59). The environment was also the same for all six specimens because they were tested in the same autoclave at the same time. These test series proved how important a role the displacement accuracy has in the case of EAC. The overall sensitivity of the pneumatic testing unit comes mainly from two factors. As the moving parts that penetrate the pressure boundary are not needed, the friction force at the sealing element is avoided. Furthermore, the size of the load frame is small i.e. the thermal expansion of the load frame posts is also relatively small. Therefore load control with the pneumatic loading unit is more accurate than with conventional servo-hydraulic devices.

7.2.3 Effects of anionic impurity on crack growth rate of Inconel alloys

The PSCFM-device, was used to determine crack growth rates for Inconel weld materials as a function of sulphate content of BWR coolant. Test materials were Inconel weld metals 182 and 82 in as welded and in thermally aged condition. The thermal aging was carried out by 200 h annealing at 400oC. The chemical compositions of test materials are presented in Table 2. The specimens were pre-cracked SEN(B) specimens with 10x10 mm2 cross section. Specimen geometry is presented in Figure 60.

Table 2. Chemical compositions, w%, of the test materials, weld metals Alloy 182 and 82. The chemical compositions were provided by the weld electrode manufacturers.

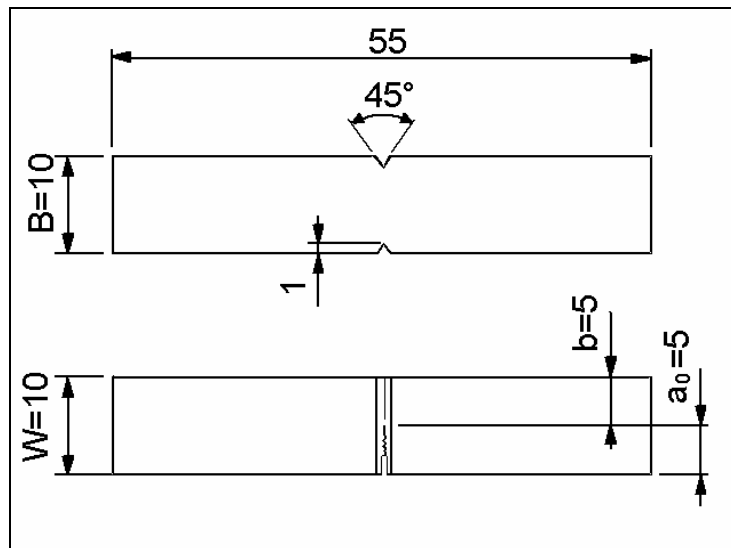|	Fe	C/N	Cr	Mn	Si	S	Ti/Mo	Ni
Alloy 182	8.07	0.03/-	15.24	7.57	0.52	0.001	0.52/-	Bal.
Alloy 82	0.71	0.036/-	20.23	2.92	0.05	0.001	0.38/-	Bal.

Figure 60. Main dimensions (in millimeters) and geometry of the specimens.[78]

The tests were performed with very slow rising displacement rates (2×10^{-8} mm/s) or, in some cases, using constant displacement. Loading geometry was three-point bending. Several test series were performed. Four to six specimens were loaded simultaneously in each test series in the same autoclave using PSCFM device with separate loading frames and instrumentation for each specimen.

Crack length was monitored using reversing Direct Current Potential Drop (DCPD) method during each test. The momentary crack lengths were calculated using the closed form expression for potential drop calibration presented in standard ASTM E 1737-96 [12]:

$$\frac{a}{W} = \frac{2}{\pi} \cos^{-1} \left[\frac{\cosh\left(\dfrac{\pi y}{2W}\right)}{\cosh\left[\left(\dfrac{U}{U_0}\right) \cosh^{-1}\left[\dfrac{\cosh\left(\dfrac{\pi y}{2W}\right)}{\cos\left(\dfrac{\pi a_0}{2W}\right)}\right]\right]} \right] \tag{48}$$

where y is the distance of the potential drop leads from the crack plane, U is momentary voltage difference between the leads, W is specimen thickness, a is crack length and U_0 is the initial voltage difference between the leads. Loading geometry and DCPD lead locations are shown in Figure 61.
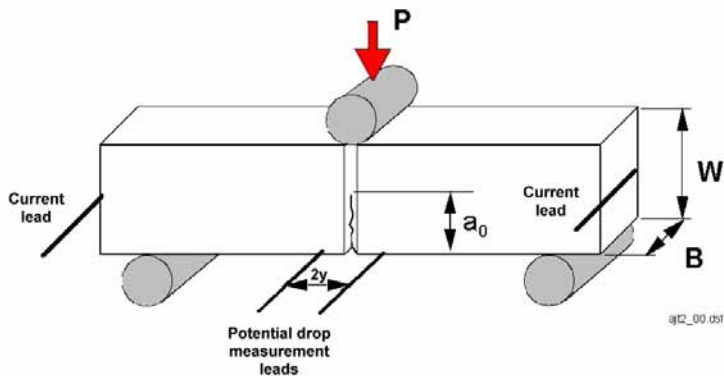

Figure 61. Loading geometry and locations of the DCPD leads are also shown. [78, 79]

J-integral levels were calculated using the procedures presented in standard ASTM E 1737-96 with formulas (26), (27), (28), (29) and (30) from the theoretical part of this thesis.

The test environment was a simulated BWR environment: temperature 273 $^{\circ}$C and outlet oxygen content 300 ppb. Diluted H_2SO_4 pre-mixture solution was added into high-purity inlet water by a liquid chromatograph pump. The flow rate of the injected solution was used to adjust the concentration of SO_4^{2-} in the water. The outlet flow was purified with ion exchangers before returning the water into re-circulation. The re-circulation flow volume through the autoclave was 0.3 l/min, which means that the autoclave water was refreshed every 20 minutes. The water chemistry parameters for the outlet water and inlet water (pH, conductivity and dissolved oxygen content) were measured continuously at ambient temperature. Corrosion potential was measured using an Ag/AgCl (0.01 M KCl)-electrode and it was around +100 mV SHE.

An example of a typical load-displacement curve of Inconel alloy 182 with the effects of sulphate intrusions is shown in Figure 62. The load starts to decrease quickly after sulphate is injected into the autoclave inlet water because of crack growth. When the sulphate intrusion is finished, the load decrease rate begins to slow down immediately. The effects of the sulphate intrusions on the crack growth rates can be seen in Figure 63, which shows the crack length vs. testing time in five simultaneously loaded specimens, three Inconel alloy 182 and two alloy 82 specimens. The lowest crack growth rates were measured in pure water prior to the first sulphate transient. The injection of a small amount of sulphate, producing a minor increase in the conductivity of the outlet water, affected the measured crack growth rate considerably in the case of Inconel alloy 182.

The effect of increased sulphate concentration on crack growth rate became visible after a 25–45 h incubation period. Purification of the water started to slowly decrease the crack growth rates. However, the crack growth rates did not decrease back to the starting value, at least not within a couple hundred hours after the sulphate intrusions.

The crack growth rates measured for alloy 182 in both welded and thermally aged condition in simulated BWR environment with various sulphate concentrations are shown in Figure 64 as a function of K_J. The results are

collected from several test series in which several specimens were tested simultaneously. SKIFS 94:1-curve in Figure 64 is a Swedish design line under which all of the laboratory crack growth rate measurement values on alloy 182 were from before 1994 (measured at 288°C with water conductivities up to 0.3 µS/cm) [80]. The other curve is a curve fitting made by Morin et al. [81] to laboratory data they had collected from literature (conductivities up to 0.3 µS/cm).

According to these results the sulphate content of BWR coolant can significantly affect crack growth rate of Inconel 182 weld material.
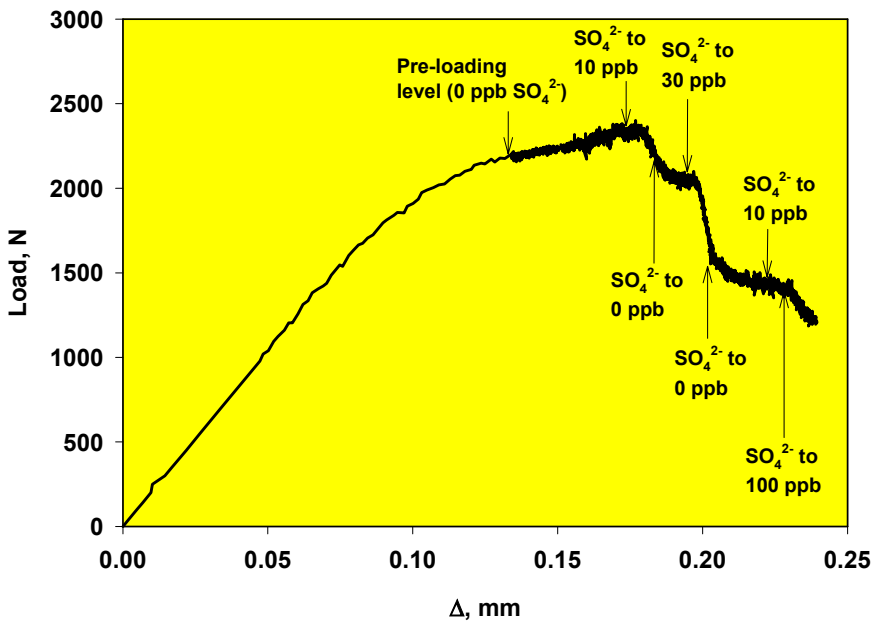
Figure 62. An example of a typical load-displacement curve of Inconel alloy 182 with the effects of sulphate intrusions. [78, 79]
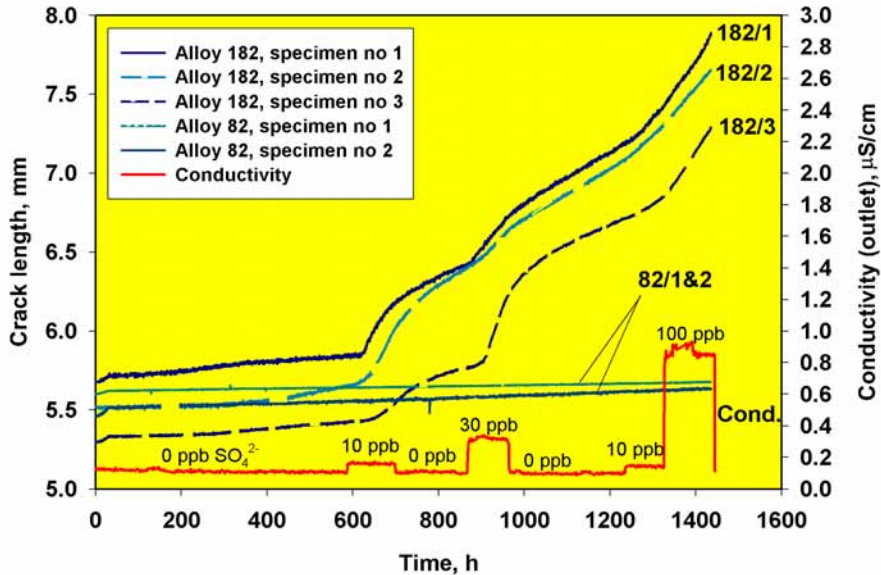
Figure 63. Effect of the sulphate intrusions on the crack growth rates in Inconel alloys 182 and 82.
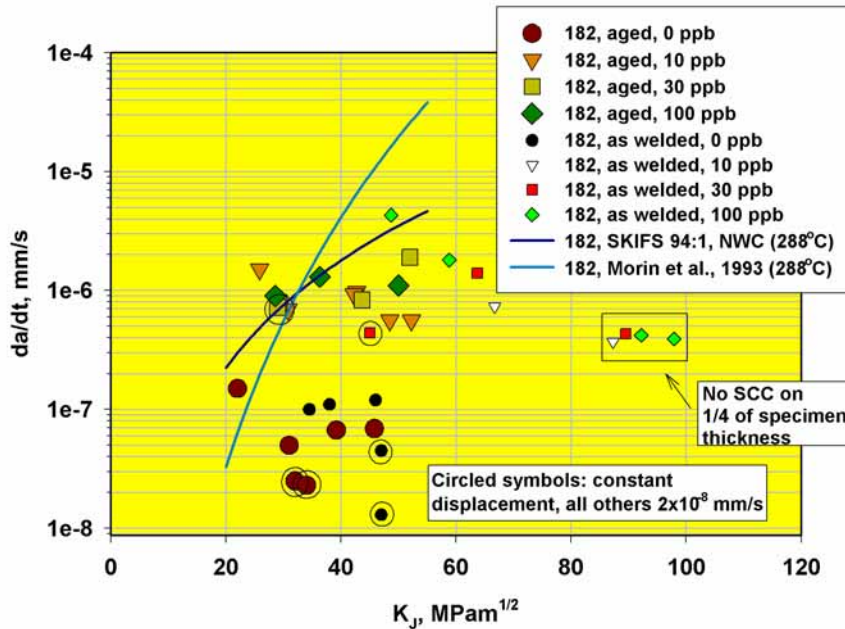
Figure 64. Crack growth rate results of Inconel alloy 182 collected from several test series in which several specimens were tested simultaneously. Two disposition lines (288°C) for Inconel alloy 182 are also marked in the figure.[78,79, 80, 81]

This tests verified that the servo-controlled fracture resistance measuring device is suitable for performing constant load and displacement rate tests for small three point bend specimens in BWR environment. The pre-set displacement rate was achieved accurately in the tests and it was constant during the test even with very slow (2 10^{-8} mm/min) displacement rates. The load and displacement accuracy during the rising load tests was good and satisfies ASTM conditions. The pressure variations of the autoclave can be accounted for by using pneumatic servo controlled pressure adjusting loop with LVDT sensors feed back signal. According to rising load tests in BWR environment the load and displacement accuracy can have an effect on the damage type of SCC i.e. fracture type can be changed between intergranularly or transgranularly as a function of accuracy of load and displacement for AISI 316 stainless steel.

Furthermore, the PSCFM measuring device was used to determined crack growth rates for Inconel 182 weld material as a function of sulphate content in BWR coolant. According to these results, the sulphate content of BWR coolant can significantly affect crack growth rate of Inconel 182 weld material.

7.3 Test results from pneumatic PSCFAT-device

The primary goal was to develop and test a prototype of the fatigue device which is capable of performing axial fatigue testing in PWR autoclave. The study consists of dynamic calibration of the pneumatic loading, determination of the specimen alignment class and a demo test in a gas environment at 100 °C [75, 82]

The dynamic calibration for the pneumatic fatigue loading unit was performed using a hydraulic material testing system (MTS). Figure 65 shows the procedure for dynamic calibration at room temperature using hydraulic testing system. The main idea of these tests was to determine the fatigue bellows effective cross-section by using two different calibration systems at room temperature. The calibration system consists of a pneumatic fatigue loading unit, MTS hydraulic testing system and a calibration specimen with eight strain gauges. The tensile force was provided by the MTS testing system and the compressing force by the pneumatic loading unit. The load range during calibration was -700 to 3200 N, the wave form was triangular ramps with frequency 0.1 to 1 Hz and the strain

range of the specimen was ±0.025 mm. Figure 66 shows the typical calibration load curves during fatigue cycles.

The effective cross section was determined by using equation (45). According to dynamic calibrations, the effective cross section of the fatigue bellows was 1060 mm^2 (compared to 1050 mm^2 in normal calibration). [75]
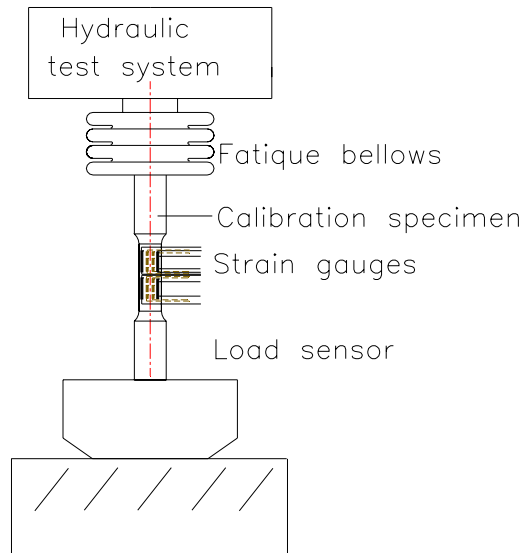
Figure 65. Schematic presentation of dynamic calibration system. [75, 82]

Also load and pressure normal calibrations for the pneumatic fatigue loading unit were performed using the calibration furnace system described earlier. The bellows stiffness of the pneumatic fatigue loading unit was non linear as can be seen in Figure 67. The normal calibration results are presented in Figure 68. [75]

Figure 66. Test result from dynamic calibration at room temperature.[75]

Figure 67. The fatigue bellows stiffness and the friction fall of the pneumatic loading unit as a function of displacement.

Figure 68. The relationship between measured and calculated loads of the pneumatic fatigue loading unit by using calibration furnace.

The difference between the dynamic and normal calibrations (presented earlier) is the direction of the load and the required displacement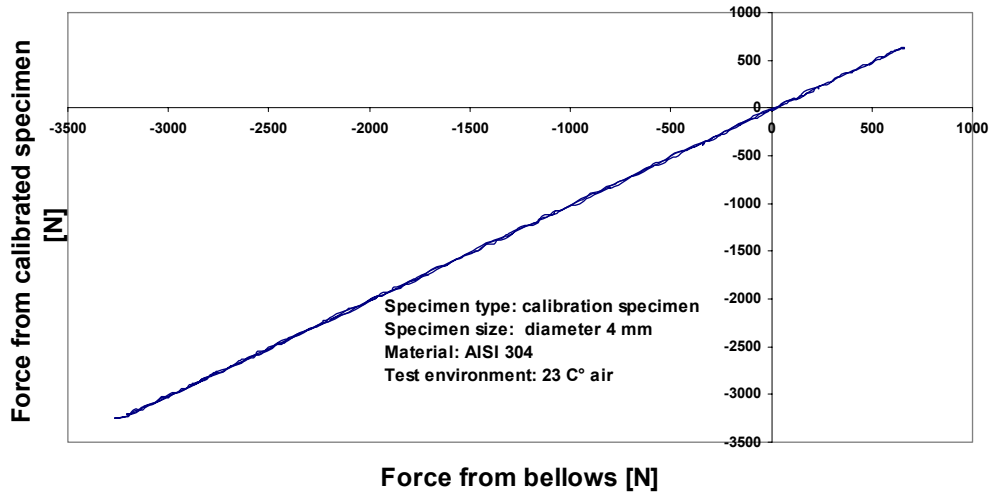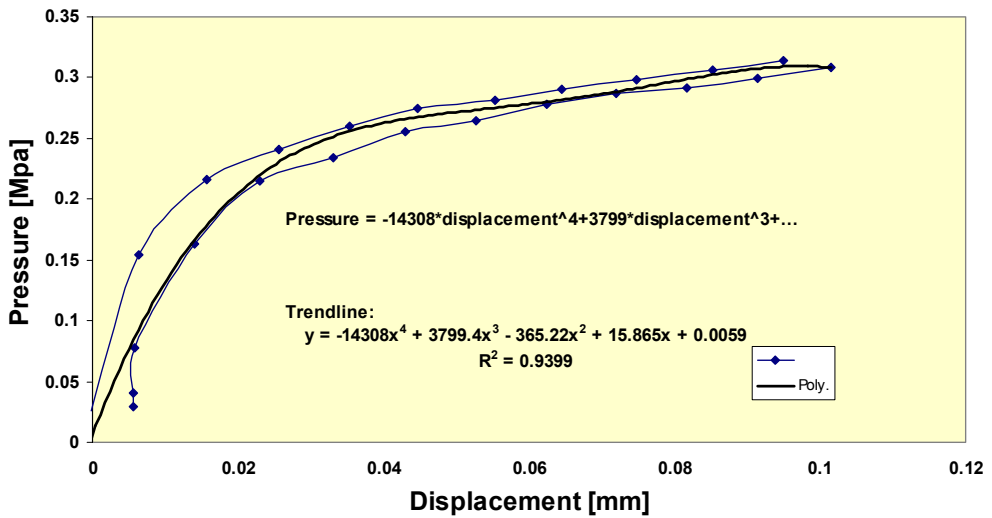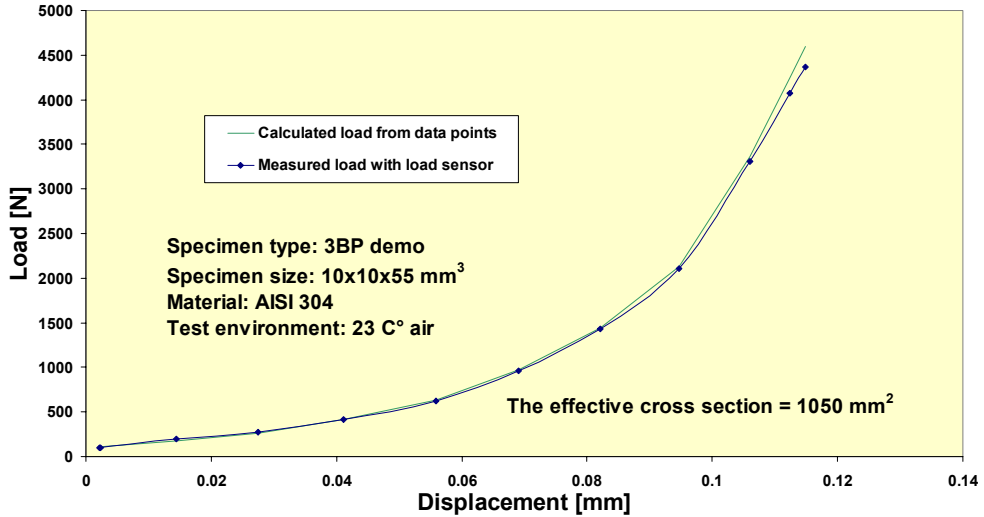 range. In normal calibration, the load of the pneumatic loading unit is always one-directional (specimen bending, bellows pressurizing) whereas in dynamic calibrations the load direction is changed. In the fatigue calibration the needed displacement is smaller, approximate 0.03 mm. [75]

The determination of specimen alignment class is performed using MTS material testing system with specimen equipped with 8 strain gauges and with the program ALIGNCAL. According to this test, the alignment class for fatigue specimen was 20. Alignment class 10 should be attainable by conventional LCF test systems in qualified test laboratories.

Class 2 is reserved typically only for very brittle ceramic materials and is not achievable by most test laboratories. For the prototype fatigue unit the measured alignment class was 20 and it was in reality just outside the window for class 10 (maximum 10% bending). [82]

The fatigue demo test was performed using a round $\varnothing$ 4 mm fatigue specimen. The gage length was 10 mm. The specimen material was AISI 304 SS.

The pressure of the autoclave was 12 MPa and temperature 100 °C. The sine wave was used with 0.1 Hz frequency.

Figure 69 shows the stress and strain signals vs. time measured during a complete load cycle. The signals in this figure have been filtered. In reality there are some ripples of about ±0.0001 magnitude in the control strain. This is probably due to the coarseness of the LVDT used to measure strain.
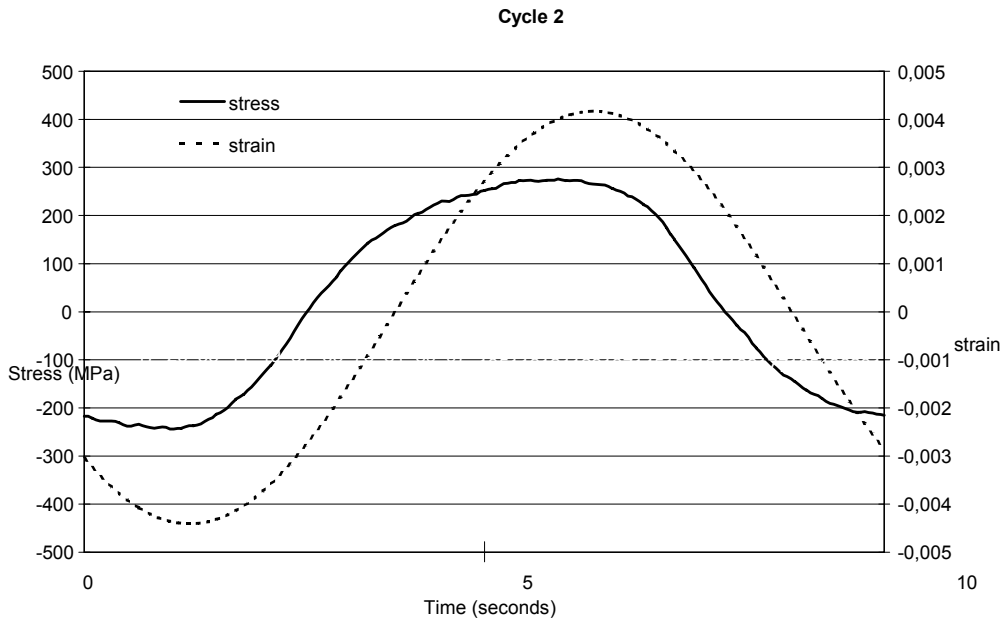
Cycle 2

Figure 69. Measured and filtered stress and strain signals during one fatigue cycle.[75]

The strain controlled fatigue test operated without difficulty for two days and 15600 fatigue cycles. The specimen failed at its midsection due to fatigue.

For comparison purposes, the data collected in this pre-study is plotted with the previously published data for AISI 304 stainless steel in Figure 70 and 71. Figure 70 shows the strain life data and Figure 71 gives stress-strain data. These graphs include the Argonne National Laboratory data, but do not represent tests in LWR coolant. The tests were performed at ambient and elevated temperatures [83].

116

In both figures the current data lies right in the middle of the published data. The two stress-strain curves in Figure 71 are for room temperature and 288–430°C elevated temperature tests. As expected, the 100°C data point from the current study falls between the curves for the other two temperature ranges. The stress amplitudes shown were measured at $N_f/2$. Results from the strain controlled fatigue test were in good agreement with data from VTT and other laboratories generated using more conventional test systems.
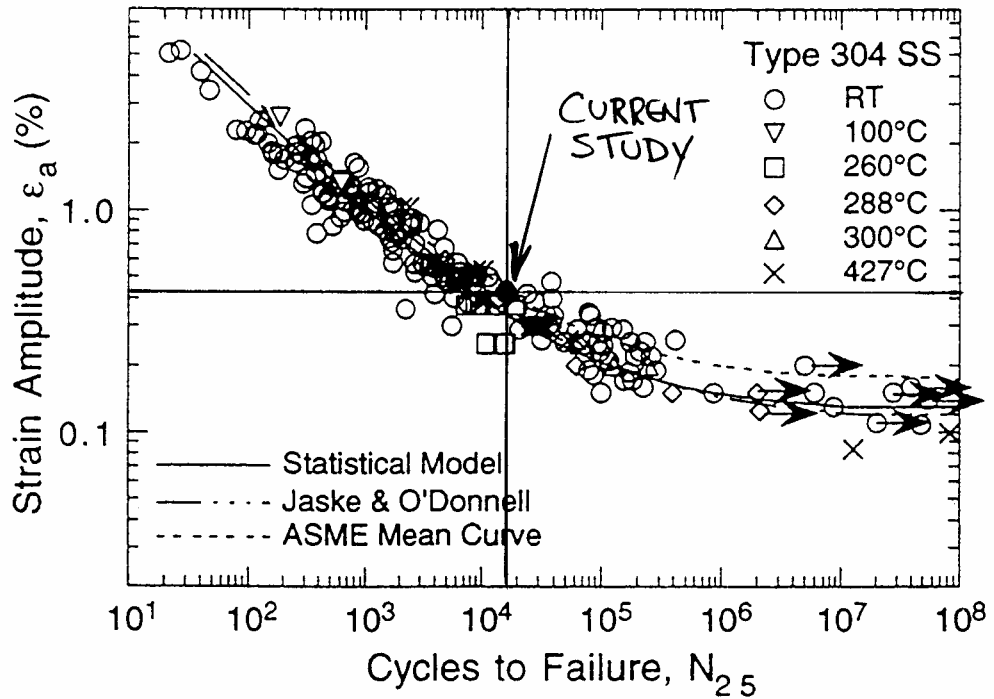
Figure 70. Comparison of the current test data with published strain-life data [83].
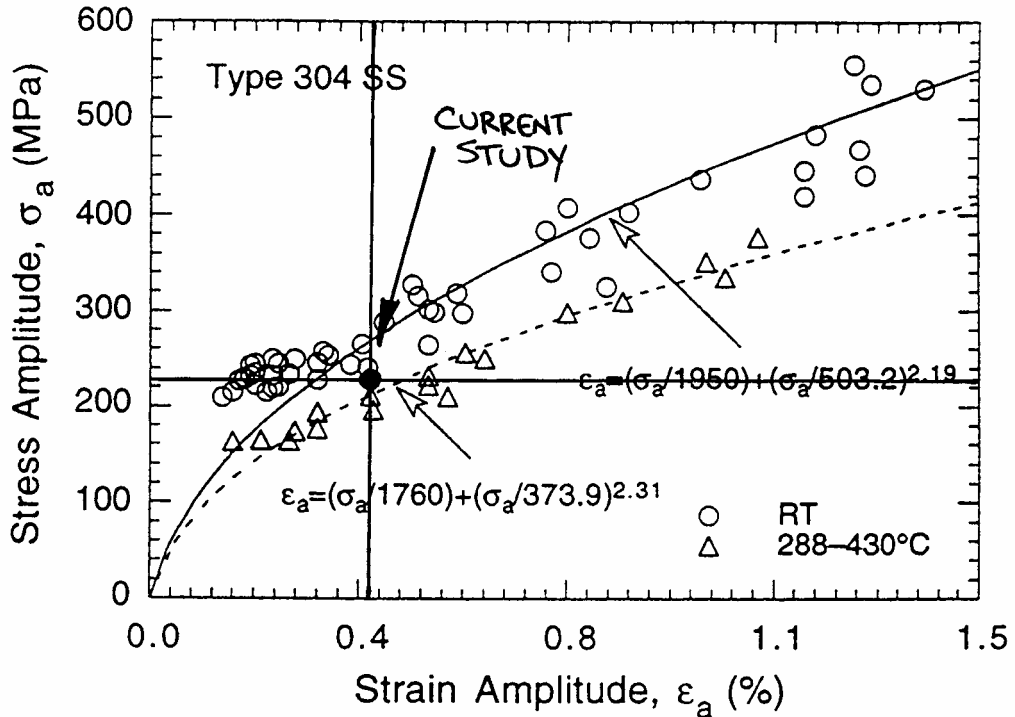
Figure 71. Comparison of the current test data with published stress-strain data [83].

7.3.1 Discussion on test control and monitoring

As seen in Figure 69, the strain control was very stable during the fatigue test. The ripples in the control strain of about ±0.0001 in magnitude are at least partially due to the coarseness of the LVDT used to measure strain. These ripples of ±0.0001 in strain correspond to an LVDT measurement accuracy of 1 µm which is the precision limit expected for this device intended to measure displacements of ±5 mm. Some improvement could be made by a more sensitive LVDT and perhaps by using more fine tuning of the bellows control system.

Test control during the verification tests was accomplished using the PSC II computer program provided with the bellows servo controller card (by Moog). This program has the advantage in that it is designed specifically to work with the air pressure servo valves and has all the functions needed for testing. The program, however, is not easy to use. Difficulties with the program would be

118

compounded when dual valves are used to control a single test and as many as six fatigue units must be controlled simultaneously. There is clearly a significant opportunity for operator error. In short, the PSC II software gets a good score for functionality but a bad score for user friendliness. Possibilities for improving user friendliness should be explored. Various hardware and software were used for control of loading and data acquisition in these verification tests. At least in the near future, use of this approach will probably continue.

Data collection was accomplished during the verification tests using the MTS Test Star program. This is not a practical solution during normal testing because the MTS system is designed to be used in conjunction with a test frame. Our dedicated PC programs for fatigue testing [5] are not directly applicable for the purpose. A new simple PC based program should be developed for this purpose.

Several programs for field measurements have been developed based on the DASY lab modular software program. These could probably be adapted for fatigue test monitoring with little difficulty. A simple PC with measurement card could then be used for test monitoring and data collection. A single PC should easily be able to handle a six specimen test.

The safeguards for VTT autoclave testing systems are based on significant experience and work well for tests performed to date. However, new measures are needed. Because the loads are based on pressure differences, a system for long term tests would need to have several built in links between autoclave control systems and the bellows control system. For example, loss of autoclave pressure would possibly buckle the specimen and damage the bellows unless appropriate safeguards are included. Loss of bellows pressure, on the other hand, would overload the specimens and invalidate the results. Loss of bellows pressure would result from a servo valve or air supply failure. A duplicate (2+2) valve system will probably add redundancy and reliability, but air the supply should also be considered. Simultaneous dynamic loading of multiple specimens requires anyway an increased air flow capacity. When purchasing this, the redundancy can be accounted for by the same.

The further fatigue test results in PWR environment has been published in reference number 87.

7.4 The test results from pneumatic CDE-device pre-study tests

The first part of the pneumatic CDE-device tests was performed in room temperature. The movement of the electrodes was measured by an LVDT sensor. According to the LVDT sensor, the accuracy of the electrode movement was ± 0.1 μm. This is accurate enough for measurements with the pneumatic CDE-device.

The following test was performed under typical BWR conditions. At room temperature the noise level in the LVDT sensor was ± 0.05 μm, but under BWR conditions it was measured to be as high as ± 0.3 μm. Therefore the reading accuracy of the LVDT sensor was less than what is necessary for a successful CDE measurement. In any way the accuracy of the electrode movement under BWR environment was better than 0.7 μm, as shown in Figure 72. It has to be verified in further tests whether the target accuracy i.e. ± 0.3 μm, is achieved also under BWR conditions. According to our measurements, the best result for electrode movement was achieved when the pressure of the bellows and environment pressure were almost equal. In this case, the own stiffness of the bellows does not affect the electrode movement because the inside pressure of the bellows can move the bellows in one direction and the outside (environment) pressure in the opposite direction.
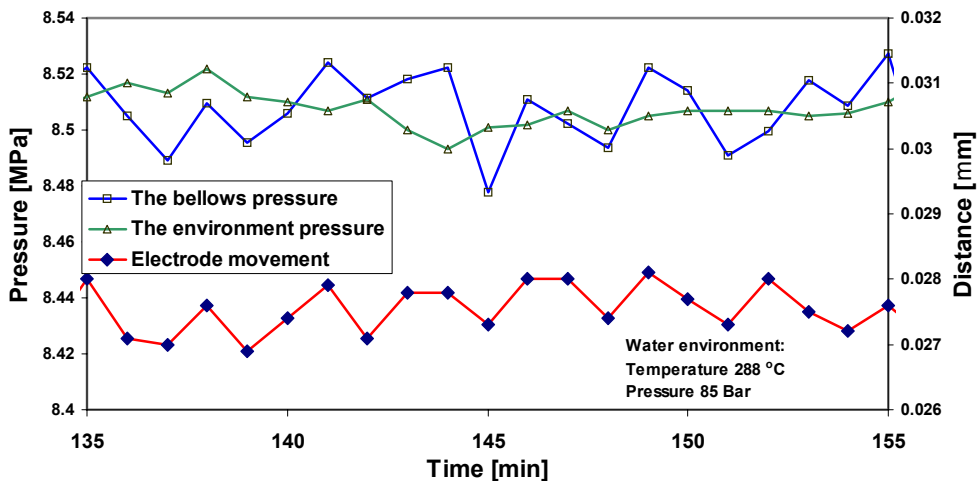

Figure 72. The electrode movement, the bellows pressure and the environment pressure in a test made under BWR conditions. [85]

When the system is operated under pressure control the pressure variation of the environment can affect the electrode movement. The electrode movement is measured by using four test series with seven steps. The starting point was zero level of the electrode and the finishing point about 0.13 mm of displacement. According to Figure 73 the environment pressure changed approx. ± 0.3 bar during the test series. This pressure variation resulted in a change of about 3 μm in the electrode position. This is too high and further development is needed to be able to run tests with the system under pressure feedback control. [85]
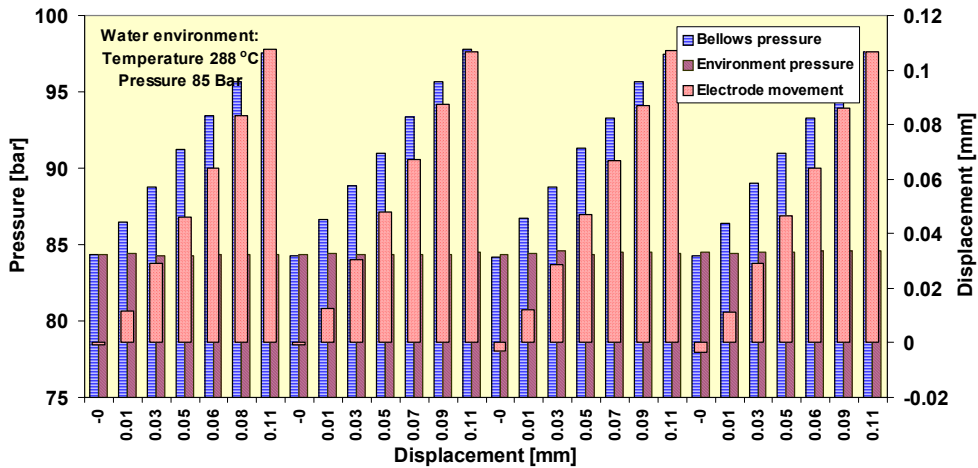
Figure 73. The effect of the environment pressure variation on electrode position. [85]

The bellows-driven single CDE arrangement had a sensitivity to pressure changes in the bulk environment. This was mainly because there was a direct connection from the bellows to the stiff spring. To decrease this sensitivity to pressure changes, new types of extra spring and bellows element shown in Figure 74 have been fitted. As a result, the spring constant produced by the whole system has been optimized.

The diameter of the new bellows is lower (reduction of the diameter from 22 mm to 19 mm) and the stiffness of the new extra spring is also lower than that of the previous ones. With the modified system shown in Figure 74 and Figure 75, a pressure variation of ±0.06 MPa can be estimated to produce an inaccuracy of <±0.12 μm in the distance between the two opposing surfaces of the bellows-

driven single CDE arrangement. The variation of ±0.06 MPa includes the commonly encountered variations of the pressure sensor of both the test environment and the pressure adjusting loop for the bellows. The former can be estimated to be ca. ±0.03 MPa in an autoclave loop and in a static autoclave, while the latter can be estimated to be of the same order of magnitude. A variation of ±0.12 μm can be considered sufficiently low to provide the accuracy needed for all the types of CDE measurements described above, in which the distance has to be controlled with an accuracy of ca. 0.2 μm.
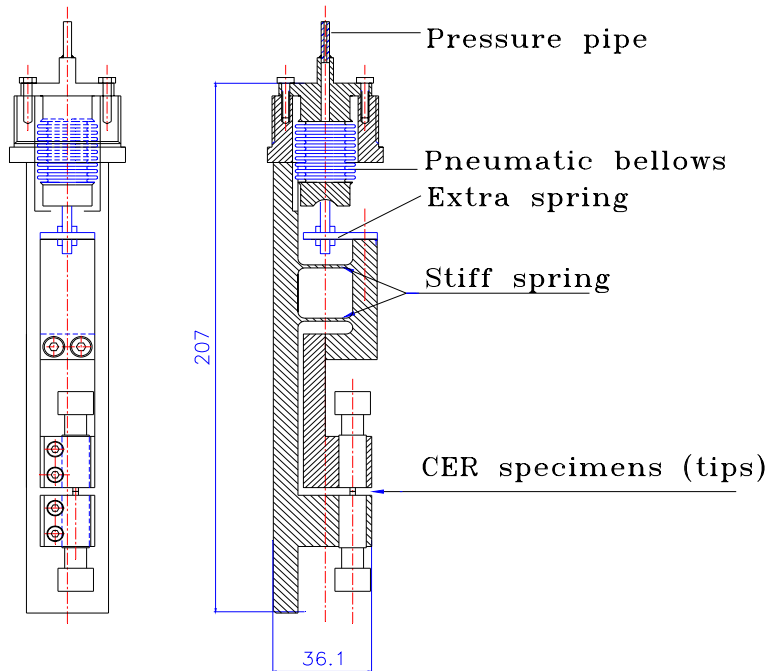

Figure 74. The bellows-driven CDE arrangement design with new types of extra spring and bellows elements introduced to reduce the system sensitivity to pressure changes in the bulk environment.
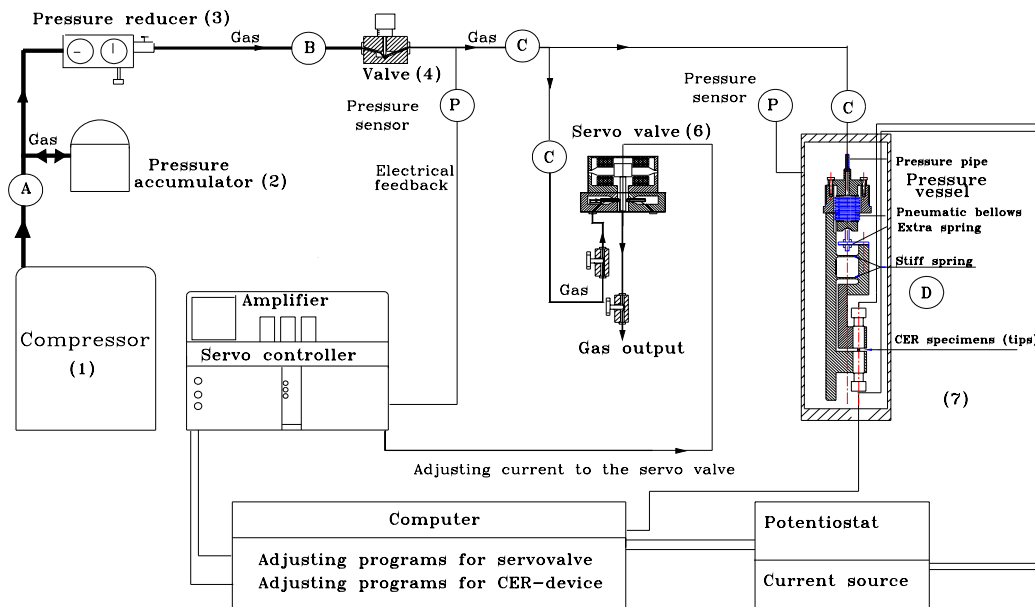
Figure 75. Scheme showing the bellows-driven servo pneumatic single CDE arrangement.

7.4.1 Results with the bellows-driven single CDE arrangement

The bellows-driven single CDE arrangement has successfully been tested in a static autoclave with low pressure variations at temperatures up to 250 ^{o}C. Figure 76 shows a comparison of surface film electric resistance of Ni measured with the conventional step motor - driven system and with the bellows-driven single CDE arrangement. The resistance was measured during a positive-going potential sweep starting from a pure Ni surface. The resistance at potentials lower than -0.6 V was equally low, indicating no formation of a surface film. At E > -0.6 V, the resistance increases due to the formation of NiO layer until a maximum value is obtained at ca. -0.3 V. At E > 0 V, a general decrease of resistance is observed. This decrease in resistance with increasing potential can be ascribed to the predominance of cation vacancies in the film structure leading to an apparent p-type semiconductor behaviour in the surface film forming on Ni in these conditions. The small peak at 0.3 V < E < 0.6 V is most probaly due to an oxidation process preceding the transpassive dissolution of Ni.

The results obtained with the modified bellows-driven single CDE arrangement and with the step motor - driven system are qualitatively and even quantitatively closely similar. The small quantitative differences can at least partly be ascribed to the generally poor reproducibility of this kind of experiments on pure Ni. The different slopes of the resistance vs. potential curves at -0.6 V < E < -0.3 V indicate a difference in the film formation mechanism, which may be a result of different prepolarisation times. Thus these differences are most probably not due to different measurement systems. One possible reason for the difference in the resistance levels at high potentials may be different contact pressures in the two measurements.
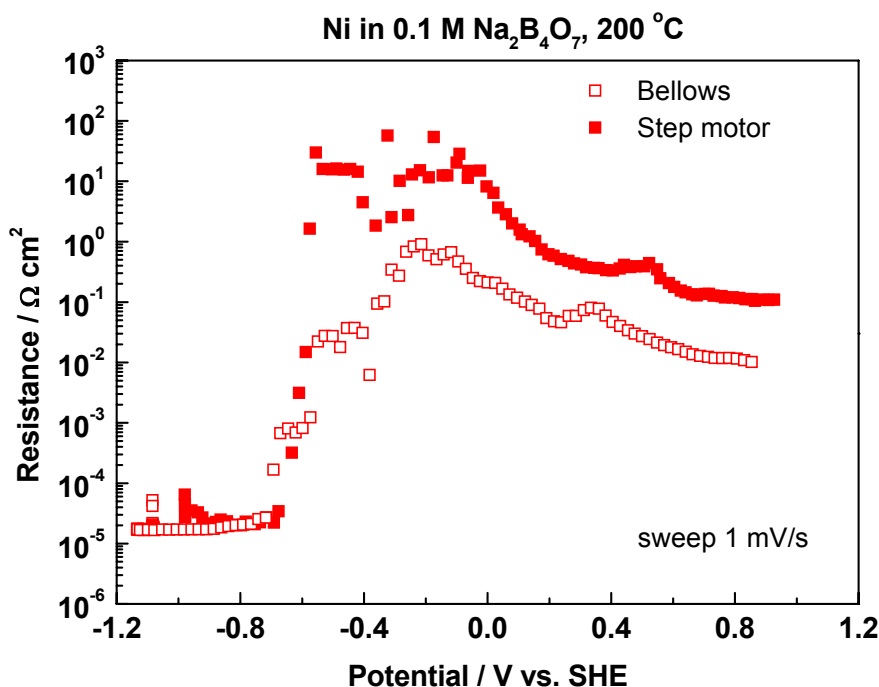

Figure 76. Comparison of surface film electric resistance measured with the bellows-driven CDE arrangement and the conventional step motor system at 200 °C in 0.1 M $Na_2B_4O_7$.

A comparison of the surface film electric resistance of the Ni-15%Cr-alloy at 200 °C measured with the conventional step motor-driven system and with the

bellows-driven single CDE arrangement is shown in Figure 77. The curves chosen for this figure comparing results obtained with two different systems are representative of the typical behaviour in a set of repeated experiments. The resistance has been measured during a positive-going potential sweep, and the sweep has been started with a freshly-polished electrode surface.

The curves obtained using both the systems show that the resistance at potentials more negative than -0.65 V is low, indicating that either no surface film is present or that the film thickness is low enough for electron tunneling to take place. At E > -0.65 V, a surface film is formed leading to an increase of the resistance until a maximum value is obtained at ca. -0.3...-0.2 V. This behaviour is very similar to what has been earlier found in the case of pure Ni [86], indicating that NiO or a closely similar product may be formed also in the surface film on the Ni-15%Cr alloy. At E > 0 V, a decreasing trend of the resistance is observed. This decrease with increasing potential can be attributed to the predominance of cation vacancies in the film structure leading to an apparent p-type semiconductor behaviour of the film forming on the Ni-15%Cr alloy. A closely similar behaviour has been found also in the case of pure Ni /85, 86/.

The main difference of the result gained for pure Ni in comparison with the present results for Ni-15%Cr is that the resistance level at -0.3 V < E < 0.3 V is roughly one order of magnitude higher for Ni-15%Cr. This is likely to arise from the contribution of Cr in the film structure.
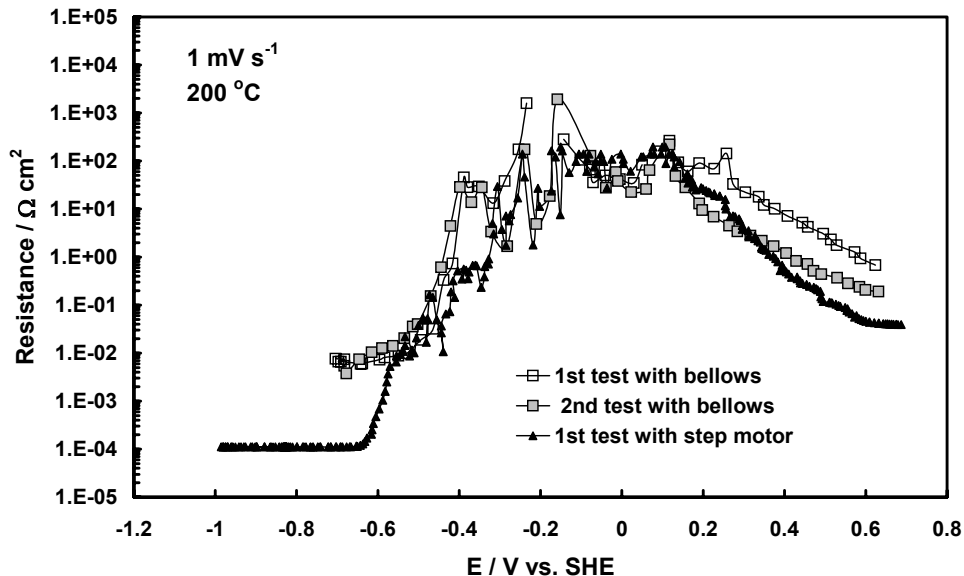
Figure 77. Comparison of the surface film electric resistance of Ni-15%Cr alloy measured with the bellows-driven CDE arrangement and the conventional step motor system at 200 °C in 0.1 M Na$_2$B$_4$O$_7$. [86]

The curves given in Figure 77 demonstrate a good qualitative and also a fair quantitative agreement between the results obtained with the bellows-driven single CDE arrangement and with the step motor-driven system. The small quantitative differences can at least partly be ascribed to the generally poor reproducibility of this kind of experiments on Ni-15%Cr that has been observed in earlier experiments with the step motor-driven system. The poor reproducibility may be due to the fact that the Cr content of the Ni-15%Cr alloy is at the limit where a dominating Cr$_2$O$_3$ -based surface film may form on the surface. Because the formation of a dominating Cr$_2$O$_3$ -based film may affect strongly the CER response, small variations in the composition of the alloy or in its pre-treatment may have a large influence on the results. [86]

The results indicate that the modified bellows-driven single CDE arrangement gives reasonable results and can therefore be successfully used for measurements in a static autoclave, in which the pressure variations are

relatively low. According to the test of the pneumatically powered CER equipment the accuracy of electrode movement in air environment at room temperature was ± 0.1 μm. In BWR environment the measured accuracy of the electrode movement was better than ± 0.35 μm. The absolute accuracy could not be determined because of limitations of the LVDT sensor used for the calibration. The accuracy of the electrode movement needed for CER measurement in BWR environment is ± 0.1 μm.

Preliminary tests with pure nickel show that the system is capable of working in a BWR environment. The results obtained with the modified bellows-driven single CDE arrangement and with the step motor driven system are qualitatively and even quantitatively closely similar. For use in a BWR environment, the pneumatically powered servo-controlled CER equipment needs more development work, especially regarding the precise compensation of the pressure variation of the environment.

7.5 PSCINCORE-device design work

The primary goal was to develop and test a prototype incore (inside the test reactor core) tensile unit capable of performing axial tensile testing at room temperature. The study consists of the determination of the specimen fixing and alignment system and a demo tests at room temperature. The preliminary tests result has been compared to results from Riso National Laboratory in Denmark.

The load frame is designed to be symmetrical and it should be inflexible between the pneumatic loading unit and specimen fixing points. The free clearance between moving parts, i.e. the posts of the moveable specimen carrier along the alignment piece holes, should be around ± 0.01 mm after the manufacturing process. Table 3 shows the measured free clearances between the posts and alignment pieces. The idea for these measurements was to determine the free clearance between moving parts by using the starting and the ending position of the specimen carrier as shown in Figure 78.

Table 3. The measurements for the free clearance between moving parts of the load frame.

Load frame position	Free clearance at point A	Free clearance at point B
Starting point	±0.0030 mm	±0.0025 mm
Finishing point	±0.0050 mm	±0.0050 mm

According to the results in table 3 the free clearances for the moving parts were very small and the movement of the sliding parts was direct and sufficiently smooth.
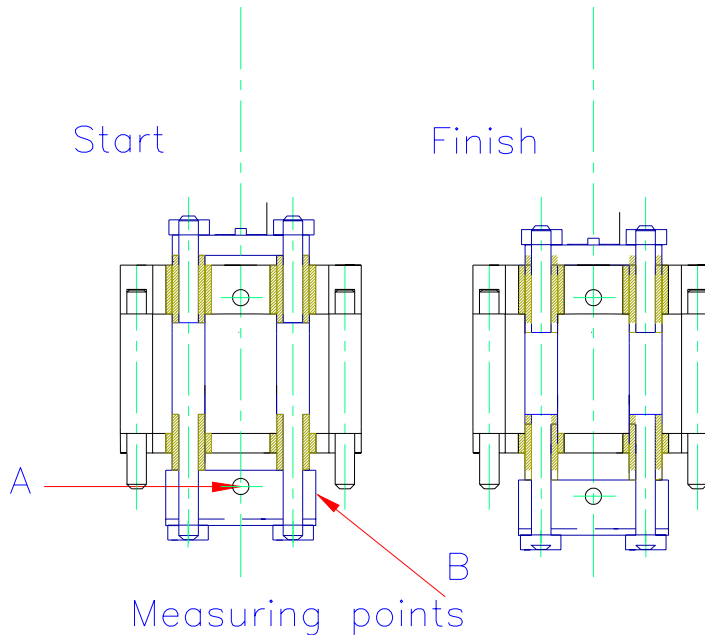
Figure 78. The measurement points for the free clearance of the moving load frame parts

The requirements for the specimen fixing system were as follows: good alignment for the specimen, no bending of the specimen during fixing and tightening processes, easy correct position of the specimen and easy use. The fixing system consists of fixing screws, carrier pins and fairing plates.

The idea to prevent the bending of the specimen during fixing and tightening processes is based on the functionality of the fairing plate. During the tightening

process of the fixing screw, the rotation range of the fairing plate is designed to be at a minimum i.e. the fairing plate can rotate only a few hundredth part of millimeter at the beginning of the fixing process. So, when the fairing plate is attached to the tensile specimen, it has only toward movement and therefore the rotating movement of the fixing screw can not affect the specimen. The right alignment for the specimen is performed by using a carrier pin which can go through the specimen and an alignment piece as shown in Figure 79.
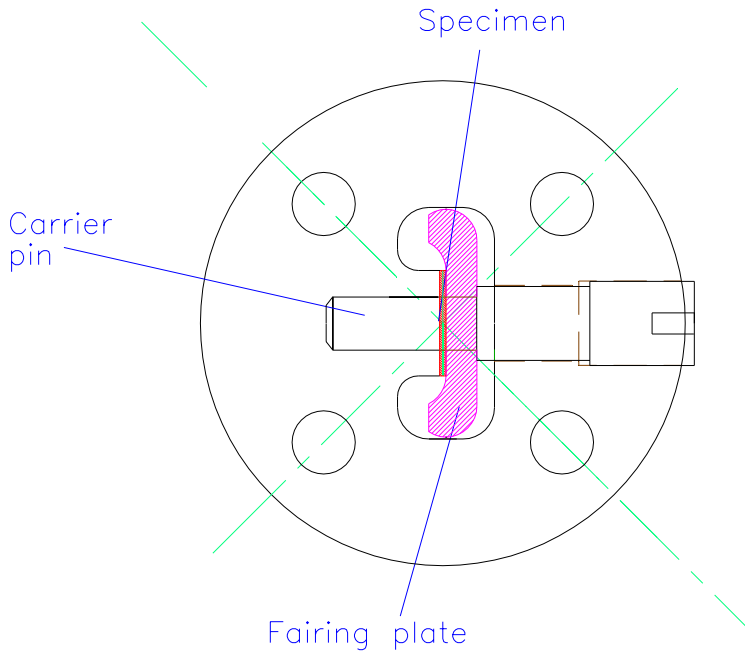
Figure 79. The tensile specimen fixing system.

The functionality of the specimen fixing system is checked by special tensile specimen with strain gauges. Two strain gages is fixed to the body of the tensile specimen using glue. According to these stain gauge measurements the bending rate of the tensile specimen was only 0.005 % during the fixing and tightening processes. According to ASTM standard, this value for bending is acceptable.

The main principle of the pneumatically powered loading unit is to provide the needed test load by using gas pressurized metal bellows. The gas is led inside the bellows from a servo-controlled pressure adjusting loop and using with the bellows inside pressure and the bellows effective cross section, the test load can

be calculated. The design and structure of the pneumatic loading unit is based on the bellows main dimensions as shown in Table 1. The pneumatic loading unit consists of a corrugated bellows, upper and lower pistons, a sleeve between pistons and a gas inlet tube as shown in Figure 37. The upper and lower pistons are moved over the sleeve when the pneumatic loading unit is pressurized. The three main diameters of the pneumatic loading unit are the outer diameter d_u, inner diameter d_i and the effective diameter d_e. The load calculations for load created with pneumatic loading unit are performed using the effective diameter d_e as shown above. The own stiffness and effective cross section of the pneumatic loading unit were selected from Table 1. The own stiffness was 268.8 N/mm and the effective cross section was 189 mm^2.

7.5.1 Typical tensile test results by using PSCINCORE device

The preliminary tensile tests were performed by PSCINCORE device at room temperature. The test materials were pure Cu, CuCrZr, CuAl25 and ferritic stainless steel. The test type was constant displacement rate test with strain rates $1.9*10^{-4}$ 1/s and $1.12*10^{-3}$ 1/s. The test temperature was 23 °C in air. Typical test results, stress as a function of strain are shown in Figure 80.
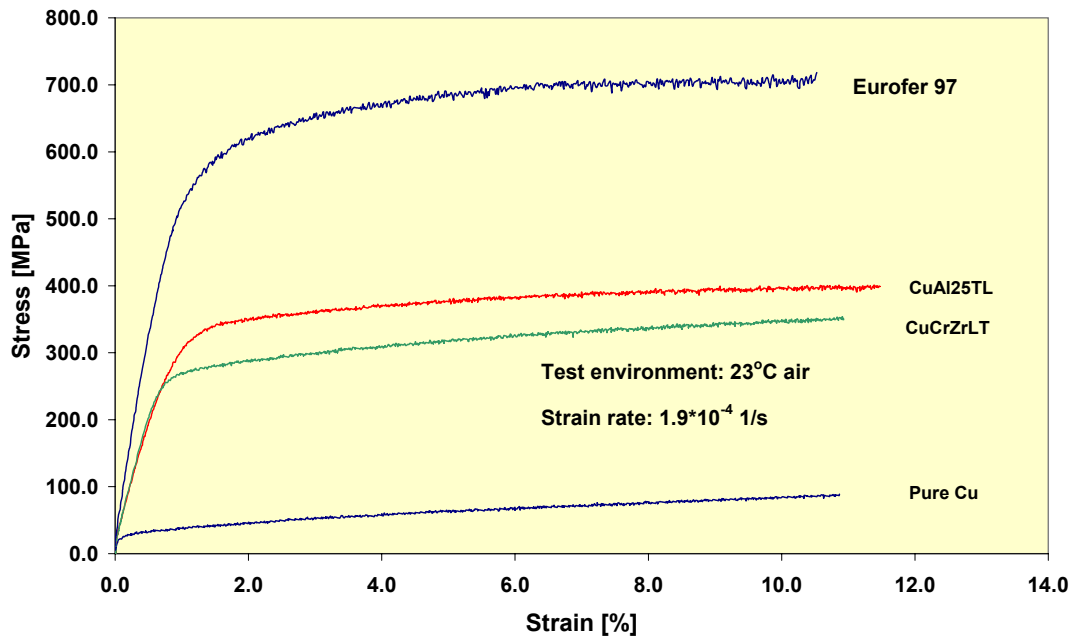
Figure 80. Strain and stress curves for different materials at room temperature.

According to the LVDT sensor, the maximum fluctuation in the displacement was < ±0.3 μm. According to ASTM 1152-87 standard the increase in the displacement has to be linear during a constant displacement rate (rising load) test and the fluctuation in the displacement can be at maximum ±3 μm at 0.3 mm of displacement and after that ±1 % of the total displacement. These requirements were achieved in the tests.

The test load presented above in every measured data points was determined by using formulas (45) and (46). According to ESIS P2 material testing standard, the load accuracy over the working range during the test should be ± 1% from measured value. According to Figure 81, these requirements were achieved in tests performed for copper alloys and for ferrite stainless steel. In the case of pure copper, the load deviation was more than ± 1 % from the measured value because of significantly lower required load levels during the tests.
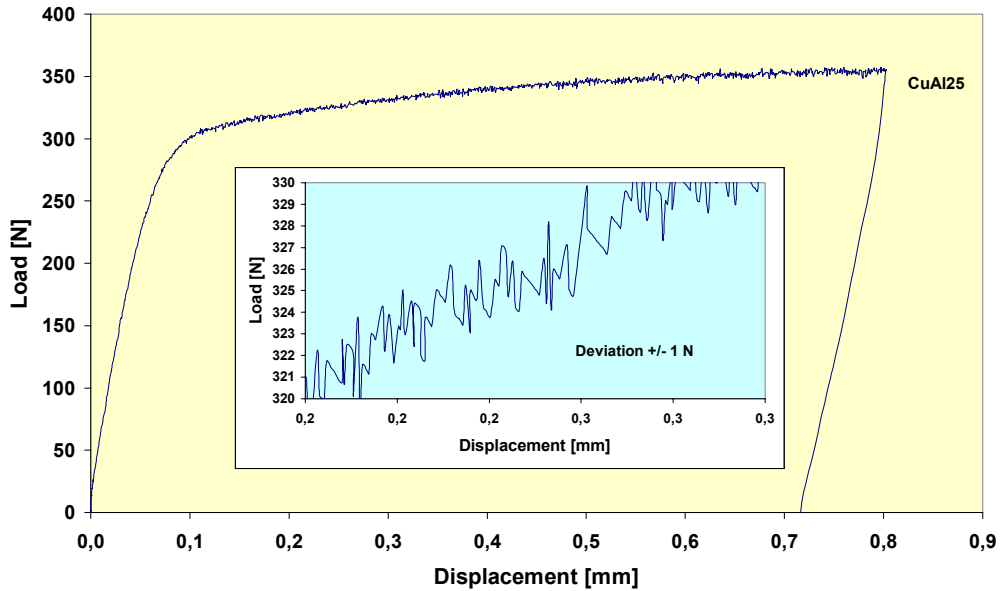
Figure 81. The load accuracy during the tensile test for CuCrZr specimen.

Stress strain curves for copper alloys performed at VTT and Riso laboratory in Denmark are compared in Figure 82. The loss of the true calibrations of the bellows own stiffness and the effective cross section values causes mainly the deviation between load levels. These values are selected from the bellows manufacturer book (table 1); according to the manufacturer, the accuracy for the bellows spring constant can be $\pm$ 20 % [73]. In the future, in addition to own stiffness calibration of the pneumatic loading unit, the calibration system should be capable of performing also calibration of the effective cross section of the pneumatic loading unit. [84]

Figure 82. Comparison between Riso and VTT results. [84]

8. In-reactor unaxial tensile test by using pure Cu specimens

The primary idea of this part was to build up and test a tensile testing system capable of performing tensile tests for small copper and copper alloy specimens inside the reactor core. The key requirements for the tensile testing system were the size of the load frame wi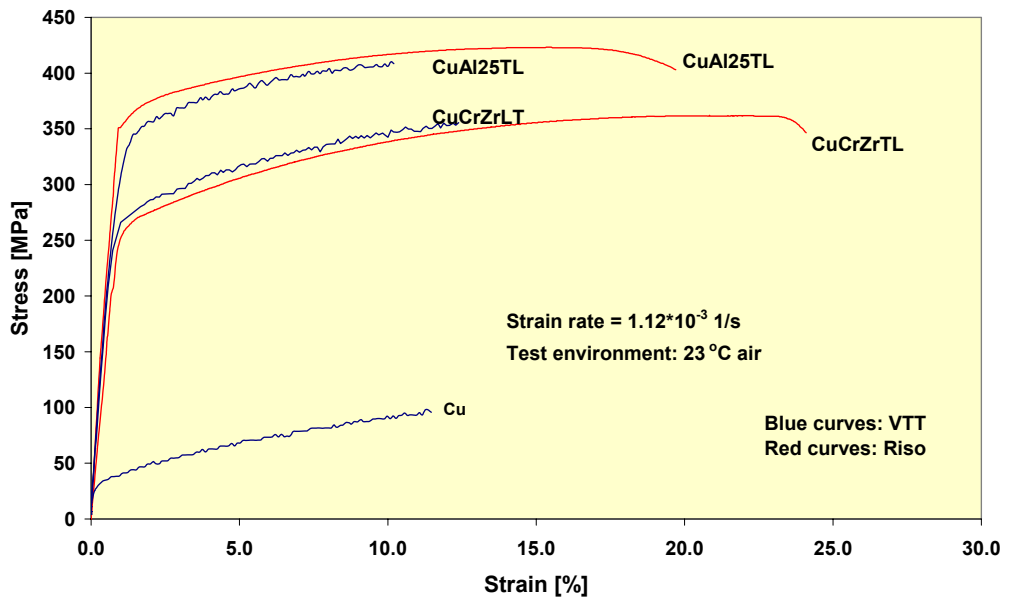th the pneumatic loading unit (bellows), the accuracy of the displacement (strain rate) and the accuracy of the load (pressure). [74]

A tensile testing system for a reactor environment requires thin and long pipe lines. The gas line between the pneumatic loading unit and pneumatic pressure adjusting loop should be at least 25 m. The maximum outer diameter for the pressure pipe was 1.6 mm. The maximum accepted diameter for the load frame was 25 mm. The pneumatic servo-controlled pressure adjusting loop with main part should be moveable. The reactor environment requires Helium instead air as a working gas for the pneumatic servo controlled testing system. The test load should be calculated from the inside pressure of the pneumatic loading unit, so a the specific calibration system was needed. The maximum inside pressure of the pneumatic loading unit should be between 50...70 bar. Instead of the prototypes 1 mm maximum displacement for the pneumatic loading unit, it was decided to use a maximum displacement of 1.4 mm. This should be enough to achieve the maximum load level during the tensile test inside the reactor. [76]

The operation principle of the tensile load frame was the same as for the prototype described above. Instead of a four post alignment system for the load frames moving parts, the reactor tensile system has been built up by using three posts as shown in Figure 83. This three post alignment system was needed because of reactor space limitations. The specimen fixing system was the same as in the prototype which is described above. The load frame with pneumatic loading unit and main parts is shown in Figure 84.
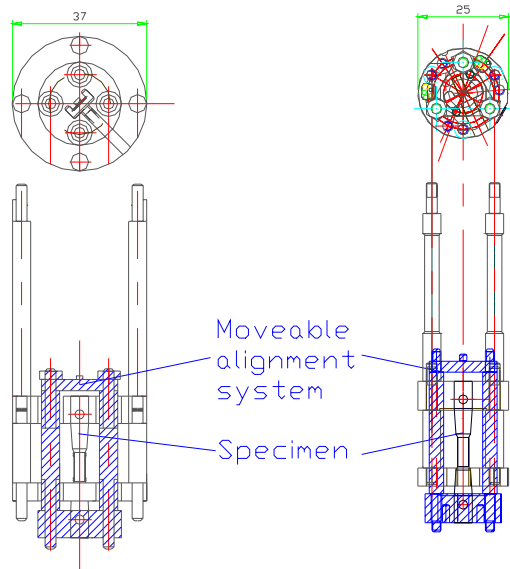
Figure 83. The structure of the load frames for the of prototype and the real reactor test device. [74]
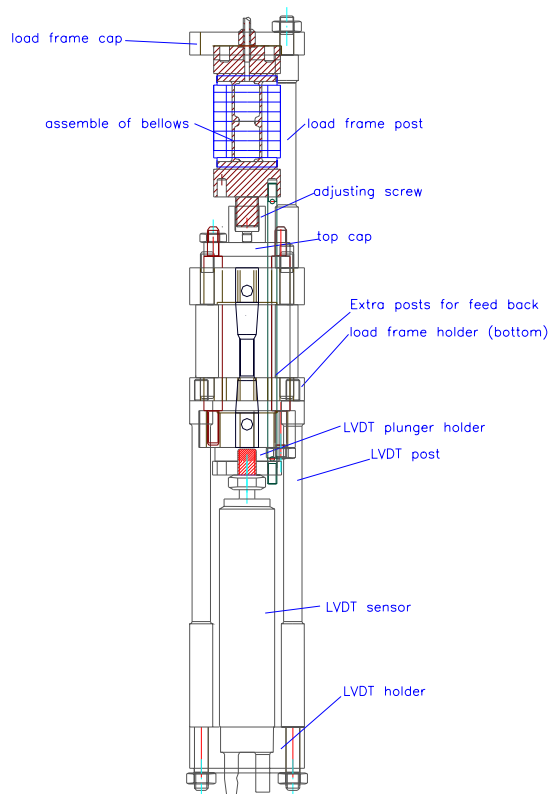
Figure 84. The load frame with main parts. [76]

8.1 Calibration of the pneumatic loading unit with load frame

The same moving parts of the load frame including pneumatic loading unit are needed in the calibration furnace as well as in a real test.

High temperature calibration of the measuring system was performed in a gas environment in the furnace shown in Figure 85. The load frame posts of the bellows was first moved to an other position and then installed into the calibration furnace. The calibration furnace consisted of the main frame, heating elements, an LVDT-sensor and a load sensor. A typical set of raw data from a load-pressure calibration run is shown in Figure 86. Based on this result and own stiffness measurement of pneumatic loading unit, an accurate calibration was achieved between the gas pressure and the load directed to the specimen by the bellows loading unit.
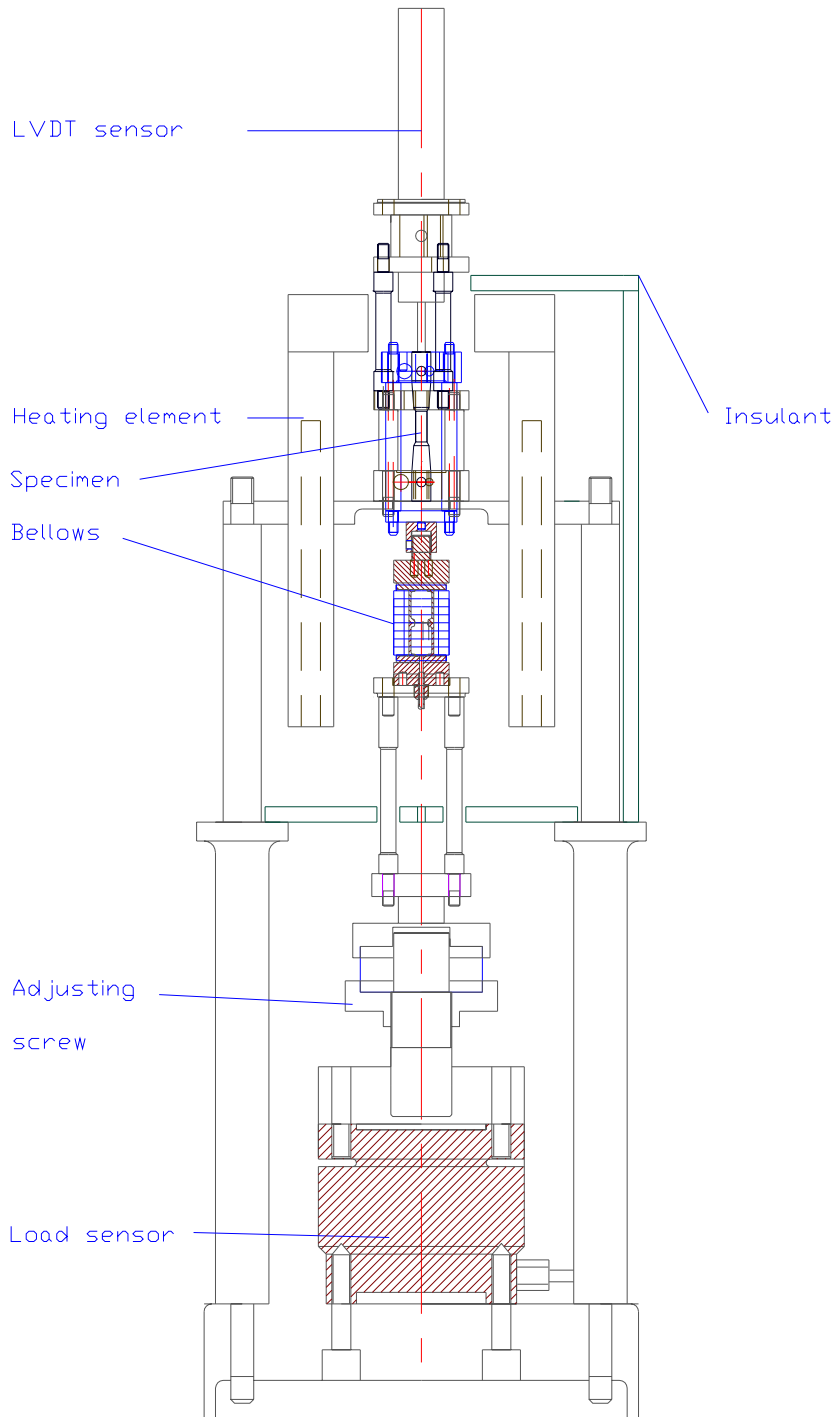
Figure 85. High temperature calibration system of the bellows.

The calibration procedure used consists of two different tests as described in section 2.3. The calibration results for the PSCINCORE pneumatic loading unit is presented in Figure 86 and 87. According to these results the own stiffness of the pneumatic loading unit was 4.6 bar/mm and the effective cross section was 106 mm^2.
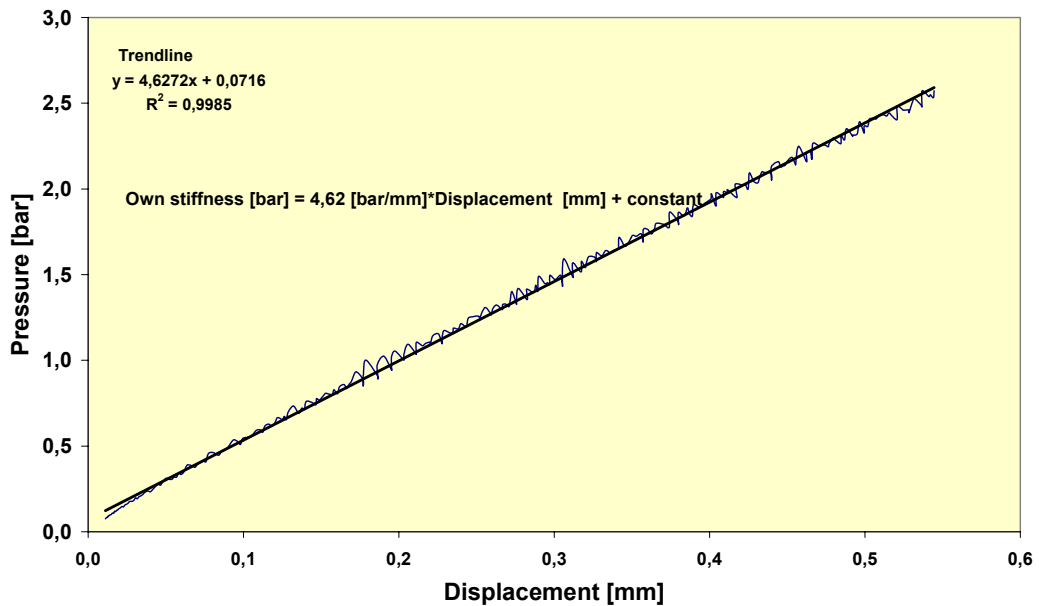
Figure 86. The own stiffness of the pneumatic loading unit.
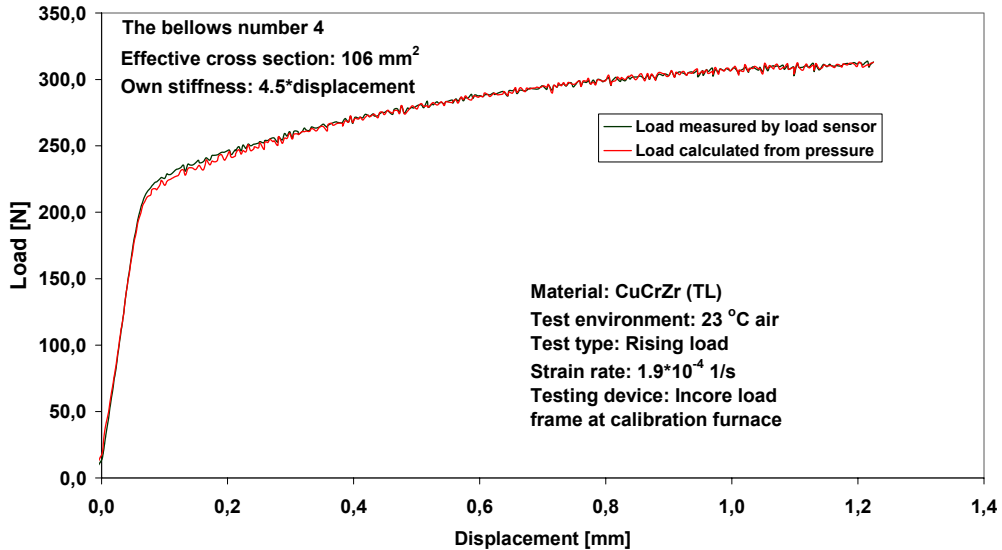
Figure 87. Calculated and measured load as a function of displacement.

As described above, the real load measured by the load sensor was 260.9 N and the calculated load was 261.2 N. The deviation of the calculated load compared to the load indicated by the load cell was 0.3 %. The accuracy of the load and pressure calibration over the tested range (0.1 to 1.3 mm of displacement) was approx. ±1 %. According to this data, the biggest deviation of the calculated load was at the beginning of the calibration curve. The main reason for this deviation is mostly mathematical but also caused by compliance in the beginning of the calibration as discussed earlier in chapter 6.4. The compliance of the calibration furnace and free clearance of the moving parts slightly affects the calibration results.

8.2 The reactor test setup

The reactor setup consists of the pneumatic loading units, pneumatic pressure adjusting loops, rigs and Helium bottles as shown in Figure 88. The distance between the servo-controlled pressure adjusting loop (cradle) and load frames was around 30 m. During the test, two load frames are used in the reactor core,

one load frame in the calibration furnace and one inside the pool water as a reference. [74]
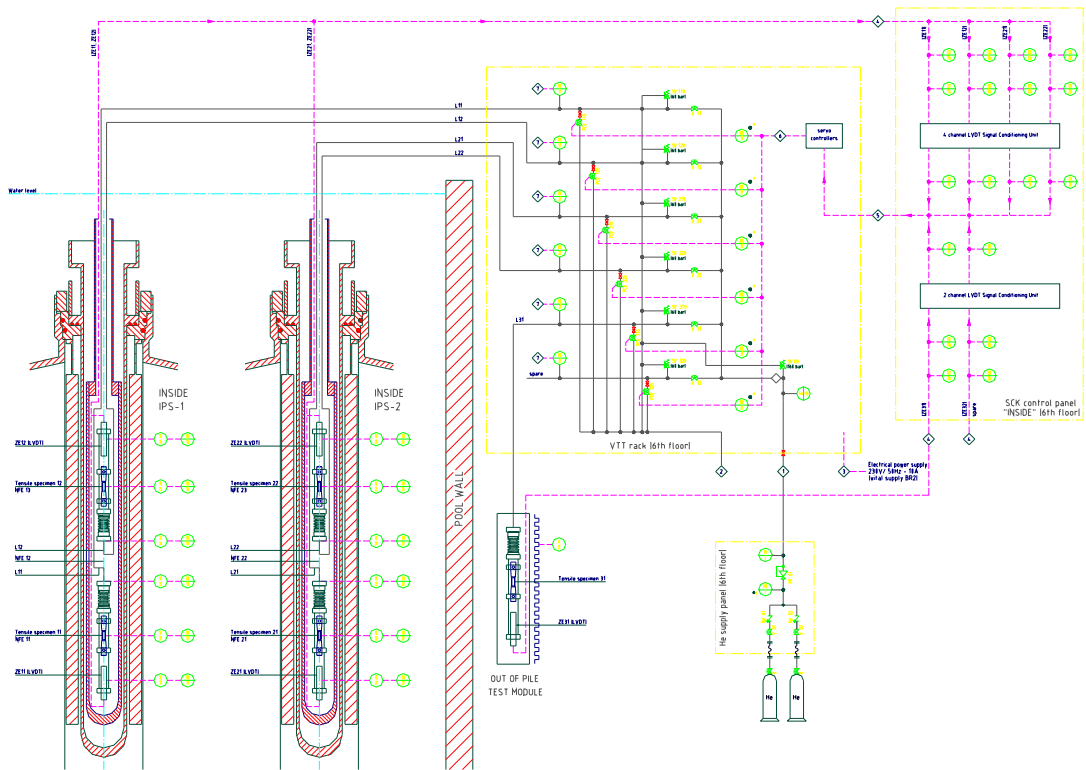
Figure 88. The reactor tensile testing setup.[76]

8.3 Results from reactor tests and discussion

For tests inside the reactor core the stress and strain curves for two pure Cu specimen was determined by using a pneumatically powered tensile testing system. The first test started immediately when the system was inside the reactor and the temperature increase caused by gamma heating was stabilized. The second test started 20 hours after the first one. The test type was a constant strain rate test with 10^{-7} 1/s strain rate. Irradiation time was around 320 hours. The stress as a function of irradiation time curve for Cu specimen is shown in Figure 89. The apparent load and strain noise consist of the electrical background noise of the LVDT sensor and the amplifier, gamma heating and fast neutron effects

which produce temperature variations of the LVDT sensor. The present work has demonstrated that it is technically feasible to carry out a well defined and controlled in-reactor dynamic tensile tests. This makes it possible to investigate the intrinsic role of the applied stress and the displacement damage acting concurrently in determining the global deformation behaviour of the material under dynamic irradiation conditions. [76]
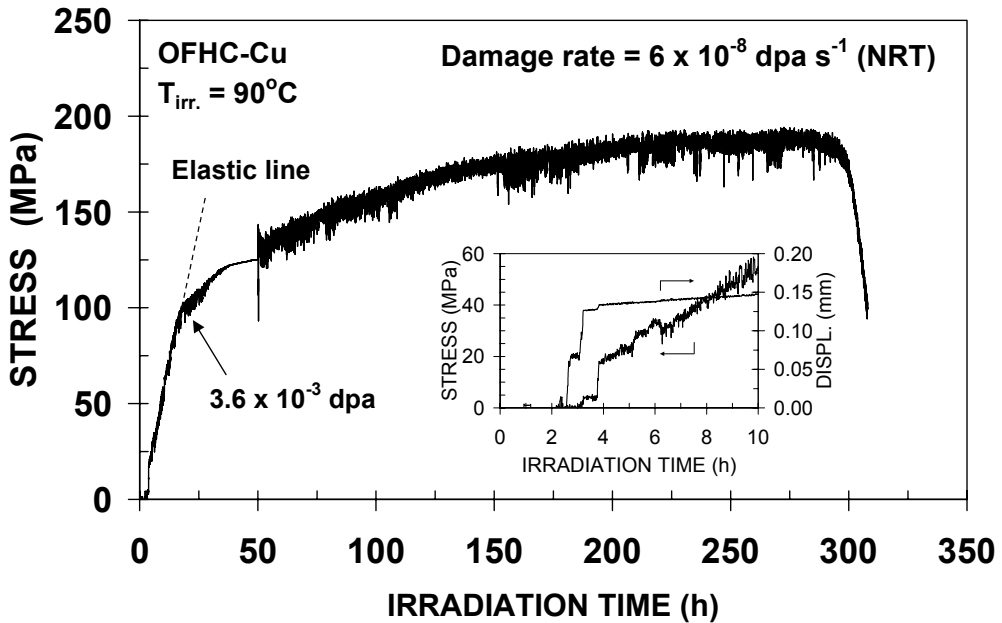
Figure 89. Stress as a function of irradiation time for pure Cu tensile specimen. [76]

The most significant feature of the present results is that during the dynamic in-reactor test, the material deforms uniformly and in a homogeneous fashion and does not show any sign of yield drop and plastic instability (i.e. low temperature embrittlement) as commonly demonstrated by the post-irradiation experiments. However, the fact that the material under the present irradiation and test conditions achieves an uniform elongation of only about 12% is still a matter of concern. This is particularly since it remains unknown as to what causes this reduction in the uniform elongation. Further investigations are necessary to determine and understand the factors responsible for the reduction in the uniform elongation. For the same pure copper tensile tested at 100°C in

the unirradiated condition yields, for example, an uniform elongation of about 56% was determined [5]. New experiments are being designed to address this issue. [76]

More detailed analysis of the in-reactor dynamic tensile test results and new experiments are in progress. [76]

9. Conclusions

The developed pneumatic loading technology provides important potential benefits and has already been successfully applied for many kind of materials testing in different test environments. A pneumatic servo-controlled material testing system was used to perform fracture mechanic-, corrosion fatigue-, tensile,- and electrochemical measurements in gas, high temperature aqueous and irradiation environments. The greatest advantages of this new testing system are sensitivity and possibilities to perform material testing inside the reactor core. Furthermore the system can be made compact so that several testing systems can be fitted simultaneously in one test chamber. Thus the total cost of testing is decreased and the reliability of the test result is considerably increased.

Over the past 9 years, VTT has used the pneumatic testing system to increase the knowledge of factors affecting material properties in gas and aqueous coolants at high temperatures. In this thesis, the workability and usability of the pneumatic material testing system with four applications was proven. The PSCFM device worked with high accuracy of displacement and load during the many fracture mechanics tests in BWR environments. The load and displacement accuracy was ± 1 % of the measured value and they satisfied ASTM and ESIS conditions. In addition, the crack growth rate of Inconel 182 weld metal as a function of sulphate content (10, 20, 30 ppb) of BWR coolant was performed. These results show that the crack growth rate of Inconel 182 weld material is strongly affected by the suphate content of BWR coolant.

The prototypes of fatigue (PSCFAT-device), controlled distance electrode (PSCCDE-device) and tensile (PSCINCORE-device) devices have been designed and tested. The units were based on proven technology and operated well and gave reliable test results about the specific material properties. The load frame unit of the PSCFAT-device was able to maintain alignment of the specimen almost as would be required of conventional materials testing load frames. The degree of bending was 11% which qualifies as a class 20 alignment, but the bending was primarily static and the dynamic component was only 2%. This degree or alignment is well suitable for LCF and HCF testing of ductile materials, such as stainless steels. The strain controlled fatigue test operated without difficulty for two days and 15600 fatigue cycles. The specimen failed in its midsection by fatigue. Results from the strain controlled fatigue test were in

good agreement with data from VTT and other laboratories generated using more conventional test systems.

The main parts and the operation principle of a pneumatically powered PSCCDE-device have also been presented. The equipment was tested in air at room temperature and under typical BWR environments. The test material was pure nickel and its oxide film properties were tested in a BWR environment as a function of potential. According to the test of the pneumatically powered CDE equipment, the accuracy of electrode movement in air environment at room temperature was ± 0.1 μm. In a BWR environment the measured accuracy of the electrode movement was better than ± 0.35 μm. The absolute accuracy could not be determined because of limitations of the LVDT sensor used for the calibration. For CDE measurements the needed accuracy of the electrode movement in BWR environment is ± 0.1 μm. For use in a BWR environment the pneumatically powered servo-controlled CDE equipment needs more development work especially for the precise compensation of the pressure variation of the environment. The modified servo-pneumatic bellows-driven single CDE arrangement has been verified to enable measurements in a static autoclave up to 250 ^{o}C. Based on the calibration of the system and on the known magnitude of the pressure variation of the bulk environment under loop conditions ($\pm$0.03 MPa) one may conclude that the current design enables similar measurements also under loop conditions. Also, further tests up to the temperature of 300 ^{o}C have to be performed. If needed, an additional improvement can be obtained by applying displacement feedback control instead of the pressure feedback control currently applied. The displacement feedback control makes it possible to compensate for pressure variations in the environment.

The present work of PSCINCORE has demonstrated that it is technically feasible to carry out well defined and controlled in-reactor dynamic tensile tests. This makes it possible to investigate the intrinsic role of the applied stress and the displacement damage acting concurrently in determining the global deformation behaviour of the material under dynamic irradiation conditions. The PSCINCORE device was used to determine stress and strain curves for pure Cu specimen in the BR-2 reactor at Belgium. The reactor pool water temperature was 90 °C, neutron flux ~$0.3*10^{14}$ n cm^{-2}s^{-1}s (E>1 MeV) and damage rate ~$2*10^{-4}$ h^{-1}. The test type was constant displacement rate test with strain rate ~10^{-7} 1/s.

The most significant feature of the present results is that during the dynamic in-reactor test, the material deforms uniformly and in a homogeneous fashion and does not show any sign of yield drop and plastic instability (i.e. low temperature embrittlement) as commonly demonstrated by the post-irradiation experiments. However, the fact that the material under the present irradiation and test conditions achieves an uniform elongation of only about 12% is still a matter of concern. This is particularly since it remains unknown as to what causes this reduction in the uniform elongation. Further investigations are necessary to determine and understand the factors responsible for the reduction in the uniform elongation due to irradiation. The same pure copper tensile tested at 100^oC in the unirradiated condition yields, for example, an uniform elongation of about 56% [74]. New experiments are being designed to address this issue.

References

1. Anderson, T. L., "Fracture Mechanics, Fundamentals and Applications." Second Edition, Department of Mechanical Engineering, Texas A&M University, College Station, Texas, CRX, 1995. Pp. 19–179.

2. Griffith, A.A., "The phenomena of Rupture and Flow in Solids." Philosophical Transactions, Series A, Vol. 221, 1920, pp. 163–198.

3. Irwin, G. R., "Onset of Fast Crack Propagation in High Strength Steel and Aluminum Alloys." Sagamore Research Conference Proceedings, Vol. 2, 1956, pp. 289–305.

4. Westergaard, H.M., "Bearing Pressures and Cracks." Journal of Applied Mechanics, Vol. 6, 1939, pp. 49–53.

5. Irwin, G.R., "Analysis of Stresses and Strains near the End of a Crack Traversing a Plate." Journal of Applied Mechanics, Vol. 24, 1957, pp. 361–364.

6. Sneddon, I.N., "The distribution of Stress in the Neighbourhood of a Crack in an Elastic Solid." Proceedings, Royal Society of London, Vol. A-187, 1946, pp. 229–260.

7. Williams, M.L., "On the Stress Distribution at the Base of a Stationary Crack." Journal of Applied Mechanics, 1957, pp. 109–114.

8. Wells, A.A., "Unstable Crack Propagation in Metals: Cleavage and Fast Fracture." Proceedings of the Crack Propagation Symposium, Vol. 1, Paper 84, Cranfield, UK.

9. Rice, J.R., "A Path Independent Integral and the Approximate Analysis of Strain Concentration by Notches and Cracks." Journal of Applied Mechanics, Vol. 35, 1968, pp. 379–386.

10. Hutchinson, J.W., "Singular Behavior at the End of a Tensile Crack Tip in a Hardening Material." Journal of the Mechanics and Physics of Solids, Vol. 16. 1968, pp. 13–31.

11. Rice, J.R. and Rosengren, C.F., "Plane Strain Deformation near a Crack Tip in a Power-Law Hardening Material." Journal of Mechanics and Physics of Solids, Vol. 16, 1968, pp 1–12.

12. ASTM E 1152-87, "Standard test method for determining J-R curves." ASTM, Annual Book of Standars, Vol 03.01, 1993, pp. 814–824.

13. Metals Handbook, Desk Edition (Second Edition), ASM International, Materials Park, 1998.

14. Sedriks, J. and Houston, A., "Corrosion testing made easy ." Stress corrosion cracking test methods. TX : NACE, vol. 1, 1990, pp. 87.

15. McClintock, F.A., "Plasticity Aspects of Fracture." Fracture: An Advanced Treatise, Vol. 3 Academic Press, New York, 1971, pp. 47–225.

16. Hertzberg, R.W., "Deformation and fracture mechanics of engineering materials." Third edition. New York, U.S.A, John Wiley & Sons, 1989, pp. 29–45 and 271–321.

17. Suresh, S., "Fatigue of Materials.", ., Cambridge Uniersity Press, 2. ed, 1998, pp. 30–33 and 40–45.

18. Paris, P.C., Gomez, M.P., and Anderson, W.P., "A Rational Analytic Theory of Fatique." The Trend in Engineering, Vol. 13, 1961, pp. 9–14.

19. Paris, P.C., and Erdogan, F., "A Critical Analysis of Crack Propagation Laws." Journal of Basic Engineerings, Vol. 85, 1960, pp. 528–534.

20. Brossia, C.S. & Kelly, R.G., "Occluded solution chemistry control and the role of alloy sulfur on the initiation of crevice corrosion in type 304 SS." Corrosion Science 40 (1998), pp. 1851–1871.

21. Page, R.A, McMinn, A. & Hudak, S.J. Jr., "Characterisation of crack tip electrochemistry using a simulated crack. Corrosion." 44 (1988), pp. 623–631.

22. P. Aaltonen, M. Bojinov, M. Helin, P. Kinnunen, T. Laitinen, E. Muttilainen, K. Mäkelä, A. Reinvall, T. Saario and A. Toivonen, "Facts and views on the role of anionic impurities, crack tip chemistry and oxide films in environmentally assisted cracking." Espoo, VTT Industrial Systems, 2002. 68 p. + app. 21 p. VTT Tiedotteita - Research Notes 2148.

23. R. Gilmont and L. I. Wechsler, American Laboraty, June 1986, pp. 70–82.

24. "High temperature, high pressure electrochemistry in aqueous solutions." Nace publications NACE-4, 1976, USA, pp. 265.

25. Bard, A.J. and Faulkner, L.R., "Electrochemical Methods, Fundamentals and Applications, John Wiley&Sons." USA 1980, pp. 718.

26. Chai, G., Lidar, P. and Molander, A., "The corrosion potential and the crack growth rate for stainless steel in BWRs under normal water chemistry." Swedish Nuclear Power Inspectorate, SKI, Stockholm, 1995, SKI Report 95:74.

27. Turnbull, A., "Crack-tip electrochemistry: recent developments." In: R.M. Latanision & R.H. Jones (eds), Chemistry and Physics of Fracture, NATO ASI Series E: Applied Sciences – No. 130, Martinus Nijhoff Publishers, Dordrecht 1987. Pp. 287–310.

28. Aromaa, J., "Materiaalien sähkökemia." TKK, Espoo, 2000, pp. 122 . [In Finnish]

29. Angeliu, T.M., Andresen, P.L. and Ford, F.P., "Applying slip-oxidation to the SCC of austenitic materials in BWR/PWR environments." In CORROSION'98, NACE International, 1998, Paper No. 262.

30. Andresen, P.L., "SCC growth rate behaviour in BWR water of increased purity.", Proceedings of the Eight International Symposium on Environmental Degradation of Materials in Nuclear Power Systems – Water Reactors, August 10–14, 1997, Amelia Island, Florida, USA, Vol. 2. Pp. 675–684.

31. Hermansson, H-P. and Gott, K., "Mechanism for the effect of sulphate on SCC in BWRs." Proceedings of the Eighth International Symposium on Environmental Degradation of Materials in Nuclear Power Systems – Water Reactors, August 10–14, 1997, Amelia Island, Florida, USA, Vol. 1. Pp. 567–673.

32. Davis, R.B. and Indig, M.E., "The effect of aqueous impurities on the stress corrosion cracking of austenitic stainless steel in high temperature water." Corrosion, April 18–22, 1983, Anaheim, California, USA, Paper number 128, pp. 25.

33. Ruther, W.E., Soppet, W.K. and Kassner, T.F., "Effect of temperature and ionic impurities at very low concentrations on stress corrosion cracking of type 304 stainless steel." Corrosion 44 (1988), pp. 791–799.

34. Ljungberg, L., Renström, K., Cubicciotti, D. and Trolle, M., "Effects of water impurities on environmental cracking in BWRs." Proceedings of the Second International Symposium on Environmental Degradation of

Materials in Nuclear Power Systems – Water Reactors. American Nuclear Society, La Grange Park, Illinois, 1986. Pp. 435–441.

35. Ljungberg, L., Cubicciotti, D. and Trolle, M. "Effects of impurities on the IGSCC of stainless steel in high-temperature water." Corrosion 44 (1988), pp. 66–72.

36. Ljungberg, L., Cubicciotti, D. and Trolle, M. "Effects of some seldom noticed water impurities on stress corrosion cracking of BWR construction materials." Corrosion 45 (1989), pp. 215–222.

37. Sambongi, M., Takamori, K., Suzuki, S., Ichikawa, N., Itow, M., Tsuchiya, Y., Kato, T., Wada, Y., Akamine, K., Takahashi, T. and Nakayama, G., "Effect of reactor water impurities on ECP and SCC." Proceedings of Water Chemistry '98, The 1998 JAIF International Conference on Water Chemistry in Nuclear Power Plants, October 13–16, 1998, Kashiwazaki, Japan. Pp. 343–348.

38. Toivonen, A., Aaltonen, P., Taivalaho, L., Moilanen, P. and Muttilainen, E. "Effects of water chemistry transients on crack growth rate of nickel-based weld metals." 10th International Conference on Environmental Degradation of Materials in Nuclear Power Systems – Water Reactors. Lake Tahoe, NV, USA, 5.–9. August 2001. Pp. 9.

39. Smallman, R.E., "Modern Physical Metallurgy and Materials Engineering." 6th ed., Butterworths, 1999, pp. 87–89.

40. Andresen, P.L., "SCC growth rate behaviour in BWR water of increased purity." Proceedings of the Eight International Symposium on Environmental Degradation of Materials in Nuclear Power Systems – Water Reactors, August 10–14, 1997, Amelia Island, Florida, USA, Vol. 2. Pp. 675–684.

41. Andresen, P.L., "A mechanism for the effects of ionic impurities on SCC of austenitic iron and nickel base alloys in high temperature water." Corrosion 85, Paper number 101, March 25–29, 1985, Boston, Massachusetts, USA.

42. Turnbull, A., "Modelling of crack chemistry in sensitized stainless steel in boiling water reactor environments." Corrosion Science 39 (1997), pp. 789–805.

43. Li, R. and Ferreira, M.G.S., "The thermodynamic conditions for hydrogen generation inside a stress corrosion crack." Corrosion Science 38 (1996), pp. 317–327.

44. Lagerström, J., Ehrnstén, U., Saario, T., Laitinen, T. and Hänninen, H., "Model for environmentally assisted cracking of Alloy 600 in PWR primary water." Proceedings of the Eight International Symposium on Environmental Degradation of Materials in Nuclear Power Systems – Water Reactors, August 10–14, 1997, Amelia Island, Florida, USA, Vol. 1. Pp. 349–356.

45. Turnbull, A., "Modeling of the chemistry and electrochemistry in cracks – a review." Corrosion 57 (2001), pp. 175–188.

46. Andresen, P.L. and Young, L.M., "Crack tip microsampling and growth rate measurements in low-alloy steel in high-temperature water", Corrosion 51 (1995), pp. 223–233.

47. Andresen, P.L., "Advanced techniques for characterisation of electrochemical effects in stress corrosion cracking." In: Russell, H.J. and Baer, D.R. (eds). New techniques for characterizing corrosion and stress corrosion, Proceedings of a symposium sponsored by the Corrosion and Environmental Effects Committee of the Structural Materials Division (SMD) of TMS. Cleveland, Ohio, USA, October 29–November 2 1995. Pp. 193–215.

48. Hänninen, H., Illi, H., Törrönen, K. and Vulli, M., "On the electrochemical and chemical conditions in corrosion fatigue cracks of low alloy steels in high temperature water." In: Cullen, W.H. (ed.). Proceedings of the Second International Atomic Energy Agency Specialists' Meeting on Subcritical Crack Growth, Sessions III and IV, Sendai, Japan, May 15–17 1985. Pp. 179–199.

49. Taylor, D.F. and Silverman, M., "The effect of hydrogen evolution on acidification in alloy 600 and 304 stainless steel crevices at 288 °C." Corrosion 36 (1980), pp. 544–549.

50. Nystrom, E.A., Lee, J.B., Sagüés, A.A. & Pickering, H.W., "An approach for estimating anodic current distributions in crevice corrosion from potential measurements." J. Electrochem. Soc. 141 (1994), pp. 358–361.

51. Taylor, D.F., "Crevice corrosion of Alloy 600 in high-temperature aqueous environments." Corrosion 35 (1979), pp. 550–559.

52. Taylor, D.F. and Caramihas, C.A., "Crevice corrosion in high-temperature aqueous systems, Potential/pH measurements in alloy 600 crevices at 288 °C." J. Electrochem. Soc. 129 (1982), pp. 2458–2464.

53. Taylor, D.F. and Caramihas-Foust, C.A., "Cooling kinetics: Evidence for a hydrogen countercell in 304L stainless steel crevices at high temperatures." J. Electrochem. Soc. 132 (1985), pp. 1811–1814.

54. Charles, E.A., Congleton, J. and Parkins, R.N., "Various electrochemical measurements in a simulated corrosion fatigue crack." Corrosion 44 (1988), pp. 599–605.

55. Gabetta, G. and Caretta, E., "Electrochemical potential measurements inside and outside a growing crack during environmental fatigue tests at 288 °C, with different oxygen contents." Corrosion chemistry within pits, crevices and cracks, 1.–3. October 1984, Teddington, UK.

56. Lee, Y.H., Takehara, Z. and Yoshizawa, S., "The enrichment of hydrogen and chloride ions in the crevice corrosion of steels." Corrosion Science 21 (1981), pp. 391–397.

57. Turnbull, A. and Thomas, J.G.N., "A model of crack electrochemistry for steels in the active state based on mass transport by diffusion and ion migration." J. Electrochem. Soc. 129 (1982), pp. 1412–1422.

58. Li, D. and Huang, Z., "A model of the electrochemical behaviour within a stress corrosion crack." J. Appl. Electrochem. 22 (1993), pp. 1310–1316.

59. Sharland, S.M., "A mathematical model of the initiation of crevice corrosion in metals." Corrosion Science 33 (2) 1992, pp. 183–201.

60. Simonen, E.P., Jones, R.H. and Windisch, C.F. Jr., "A transport model for characterizing crack tip chemistry and mechanics during stress corrosion cracking." In: Russell, H.J. and Baer, D.R. (eds). New techniques for characterizing corrosion and stress corrosion. Proceedings of a symposium sponsored by the Corrosion and Environmental Effects Committee of the Structural Materials Division (SMD) of TMS, Cleveland, Ohio, USA, October 29–November 2, 1995. Pp. 141–160.

61. Aaltonen, P., Bojinov, M., Helin H., Kinnunen, P., Laitinen, T., Muttilainen, E,. Mäkelä, K., Reinvall, A., Saario, T. and Toivonen, A., "Facts and views on the role of anionic impurities, crack tip chemistry and oxide films in environmentally assisted cracking." Espoo, VTT Industrial Systems, 2002. 68 p. + app. 21 p. VTT Tiedotteita - Research Notes 2148.

62. Ateya, B.G. and Pickering, H.W., "The distribution of anodic and cathodic reaction sites during environmentally assisted cracking." Corrosion Science 37 (1995), pp. 1443–1453.

63. Korroosiokäsikirja, Suomen Korroosioyhdistys SKY, 1988, pp. 966.

64. Fontana, Corrosion Engineering and Applications, McGraw-Hill Science/Engineering/Math; 3rd edition (November 1, 1985), pp. 512.

65. Marcus P. and Oudar J., (eds.) Corrosion Mechanisms in theory and practice. Marcel Dekker, New York 1995, pp. 201–372.

66. Laitinen, T. et al., "The properties of and transport phenomena in oxide films on iron, nickel, chromium and their alloys in aqueous environments." Säteilyturvakeskus, Report STUK-YTO-TR150, Edita, Helsinki 1999, 79 s.

67. Macdonald, and Hettiarachchi, S.J., Electrochem. Soc., 131 (1984), Pp. 2206.

68. Kinnunen. P., "Electrochemical characterisation and modeling of passive films on NI- and Fe-based alloys." VTT Publications 427, 2002, appendix 1.

69. Chanfreau, E., Saario, T., Aaltonen, P., Törrönen, K., "Autoclave facility for materials testing and sensor development in simulated process environments." Espoo, Valtion teknillinen tutkimuskeskus, Tiedotteita, 1987, 812. 54 s.

70. SFS standard 2289., "Takaisinkytketty säätöjärjestelmä.", 21 s.

71. Moilanen. P., Arilahti. E. and Varis. E., "Pneumaattinen säätö" Finnish patent number: 107646.

72. Moog programmable servo control manual, Moog controls limited, Users manual, 2000, pp. 234.

73. Hydra Metal bellows catalog, Witzenmann, 2002, pp. 280

74. Saario T. and Piippo J., "A new electrochemical technique for in situ measurement of electric resistance and semiconductor characteristics of surface films on metals." Materials Sci. Forum 1995;185–188, 621–627.

75. Marquis. G., Moilanen. P., Solin. J. and Aaltonen. P., "A Novel Unit for Testing in Autoclave." Report VALC-611. 1999. Pp. 21.

76. Singh. B.N., Tähtinen. S., Moilanen. P., Jacquet. P. and Dekeyser. J. "In-reactor uniaxial tensile testing of pure Copper at 90°C., Journal Nuclear Materials, 2003. Pp. 12.

77. ESIS P2-P (1992), "ESIS procedure for determining the fracture behaviour of materials." European Stuctural Integrity Society, Delft, The Netherlands, pp. 1289–1297.

78. Toivonen A., "Stress corrosion testing of metals - applications of small pre cracked bend specimens.", Licentiate seminar. HUT. 2002. Pp. 14.

79. Toivonen, A., Moilanen P., Pyykkönen M., Tähtinen S., Rintamaa R. and Saario, T., "The feasibility of small size specimens for testing of environmentally assisted cracking of irradiated and materials under irradiation in reactor core." Nuclear Engineering and Design 193, 1999, pp. 309–316. (PSCFM device)

80. SKIFS 1994:1, "Statens kärnkraftsinspektions föreskrifter om mekaniska anordningar i kärntekniska anläggningar." SKI, 1994.

81. Morin, U., Jansson, C. and Bengtsson, B., "Crack Growth Rates for Ni-base Alloys with the Application to an Operating BWR." 6th International Symposium on Environmental Degradation of Materials in Nuclear Power Systems-Water Reactors, August 1-5, 1993, San Diego, California. Pp. 373–377.

82. Marquis, G. and Solin, J., "Spectrum fatigue testing using dedicated software." Automation in Fatigue and Fracture: Testing and Analysis, ASTM STP 1231, C. Amzallag, Ed., American Society for Testing and Materials, Philadelphia, 1994. Pp. 241–256.

83. Chopra, O.K. and Gavenda, D.J., "Effects of LWR coolant environments on fatigue lives of austenitic stainless steels." PVP - Vol. 353, Pressure Vessels and Piping Codes and Standards, ASME, 1997, Pp. 87–97.

84. Tähtinen, S., Pyykkönen M., Singh B.N and Toft P., "Effect of neutron irradiation on tensile and fracture toughness properties of copper alloys and their joints with stainless steel." Effects of radiation and Materials, 19th International Symposiuom, STP 1366, American Society for Testing and Materials, West Conshohocken, PA (2000), pp. 1241–1259.

85. Moilanen, P., Arilahti, E., Bojinov, M., Laitinen, T., Mäkelä, K., Mäkelä, M., Mäkinen, R., Saario, T., Sirkiä, P. and Toivonen, A., "Pneumatic servo-controlled fracture resistance measuring device (PSFM-Device) and contact electric resistance measuring device (CER Device)." Enlarged Halden Programme Group Meeting, Loen, NO, 24 – 29 May 1999 (1999), 16 p.

86. Bojinov, M., Kinnunen, P., Laitinen, T., Moilanen, P., Mäkelä, K. and Saario, T., "Further testing of the bellows driven controlled-distance electrochemistry arrangenment.", Research report BVAL67-011187, Espoo, 2001, pp. 11.

87. Solin, J., Karjalainen-Roikonen, P., Moilanen, P. and Marquis, G,. " Fatigue testing in reactor environments for quontitative plant life management.", 2nd International Conference on Fatigue of Reactor Components. Snowbird, UT, 29–31 July 2002. EPRI OECD USNRC (2002), pp.16.

88. Brummer, S.M., Simonen, E.P., Scott, P.M., Andresen, P.L., Was, G.S. and Nelson, J.L., "Radiation-induced Material Changes and Susceptibility to Intergranular Failure of Light-Water-Reactor Core Internals". Journal of Nuclear Materials, 274, 1999. Pp. 300–314.

Author(s)
Moilanen, Pekka

Title
Pneumatic servo-controlled material testing device capable of operating at high temperature water and irradiation conditions

Abstract

Special requirements set for the constructional materials used in energy production have strongly influenced the challenges in the component design work. Many material parameters such as corrosion, fracture mechanics, fatigue and oxide films are needed as input data for such work. The generation of reliable data calls also for more sophisticated testing systems. The newly developed pneumatic loading technology (patented in Finland and international patents pending) provides important potential benefits and has already been successfully applied to testing many kinds of materials in different test environments. As the moving parts that penetrate the pressure boundary are not needed, the friction force at the sealing element location is avoided. Therefore the load control with pneumatic loading unit is more accurate than with the conventional servo-hydraulic devices. This enables testing of small size samples which is an advantage e.g. when testing irradiated materials or testing materials inside the reactor core of a nuclear power plant and especially in determining environmentally assisted crack growth rates of structural materials. Furthermore, the new design enables simultaneous testing of several samples, which helps produce more reliable statistical data in a more economical way.

This thesis summarizes my work done at the Technical Research Centre of Finland over the past 9 years to increase the knowledge of factors affecting material testing devices and material properties in gas and aqueous coolants at high temperatures. The developed pneumatic servo-controlled material testing device has been used to perform crack growth rate tests as a function of stress intensity factor K for AISI 316 stainless steel and Inconel 182 weld metal in Boiling Water Reactor (BWR) coolant by using small size (10x10x55 mm) three point bending specimens. The load and displacement were controlled during these tests by the pneumatic servo-controlled fracture measuring device (PSCFM device) and based on test results crack growth rates for Inconel weld metal and AISI 316 have been calculated. During the tests, accuracy with very slow constant displacement rates of $1.2 \ 10^{-5}$ mm/min and $1.2 \ 10^{-6}$ mm/min and long term stability of the pneumatic material testing system under high temperature water environment, has been verified. Furthermore, the crack growth rate for Inconel 182 weld metal as a function of sulphate content (10, 20, 30 ppb) of BWR coolant has been determined. These results shows that the crack growth rate of Inconel 182 weld material is strongly affected by the sulphate content of BWR coolant. Furthermore, prototypes of pneumatically powered fatigue (PSCFAT-device), controlled distance electrode (PSCCDE-device) and tensile (PSCINCORE-device) devices have been designed and tested. The units, which were based on proven technology, operated well and gave reliable test results for the material design parameters. The PSCFAT device was tested at room temperature and the degree of specimen bending and general system performance were measured. A strain controlled axial fatigue test in a 12 MPa autoclave at $100 °C$ was also performed. The test material was AISI 316 stainless steel and the specimen failed in its midsection due to fatigue after 15600 cycles. The preliminary tests with pneumatically powered controlled distance electrode arrangement equipment (PSCCDE) is presented. The equipment was tested in air at room temperature and in typical BWR environments. The test material was pure nickel and its oxide film properties were tested in BWR environment as a function of potential.

The design work for the pneumatic tensile testing device which is capable of working in a real reactor core is introduced. Prototype design, load calibrations, load frame for thin specimen tensile testing, and reactor installation with 30 m gas lines is presented. Furthermore, the PSCINCORE device was used to determine stress and strain curves for pure Cu specimen in the BR-2 reactor at Mol in Belgium. Reactor pool water temperature was 90 °C, neutron flux ~$0.3*10^{14}$ n cm^{-2}s^{-1}s (E>1 MeV) and damage rate ~$2*10^{-4}$ h^{-1}. The test type was constant displacement rate test with strain rate ~10^{-7} 1/s.

Some of the results gained in this work are unique, whenever possible however, the test results have been verified by comparison to earlier results with alternative techniques. Invariably, the comparisons prove applicability of the pneumatically powered technology developed in this work.

Special requirements set for the constructional materials used in energy production have strongly influenced the challenges in the component design work. Many material parameters such as corrosion, fracture mechanics, fatigue and oxide films are needed as input data for such work. The generation of reliable data calls also for more sophisticated testing systems. The newly developed pneumatic loading technology provides important potential benefits and has already been successfully applied to testing many kinds of materials in different test environments including a real nuclear power plant reactor core. As the moving parts that penetrate the pressure boundary are not needed, the friction force at the sealing element location is avoided. Furthermore, the new design enables simultaneous testing of several samples, which helps produce more reliable statistical data in a more economical way. This thesis summarizes the work done at the Technical Research Centre of Finland over the past 9 years to increase the knowledge of factors affecting material testing devices and material properties in gas and aqueous coolants at high temperatures.